A comprehensive evaluation of enhanced temperature influence on gas and aerosol chemistry in the lamp-enclosed oxidation flow reactor (OFR) system

Tianle Pan[1,2,3,4,5], Andrew T. Lambe[6], Weiwei Hu[1,2,4,5], Yicong He[7,a], Minghao Hu[8], Huaishan Zhou[1,2,3,4,5], Xinming Wang[1,2,4,5], Qingqing Hu[9], Hui Chen[9], Yue Zhao[10], Yuanlong Huang[11], Doug R. Worsnop[6,12], Zhe Peng[13,14], Melissa A. Morris[13,14], Douglas A. Day[13,14], Pedro Campuzano-Jost[13,14], Jose-Luis Jimenez[13,14], Shantanu H. Jathar[7]

[1]State Key Laboratory of Organic Geochemistry, Guangzhou Institute of Geochemistry, Chinese Academy of Sciences, Guangzhou 510640, China
[2]CAS Center for Excellence in Deep Earth Science, Guangzhou, 510640, China
[3]Chinese Academy of Sciences University, Beijing 100049, China
[4]Guangdong-Hong Kong-Macao, Joint Laboratory for Environmental Pollution and Control, Guangzhou Institute of Geochemistry, Chinese Academy of Science, Guangzhou 510640, China
[5]Guangdong Provincial Key Laboratory of Environmental Protection and Resources Utilization, Chinese Academy of Science, Guangzhou 510640, China
[6]Aerodyne Research Inc., Billerica, Massachusetts, 01821, United States
[7]Department of Mechanical Engineering, Colorado State University, Fort Collins, Colorado 80523, United States
[8]China-UK Low Carbon College, Shanghai Jiao Tong University, Shanghai, 201306, China
[9]Key Laboratory of Organic Compound Pollution Control Engineering, School of Environmental and Chemical Engineering, Shanghai University, 200444, Shanghai, China
[10]School of Environmental Science and Engineering, Shanghai Jiao Tong University, Shanghai, 200240, China
[11]Department of Environmental Science and Engineering, California Institute of Technology, Pasadena, California 91125, United States
[12]Institute for Atmospheric and Earth System Research (INAR) / Physics, Faculty of Science, University of Helsinki, Helsinki, 00014, Finland
[13]Cooperative Institute for Research in the Environmental Sciences (CIRES), University of Colorado at Boulder, Boulder, Colorado, 80309, United States
[14]Department of Chemistry, University of Colorado at Boulder, Boulder, Colorado 80309, United States
[a]now at: State Key Joint Laboratory of Environmental Simulation and Pollution Control, School of Environment, Tsinghua University, Beijing 100084, China

Correspondence to: Weiwei Hu (weiweihu@gig.ac.cn)

Abstract. Oxidation flow reactors (OFRs) have been ~~widely used~~extensively utilized to ~~investigate~~examine the formation of secondary organic aerosol (SOA). However, the UV lamps ~~that are commonly used~~typically employed to initiate the photochemistry in OFRs can ~~lead to increases~~result in ~~the~~a elevated reactor temperature with ~~consequences that have~~their implications not ~~been assessed in detail.~~thoroughly evaluated. In this study, we ~~systematically investigated~~conducted a comprehensive investigation into the temperature distribution ~~inside~~within an Aerodyne Potential Aerosol Mass OFR (PAM-OFR), and examined the ~~associated impacts~~subsequent effects on flow and chemistry ~~arising from~~due to lamp heating. A lamp-induced temperature ~~enhancement~~increase was observed, which was a function of lamp driving voltage, number of lamps, lamp types, OFR residence time, and positions ~~inside~~within the PAM-OFR. Under ~~common~~typical PAM-OFR operational conditions (e.g., < 5 days of equivalent atmospheric OH exposure under low-NOx conditions), the temperature ~~enhancement was usually within~~increase typically ranged from 1-5 °**C**. Under extreme (but less ~~commonly used) settings~~frequently encountered) conditions, the heating could reach up to 15 °**C**. The influence of the increased temperature over ambient conditions on the flow distribution, gas, and condensed phase chemistry ~~inside~~within PAM-OFR was evaluated. ~~We found~~Our findings indicate that the increase in temperature ~~changes~~altered the flow field, ~~leading to~~resulting in a ~~reduced~~diminished tail on the residence time distribution and corresponding oxidant exposure due to faster

recirculation. According to simulation results from a ~~box model using~~ radical chemistry <u>box model</u>, the variation of absolute oxidant concentration ~~inside of~~ <u>within</u> PAM-OFR due to temperature increase was ~~small~~<u>minimal</u> (<5%). The temperature influences on existing and newly formed <u>organic aerosol (</u>OA<u>)</u> were also investigated, suggesting that ~~the~~<u>an</u> increase in temperature can impact the yield, size, and oxidation levels of representative biogenic and anthropogenic SOA types. Recommendations for temperature-dependent SOA yield corrections and <u>PAM-</u>OFR operating protocols that mitigate lamp-induced temperature enhancement and fluctuations are presented. We recommend blowing air around the ~~outside of the~~ reactor's <u>exterior</u> with fans during <u>PAM-</u>OFR experiments to minimize the temperature increase ~~inside~~ <u>within</u> PAM-OFR. Temperature increases are substantially lower for OFRs ~~using~~<u>utilizing</u> less powerful lamps ~~than~~<u>compared to</u> the Aerodyne version.

1 Introduction

Secondary organic aerosol (SOA) ~~can account for~~<u>constitutes</u> 60-95% of <u>organic aerosol (</u>OA<u>)</u> and 10-75% of submicron particles (Jimenez et al., 2009), thus, strongly impacting air quality (Huang et al., 2014), climate (Myhre, 2013; Poschl, 2005) and human health (Nel, 2005; Feng et al., 2016; Nault et al., 2021). Elucidating the formation mechanism of SOA is crucial for clarifying its environmental impact (Ziemann and Atkinson, 2012; Hallquist et al., 2009; Klyta and Czaplicka, 2020). To investigate SOA formation, chambers (Hildebrandt et al., 2009; Cocker et al., 2001; Paulsen et al., 2005; Wang et al., 2014; Carter et al., 2005; Martin-Reviejo and Wirtz, 2005; Rollins et al., 2009; White et al., 2018; Zong et al., 2023) and flow tubes (Cooper and Abbatt, 1996; George et al., 2007; Hanson and Lovejoy, 1995; Robbins and Cadle, 2002; Katrib et al., 2005; Knopf et al., 2005; Ezell et al., 2010) have been commonly used in the laboratory ~~or~~<u>for</u> investigating secondary formation in the early periods of past several decades. In the last decade, due to ~~the fast development of~~<u>rapid advancements in</u> online measurement techniques, ~~different~~<u>various</u> types of oxidation flow reactors (~~OFR~~<u>OFRs</u>), which are portable and ~~can be used in~~<u>suitable for</u> field studies to explore SOA formation under ambient conditions, have been developed and widely deployed (Kang et al., 2007; Watne et al., 2018; George et al., 2007; Peng and Jimenez, 2020; Lambe et al., 2011b; Shah et al., 2020; Saha et al., 2018; Xu and Collins, 2021; Chu et al., 2016; Simonen et al., 2017; Li et al., 2019; Keller et al., 2022 and references therein).

The potential aerosol mass (PAM) reactors, initially distributed by Prof. Bill Brune (the Penn State PAM) and later modified and commercialized by Aerodyne Research Inc~~.~~<u>.,</u>, are the most ~~widely used~~<u>extensively utilized</u> OFRs for ~~studying~~<u>investigating</u> SOA formation and evolution ~~under~~<u>in</u> ambient environments (Peng and Jimenez, 2020). <u>The PAM reactor was first proposed and designed by Kang et al. (2007), leading to successful deployment across various</u> field studies including forests (Hu et al., 2016; Palm et al., 2016; Palm et al., 2017; Palm et al., 2018; Sumlin et al., 2021), urban areas (Ortega et al., 2016; Liu et al., 2018; Chen et al., 2021; Hu et al., 2022; Sbai et al., 2021; Park and Kim, 2023; Xu et al., 2022; Park et al., 2019), rural sites (Ahlberg et al., 2019; Hodshire et al., 2018; Hu et al., 2016), tunnel/roadside studies (Liu et al., 2019; Liao et al., 2021; Tkacik et al., 2014; Saha et al., 2018), as well as ~~in multiple~~<u>numerous</u> laboratory studies (Kang et al., 2007; Lambe et al., 2011b; Bahreini et al., 2012; Bruns et al., 2015; Sengupta et al., 2018; Kramer et al., 2019; Cheng et al., 2021; Lei et al., 2022; Srivastava et al., 2023 and references therein). In the PAM, high concentrations of the OH radicals, which is the major oxidant for SOA formation in ambient air, can be generated quickly by initiating the photochemistry of O_3 and H_2O with UV lamps (185/254 nm) mounted inside of a flow tube (Lambe et al., 2011b; Li et al., 2015; Peng et al., 2015).

~~Earlier studies using~~<u>Previous research utilizing</u> the Penn State PAM reported a temperature ~~increase~~<u>elevation</u> of 2 °C. However, several recent studies using the PAM ~~show~~<u>have demonstrated</u> that the UV lamps can ~~increase~~<u>augment</u> the

85 internal temperature of that reactor by 0-15 °**C** (up values are under extremely high voltage ~~settings~~conditions) above ambient temperature (Lambe et al., 2011a; Chen et al., 2013; Tkacik et al., 2014; Lambe et al., 2019; Charnawskas et al., 2017). ~~However~~Despite this, a ~~full~~comprehensive investigation of the lamp heating effect on the temperature distribution ~~inside of~~within PAM-OFR and ~~clarification~~an elucidation of its influences on the flow distribution ~~inside of~~within PAM-OFR ~~has not been reported yet~~remain unreported. The temperature is a key parameter for gas diffusion and gas/aerosol

90 partitioning (Pankow, 1994; Donahue et al., 2006). The increase in the temperature gradient caused by lamp heating inside an OFR can result in the formation or deepening of recirculating flow, ~~which leads~~leading to a shorter residence time and a broader residence time distribution (Huang et al., 2017; Lambe et al., 2019). Numerous chamber studies have ~~found~~determined that ~~higher~~elevated temperatures ~~may~~can substantially ~~decrease~~reduce the SOA yield (Gao et al., 2022; Lamkaddam et al., 2017; Boyd et al., 2017; Price et al., 2016; Clark et al., 2016; Tillmann et al., 2010; Pathak et al., 2007)

95 and influence SOA chemical composition (Jensen et al., 2021; Gao et al., 2022; Simon et al., 2020; Li et al., 2020a; Kristensen et al., 2020; Quéléver et al., 2019; Denjean et al., 2015). ~~Thus~~Consequently, the increase of temperature ~~inside of~~within PAM-OFR, which could lead to extra uncertainty for SOA ~~simulation~~simulations and ~~study~~studies, should be further assessed and clarified.

In this study, we systemically investigate the effects of lamp-induced heating on PAM-OFR measurements. Based

100 on computational fluid dynamics (CFD) simulation, we show how the temperature affects the flow and average OH exposure ~~inside~~within the PAM-OFR. Two box models were applied to illustrate ~~how~~the ~~enhanced~~influence of increased temperature ~~impacts~~on the chemistry of gas-phase reactions and SOA formation ~~inside~~within the PAM-OFR. The model results can ~~be used~~serve as a ~~rough~~preliminary reference for correcting the related experimental results due to ~~enhanced~~increased temperature. Finally, we ~~propose the use of~~suggest utilizing fans to cool the PAM-OFR and

105 implementing an online sampling strategy that alternates between high and low driving voltages at varied lamp settings to reduce the uncertainty caused by the varied heating effect.


2 Methods

2.1 Oxidation flow reactor (OFR)

The PAM-OFR (Aerodyne Research, Inc~~.~~., abbreviated as ARI) used in this study is a 13 L horizontal aluminum

110 cylindrical chamber (46 cm long × 22 cm ID). Four low-pressure germicidal mercury (Hg) lamps are isolated from the sample flow by type 214 quartz tubes (Fig. S1). The Hg UV fluorescent lamps used in this study are commercial products (GPH436T5VH/4 or GPH436T5L/4, Light Sources, Inc~~.)~~.), which are the default light bulbs ~~chosen~~selected by ARI for the OFR (Fig. S2). ~~In addition~~Additionally, the temperature within an OFR with the Penn State low-pressure Hg UV lamps (model no. 82-9304-03, BHK Inc.), which are also widely ~~used~~utilized in PAM-OFR (Khalaj et al., 2021; Xu and Collins,

115 2021; Lambe et al., 2011b; Siemens et al., 2022; Hu et al., 2016; Ortega et al., 2013; Link et al., 2016; Palm et al., 2016; Kang et al., 2018; Mitroo et al., 2018; Kang et al., 2007), are ~~also~~measured as well. For the Light Sources lamps, the light intensity of each lamp was ~~changed through~~adjusted via the AC voltage input to the lamp ballast, controlled by a computer with settings ranging from 0 V (minimum) to 10 V (maximum, full AC output). For BHK lamps, the maximum setting voltage is 5 V (full AC output). At maximum voltage, the ~~best~~optimal estimation of supply power is 8.9 W (see sect. S1

120 for details) to each lamp for the Light Source lamp and 6.3 W for the BHK lamp. When the lamps are turned on, a pure nitrogen purge gas ~~flows through~~is introduced into the lamp sleeve at a flow rate of 0.2-0.3 L min^{-1}. The lamp sleeve is defined as the space between the lamps and the ~~wall of the~~quartz tube~~. This is done~~ wall to ~~avoid the accumulation~~

~~of~~prevent oxidation products from accumulating on the lamp surface ~~of the lamps~~ and to ~~somewhat~~slightly cool the UV lamps (minor effect, as discussed below). On the inner surface of the front plate of the PAM-OFR, a hexagon nut is ~~connected~~attached to the center inlet. The side of the nut is drilled with holes to promote axial mixing of the sample flow~~,~~ and is hereafter referred to as an inlet diffuser (Fig. S1c) (Mitroo et al., 2018). Two mesh screens~~, used~~ are installed inside the front and back plates to block debris and insects and ~~make the~~to improve air flow ~~more even~~uniformity (helping to break up eddies from outside~~), are installed inside of the front and back plates, respectively~~) (Fig. S1b). A detailed schematic plot of the PAM-OFR used in this study ~~can be found~~is shown in Fig. 1.

2.2 Measurement of OFR temperature

The temperature distribution inside the PAM-OFR was measured with multiple temperature sensors. The types and models of temperature sensors used are listed in Table S1. To ~~assess~~evaluate the accuracy of temperatures measured by different temperature sensors, a ~~comparison~~comparative experiment was ~~carried out~~conducted under different ambient environments. We ~~found~~observed a good agreement (within 2 °C) among the different temperature sensors, supporting the robustness of the temperatures measured in this study (Fig. S3). Detailed information on experimental settings for temperature measurements inside the PAM-OFR is summarized in Fig. 1 and Table S2. Briefly, we measured the air temperature inside PAM-OFR at varied positions (~~vertically~~vertical and ~~horizontally)~~horizontal directions, as well as different depths from inlet (Fig. 1b)) under different lamp ~~settings~~configurations (e.g., number of lamps, ~~lamp~~ types~~, and lamp~~ of lamps, intensity of lamps) and flow rates. ~~To achieve~~For this purpose, an external temperature sensor was placed directly inside the PAM-OFR and was moved manually from outside. The values reported in this study were obtained after the internal temperature ~~inside~~ of the PAM-OFR ~~was stable~~stabilized for ~20 min after switching the PAM-OFR ~~settings.~~configuration. During ~~the~~ measurement, the inlet diffuser and the mesh screen ~~in~~on the front plate ~~of OFR~~ or ~~in the~~ backplate of the PAM-OFR needed to be removed to extend the thermocouple inside the PAM-OFR. We ~~have~~ tested ~~if the removal of~~ whether removing the mesh screen would ~~change~~affect the temperature field inside the PAM-OFR and found ~~a~~negligible ~~impact (~~effects as shown in Fig. S4 (removed the back plate mesh screen) vs. Fig. 5 (removed the inlet diffuser and front plate mesh screen~~))~~). ~~We also~~Additionally, we covered the sensor with shielding paper to ~~avoid the~~prevent potential influences of optical radiation from ~~the~~ UV lamps on temperature detection during this process. In addition to the ~~inside~~internal temperature ~~of OFR~~, the temperature of the inner/external surface ~~of OFR~~, and the temperature in the gas output of the PAM-OFR were also measured for comparison. ~~A sensor for detecting~~A temperature and relative humidity (RH) sensor (referred to as a "primary T/RH sensor", Sensirion SHT21, Sensirion AG) was mounted on the back plate at the factory. Consequently, the default primary T/RH sensor was utilized for temperature measurement in all the experiments. In addition to the temperature measurement in OFR, we measured the residence time distribution (RTD) at different voltages to explore the effect of temperature on RTD. Specifically, we first turned on the lights to make the temperature stable. Then, a 2 s pulse of 50 ppm SO_2 was injected into a 5 L min^{-1} carrier gas (N_2) with RH <10%. N_2 was selected as the carrier gas to prevent the reaction between SO_2 and the generated oxidant when UV lamps were turned on. We measured the RTD with lamp driving voltage set at 0 V, 5 V and 10 V. Note that we only used the outlet for aerosol line for sampling (5 L min^{-1}) during the RTD measurement for better comparison with simulation results in Sec. 2.3. Most of the temperature experiments were done with sampling exhaust line from the ring flow.

4
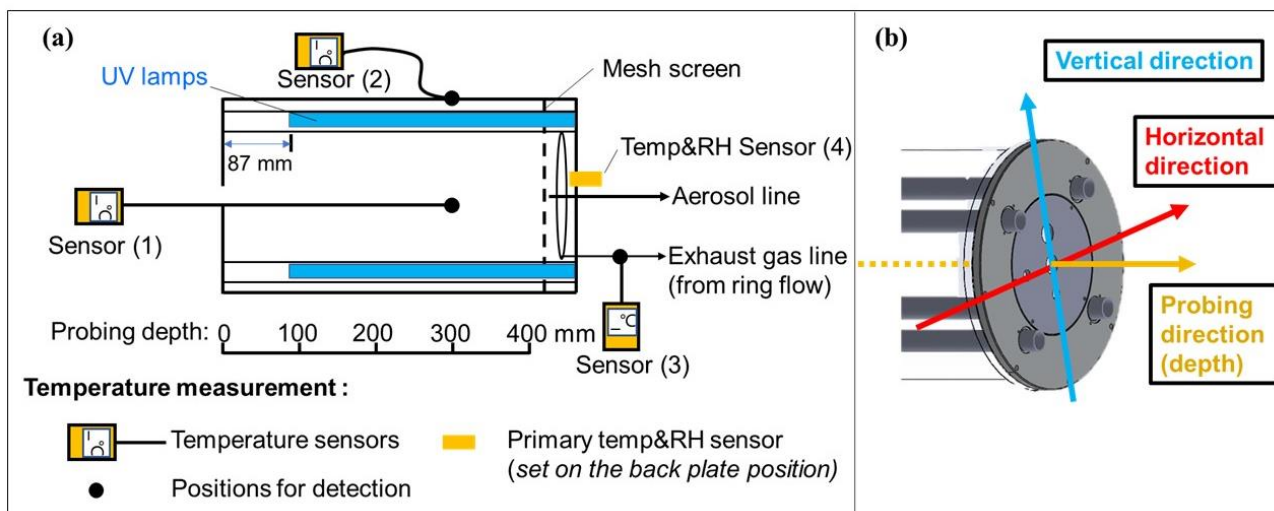
Figure 1: (a) **Schematic plot for temperature measurement in the oxidation flow reactor of this study and (b) directions for temperature measurement. The center inlet, nut, and mesh screen near the front plate were removed when the temperature sensor was probed in the front direction. The information of different temperature sensors used can be found in Table S1.**

2.3 Model simulations on temperature distribution and flow field inside OFR

Computational Fluid Dynamics (CFD) simulations were performed using the ANSYS Fluent software (Version 14.5) in three dimensions to simulate the temperature distribution and flow field in within the PAM-OFR. ANSYS has been used to simulate the flow field insidewithin flow reactors in past studies (Li et al., 2019; Ihalainen et al., 2019). The temperature distribution and flow field under unheated and heated conditions were both simulated with the CFD model. The simulated experimental condition iswas 5 L min^{-1} of air as the carrier gas and 0.3 L min^{-1} of SO$_2$ which was injected for 2 s as the tracer gas. Note that during modeling, the airflow within OFR was only sampled through output for the aerosol line as considering the ring flow manifold for gas phase sampling would significantly increase the complexity for modeling. The convergence of this model was defined when the residuals of physical quantities (e.g., pressure, temperature, velocity, density, and viscosity, etc.) were below 0.001.

For the unheated condition, the more advanced "realizable k-epsilon turbulence model" was usedemployed (Shih et al., 1995). The simulation was solved by using the pressure-based SIMPLEC algorithm, which is a commonly useda prevalent method in CFD models for simulating incompressible flow problems (Patankar and Spalding, 1972), as OFR conditions with lights were off.. For the heated condition, the thermal boundary was set to a series of fixed temperatures, based on thosederived from directly measuredmeasurements in the PAM-OFR. When the driving voltagevoltages of all the PAM-OFR lamps was allwere set to be 5 V, the model settings applied were 55 °**C** for the surface of the quartz UV lamp sleevessleeve surface, 35 °**C** for the inner wall surface, and 26 °**C** for the carrier gas. When the driving voltages of all the voltages of the PAM-OFR lamps were set to 10 V, thosethese values were setadjusted to 62 °**C**, 40.5 °**C**, and 23 °**C**, respectively. The lower carrier gas temperature under 10 V conditions vs,compared to 5V was caused byattributed to the different variations in room temperatures in each across different real experimentexperiments. The viscosity and thermal conductivity of the mixing gas were calculated using the mass-weighted-mixing-law (Ni et al., 2010). The Least Squares Cell-Based method and the species transport model were used for the solution (Ghia et al., 1982).

2.4 KinSim kinetic model for gas-phase reactions

The influence of temperature on gas-phase reactions was modeled using a box model (KinSim 4.14 in Igor Pro. 6.37), incorporating the OFR radical mechanisms as utilized by Li et al. (2015), Peng et al. (2015) and Peng et al. (2019). All gas-phase reactions were derived from the JPL chemical kinetic data evaluation, which incorporates temperature as a variable for reaction rate calculation (Burkholder et al., 2019). In the model, we assumed a mixing volume of 800 ppb SO_2 injection into the PAM-OFR with a constant 2.2% water vapor mixing ratio (RH=70% at 25 °C), based on calibration experiment settings. This corresponds to an OH reactivity (OHR) of the incoming air of 20 s^{-1}. The simulated SO_2 output concentration in the model was weighted by the measured residence time distribution (RTD) at a flow rate of 5 L min^{-1} (~700 s). Good agreement between the modeled SO_2 decay based on the KinSim model and the measured SO_2 results has been demonstrated in Hu et al. (2022).

The OFR185 mode mechanism, which involves the generation of O_3 and OH radicals via the photolysis of O_2 and H_2O within OFR, was incorporated into the model. Note that the photon flux ratio between 185 and 254 nm, derived from lamps manufactured by Light Source Inc., remains constant regardless of their intensity (Rowe et al., 2020). However, these ratios exhibit variation with intensity for the BHK lamps (Li et al., 2015). In the model, the photon flux ratio of 185/254 nm was set to be constant (5%). Results for 25 °C to 40 °C (binned with 5 °C) were modeled, which covers the typical temperature range within the PAM-OFR under most lamp settings. These simulations were conducted using residence time distribution (RTD) obtained under unheated conditions in the PAM-OFR (25 °C). Since the RTD inside OFR can also be influenced by temperature (Lambe et al., 2019), we also showed the model results with measured RTD at 40 °C.

2.5 SOM model for SOA formation

The Statistical Oxidation Model (SOM) is a kinetic, process-level model designed to simulate the SOA formation. This model incorporates gas-particle partitioning, multi-generational oxidation (fragmentation and functionalization), and autoxidation for highly oxygenated molecules (HOMs) (Cappa and Wilson, 2012; Eluri et al., 2018; He et al., 2021; He et al., 2022). The SOM model has been shown to successfully capture the evolution of SOA formation and oxidation in multiple laboratory and field studies (Cappa and Wilson, 2012; Jathar et al., 2015; Eluri et al., 2018; Akherati et al., 2020; He et al., 2021; He et al., 2022). In the SOM model, the oxidation of a VOC precursor is tracked by its evolution within a carbon−oxygen grid. The volatilities and reactivity (k_{OH}) of organic species in each grid are determined based on their carbon (N_C) and oxygen numbers (N_O) (Cappa and Wilson, 2012; Jathar et al., 2015; Eluri et al., 2018). In total, six adjustable parameters are used to determine the reaction probabilities and volatility of the grid species. Four parameters (p1-p4, Table S3) indicate the number of oxygens added per functionalization reaction, and two other parameters describe the probability of fragmentation (m_{frag}, Table S3) and the reduction in vapor pressure (ΔLVP, Table S3) per oxygen atom added to the carbon backbone (Jathar et al., 2016; Akherati et al., 2019).

In this study, we employed the SOM model in conjunction with the TwO-Moment Aerosol Sectional model (TOMAS) (Adams and Seinfeld, 2002; Pierce et al., 2007) to simulate the temperature influences on the yield, oxidation state, and size distributions of newly formed SOA within the PAM-OFR. In the model, the temperature dependence is determined by the Clausius–Clapeyron Equation:

$$P_i^* = P_{i,ref}^* \times e^{(\frac{H_i^{vap}}{R} \times 10^3 \times (\frac{1}{298} - \frac{1}{T}))}$$ (1)

where R (8.314 J mol⁻¹ K⁻¹) is the ideal gas constant, P_i^* and $P_{i,ref}^*$ (Pa) are the saturation pressure of species i at target temperature and reference temperature (298 K ~~used here~~), respectively. The $P_{i,ref}^*$ can be calculated based on the ~~following~~ equation (2):

$$P_{i,ref}^* = \frac{C_{i,ref}^* \times R \times 298}{MW_{org,i} \times 10^6}$$ (2)

where $MW_{org,i}$ (g mole⁻¹) is the molecular weight of organic species i and $C_{i,ref}^*$ (µg m⁻³) is the saturation concentration at 298 K. The $MW_{org,i}$ and $C_{i,ref}^*$ are calculated based on the number of C (N_C) and O (N_O) and ΔLVP of species i (Eluri et al., 2018). The H_i^{vap} (kJ mol⁻¹) is the evaporation enthalpy of species i, calculated ~~as followed~~using the equation (3) (Epstein et al., 2010):

$$H_i^{vap} = -11 \times log\, C_{i,ref}^* + 131$$ (3)

In addition, constant H_i^{vap} of 80, 100, 120 and 150 kJ mol⁻¹, derived from analysis of field data, was also tested in the model (Saha et al., 2017; Cappa and Jimenez, 2010; Louvaris et al., 2017).

In this study, SOA formation from four typical VOC precursors including dodecane, α-pinene, toluene, and m-xylene was modeled under different OA concentrations (1-80 µg m⁻³) and NOx conditions (low NOx vs high NOx~~) was modeled.~~). Five ~~stages of~~ temperature stages ranging from 20-40 °C were simulated. Similar to the gas-phase simulations, results were also calculated based on the measured RTD obtained at both ~25 °C and ~40 °C (for the modeled yields under 40 °C~~)~~), with a total model time of 700 s. Additionally, we also considered the highly oxygenated organic molecules (HOMs) in this model that contribute to new particle formation (He et al., 2021; Bianchi et al., 2019). The HOM yields and other detailed information for input parameters can be found in Table S3. These parameters were obtained by fitting the simulated results to the measured chamber results under high and low NOx conditions, respectively (Eluri et al., 2018; Cappa et al., 2016). Thus, the exact NO concentration was not considered in the SOM model during the simulation

## 3 Results and discussions

3.1 Heating effect inside OFR

To characterize the temperature distribution ~~in~~within the PAM-OFR, we measured the temperature as a function of lamp driving voltage, number of lamps ~~used~~, flow rate, lamp types, and different ~~space~~spatial positions.

3.1.1 Enhanced temperature vs lamp driving voltage (OH exposures) and flow rate

In general, ~~we observed~~ a systematic ~~increase in~~ temperature ~~inside~~increase was observed within the PAM-OFR with Light Source lamps. As shown in Fig. 2a, the ~~enhanced~~ temperature ~~in~~within the PAM-OFR ~~increases~~increased as a function of lamp driving voltage and, hence, OH exposures. When the driving voltage ~~on~~of the 2-lamp setup was changed in increasing fashion (~~from~~ 0 V to 3 V, Light Source lamp), the temperature ~~enhancement in~~increase within the PAM-OFR was generally ~~lower~~less than 5 °C. 3 V ~~is roughly~~was approximately equivalent to a photochemical aging time of around 5 days (assuming the water mixing ratio ~~is~~was 1.88%, RH~~≈~~=60%, external OH reactivity=30 s⁻¹). For a higher voltage range (~~from~~ 3 V to 10 V, which ~~is equivalent~~corresponds to a photochemical aging time from 5 days to two weeks), the

temperature inside the <u>PAM-</u>OFR increased by 10 °**C**. Note that the relationship between the lamp driving voltage and OH exposure varied ~~with~~<u>depending on</u> the number and type of UV lamps used, as well as ~~how~~ the <u>operation mode of the PAM-</u>OFR ~~was operated, as shown in~~ (Fig. S5~~.~~<u>).</u> When four lamps were turned on and the <u>lamp</u> driving ~~lamp~~ voltage was increased from 2 to 10 V, the temperature <u>inside the PAM-OFR</u> increased by 5-20 °**C** ~~inside the OFR~~ for the laboratory tests (Fig. 2a and 3a). These results ~~support~~<u>indicated</u> that the temperature increase inside of the <u>PAM-</u>OFR ~~is~~<u>was</u> mainly due to the heat from the lamps~~ and~~<u>, which</u> was further ~~supported~~<u>confirmed</u> by Fig. 3b, which ~~shows~~<u>showed</u> that the temperature ~~enhancement~~<u>increase</u> inside the <u>PAM-</u>OFR decreased as a function of the flow rate from 3 L min^{-1} to 7 L min^{-1} (Fig. 3b). The anti-correlation between the temperature ~~enhancement~~<u>elevation</u> and ~~the~~ flow rate was mainly ~~due~~<u>attributed</u> to the ~~higher heat capacity~~<u>larger gas mass</u> provided by the increased air flow, ~~thus needing~~<u>so that</u> a lower temperature increase <u>was required</u> to ~~carry the~~<u>transfer</u> excess heat from the lamps.
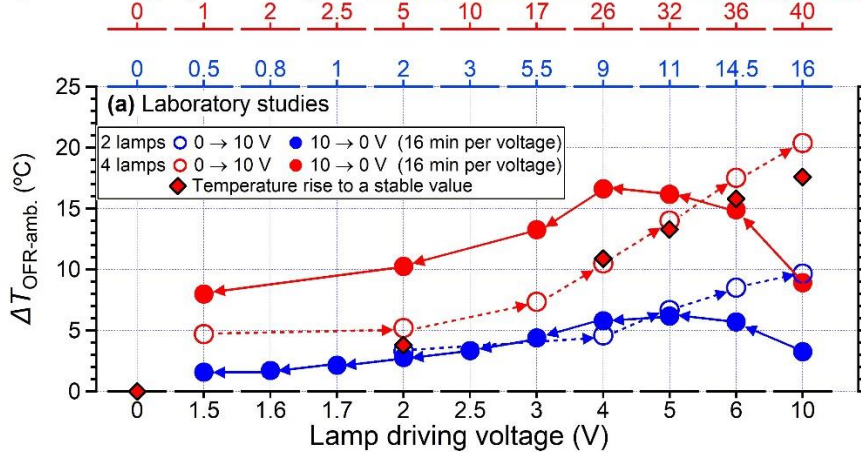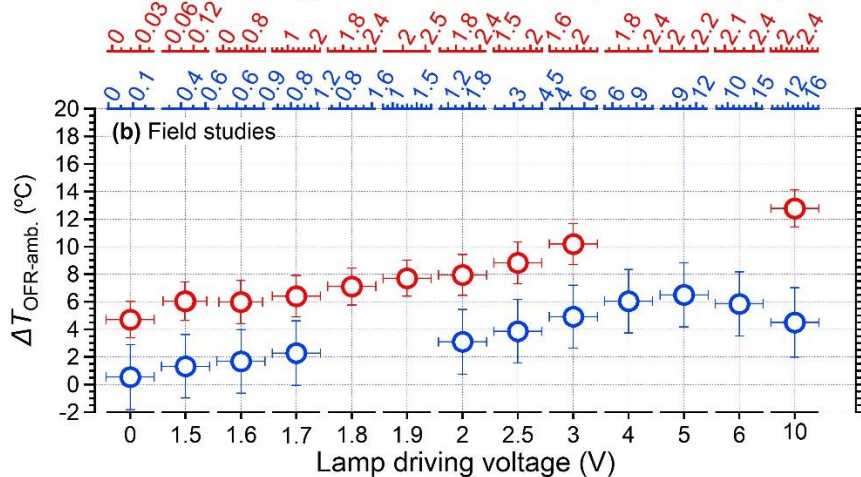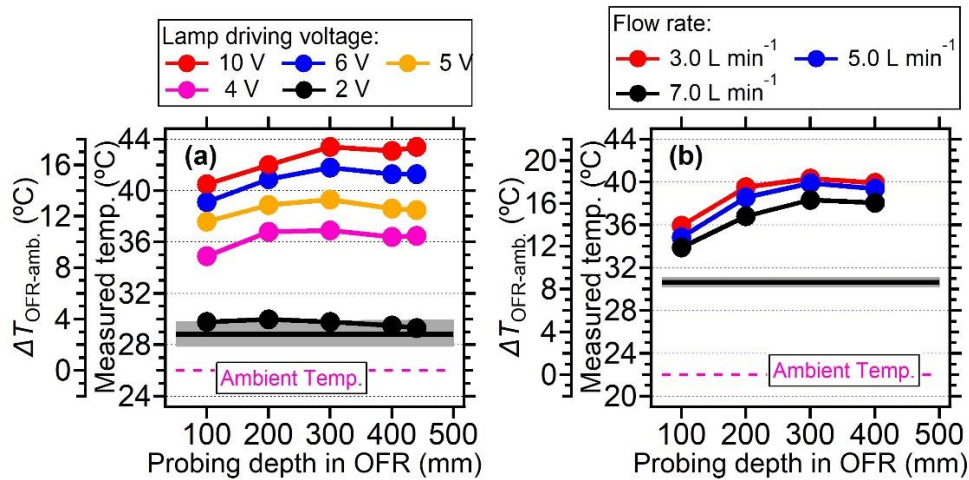

Figure 2: (a) ~~Enhanced temperature~~<u>Temperature elevation</u> **inside** <u>the PAM-</u>**OFR (**~~Measured~~<u>measured</u> **temperature in OFR minus ambient temperature) as a function of the lamp driving voltage using two lamps and four lamps in the laboratory studies. Note that without specific notification, all the temperature measurement results shown in the main text are obtained with lamps produced by Light Source Inc. The relationship between lamp driving voltage and OH exposures for using two lamps and four lamps can be found in Fig. S5. The OH exposures were calculated based on the empirical parameters in Hu et al. (2022) assuming a mixing water ratio of** ~~around~~ **1.88% and** <u>an</u>

275　**external OH reactivity of 30 s⁻¹. The equivalent aging days (top axis) were estimated by assuming ambient OH** ~~concentrations are around~~ concentration of **1.5x10⁶ molecules cm⁻³**~~.~~ (Mao et al., 2009). **The lamp** ~~type~~types **applied here** ~~is~~were **uncovered for field studies with four lamps in Fig. 2b and 80% covered for other conditions. The** temperatures were **measured** ~~position of temperature is in~~at **the centerline with** a **300** ~~nm~~mm **probing.** ~~The flow~~ **flow rate** ~~is~~was **5 L min⁻¹. (b)** ~~Enhanced temperature~~Temperature elevation **inside** the PAM-**OFR as a function of light**
280　**settings in the field studies. Two lamps were applied** ~~in the~~for **low NOx conditions, while** ~~the~~ **four lamps were** used **for high NOx conditions. The high NOx reaction regimes were achieved by** ~~inputting~~the introduction of **extra N₂O as illustrated in Peng et al. (2018) and Lambe et al. (2017).**

Figure 3: (a) The measured temperature and the temperature elevation (measured temperature in OFR minus
285　ambient temperature) **under different lamp driving voltage and (b) at different flow rates for Light Source lamp. The temperature was measured in the centerline at different probing positions. Black lines and gray shadows** ~~represent~~represented **the temperature measured by the primary T/RH sensor. For panel (a) four lamps were all turned on during measurement. The flow rate** ~~is~~was **5 L min⁻¹; For panel (b), four lamps were set in** ~~10~~5 **V.**

When the lamp driving voltage was set in a monotonically decreasing fashion (e.g., from 10 V to 0 V), the maximum
290　temperature increase did not occur at the highest voltage setting of lamps (10 V), but in the range of 4-6 V, as shown in Fig. 2a and b. This ~~inconsistency is mainly due~~discrepancy was primarily attributed to the fact that the lamps ~~starting~~were initiated at 10 V ~~with colder~~under cooler conditions (e.g., room temperatures or lower voltage settings), ~~meanwhile,~~while the OFR reactor ~~has~~had a thermal mass that ~~needs~~required time to accumulate or dissipate heat. As depicted in Fig. 4 ~~shows that,~~ the entire system ~~needs more than~~necessitated over 100 minutes to achieve a thermal steady state. However, a much
295　shorter ~~time~~durations (15-24 minutes) ~~is~~were usually applied in the laboratory and field studies when voltages ~~are~~were systematically varied (Link et al., 2016; Murschell and Farmer, 2018; Hu et al., 2016; Ortega et al., 2016; Palm et al., 2016; Palm et al., 2018; Saha et al., 2018; Shah et al., 2020; Hu et al., 2022). These ~~short~~brief constant lamp power ~~times result in reduced~~periods led to diminished temperature variation between different power settings, as well as ~~inconsistency~~inconsistencies between maximum temperature peak with maximum power setting. To ~~be clear~~elucidate, the
300　time series of measured temperature when the lamp driving voltage was set under a representative lamp voltage cycle (decreasing fashion: 10-6-5-4-2-0 V) ~~are displayed~~were presented in Fig. 5. Two scenarios with two and four lamps being turned on were both shown. The reason ~~that~~for initiating the lamp voltage ~~starts with~~at 10 V in this typical setting ~~is~~was to ~~maximize~~optimize the efficiency of filament ignition in UV fluorescent lamps. Even though the thermal steady state was

not achieved at each voltage ~~setting~~, temperature increases of 2-8 °C for two lamps and 6-16 °C for four lamps were observed. In general, the temperature ~~enhancement~~increase inside the PAM-OFR is a function of the voltage profile and the time spent at each voltage. ~~Maximum~~The maximum SOA formation ~~is~~was typically observed after 1-2 days of equivalent age (Ortega et al., 2016; Palm et al., 2016; Hu et al., 2022). In most cases, the temperature ~~enhancement~~increase inside the PAM-OFR ~~is~~was generally less than 5 °C below 5-7 days of equivalent atmospheric OH exposure ~~under~~in laboratory and field studies ~~as shown in Fig.~~(Figs. 2a and 2b~~.~~). The main exceptions ~~involve~~were specific OFR modes that incorporate N_2O or isopropyl nitrite precursors to establish high-NOx conditions (Lambe et al., 2017; Lambe et al., 2019). In these cases, four lamps ~~are~~were beneficial to compensate for the absorption of 185 nm radiation by N_2O (Peng et al., 2018) that ~~hinders~~inhibited HO_x production, or the relatively weak absorption of UVA radiation by isopropyl nitrite, respectively. This also ~~makes the~~results in more uniform radiation within the OFR ~~more uniform,~~ as when only two lamps are used, the area with another two lamps off would be darker due to the absorption of radiation.
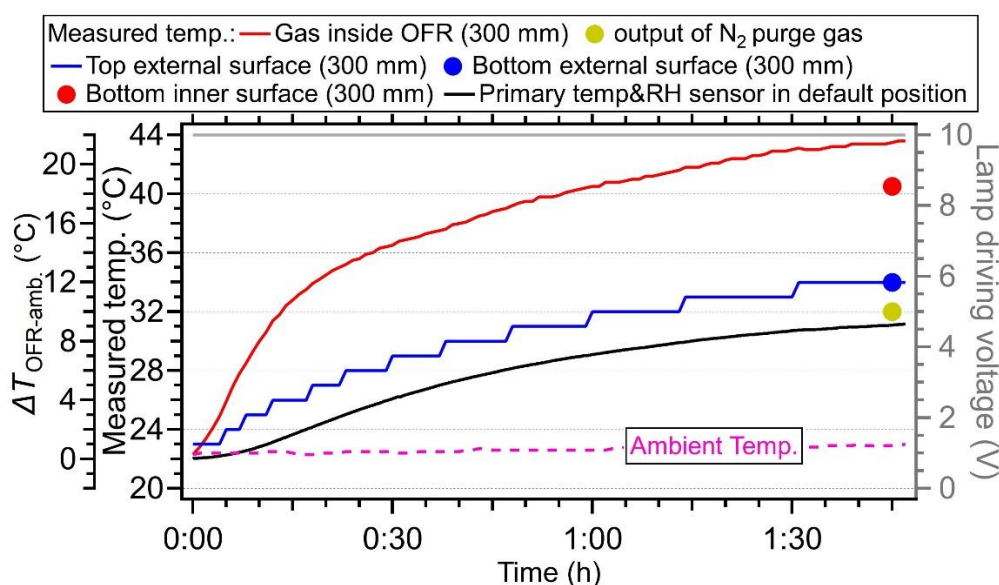

Figure 4: The temperature variation under 10 V driving voltage for 4 lamps as a function of time. The ~~start~~starting time ~~is~~was defined as the moment when the lamps ~~being~~were turned on. The temperature sensors were set at a depth of 300 mm in the central line to measure the temperature inside the PAM-OFR. The flow rate ~~is~~was 5 L min⁻¹. The temperature of the external surface of OFR ~~is~~was also measured at the top and bottom positions. The temperature measured by the default OFR sensor installed ~~in~~on the backplate ~~is~~was also shown in the black line. The purple dotted lines represent the ambient temperature.

3.1.2 ~~Enhanced temperature~~Temperature increase vs lamp types.

The temperature ~~enhancement~~increase as a function of ~~different~~lamp types ~~of lamps~~ was also investigated ~~here~~. The four types of lamps tested ~~lamps are~~were shown in Fig. S2. Fig. S6 ~~shows~~showed similar temperature distribution inside the PAM-OFR ~~no matter whether~~with 80% covered or uncovered lamps, as well as ~~no matter whether~~with only 254 nm or 254/185 nm lamps ~~were used~~. These results ~~suggest~~indicated that the ~~heating inside OFR is mainly from the~~heat transfer ~~of~~from the hot quartz sleeve (heated by the lamps) ~~but not from~~was the main source of heating inside the PAM-OFR, rather than their optical radiation. ~~Thus~~Therefore, different lamp types ~~of lamps~~mainly impact ~~mostly the~~OH exposures, but not ~~the~~heating ~~effect. The~~effects. All the three ~~types of~~lamps applied here ~~are all from the same manufacturer (~~were manufactured by Light Source Inc~~) and, therefore~~., so they have ~~a~~similar ~~value of~~power supplied to each lamp (8.9 W).

In addition, we ~~also tested~~measured the temperature ~~enhancement~~increase in the OFR with lamps from another ~~producer~~manufacturer (BHK Inc.). ~~An enhanced~~A temperature increase of 6 °**C** inside the OFR was found at the centerline when two BHK lamps at full power (Fig. S7b) were used ~~in an OFR~~ with a flow rate of 4.5 L min^{-1}. The ~~less enhanced~~ lower temperature increase with BHK lamps ~~is probably~~was due to the lower input heating energy (6.3 W per lamp)

335 ~~than~~compared to the ~~lamp~~lamps from Light Sources. For the lower driving voltage of 0.95 V for BHK lamps ~~as run~~ during a field campaign, a temperature ~~enhancement~~increase of 1-2 °**C** with an equivalent aging time of around 1.5 days was observed (Fig. S7a and S7b). ~~For~~During that campaign, the OFR was operated mostly continuously at ~1.5 days equivalent aging, since most SOA formation is often ~~is~~ observed at these moderate exposures, and is low enough that heterogeneous oxidation is not yet significant (e.g., Palm et al. (2016), Ortega et al. (2016) and Hu et al. (2016)).

340 **3.1.3 Mapping out the temperature ~~enhancement~~increase inside the PAM-OFR**

In this section, the ~~enhanced temperatures inside of~~temperature increase within the PAM-OFR as a function of position ~~are~~was explored. In our case, when the voltages of four lamps ~~are~~were set to be 5 V (~30 days' ~~equiv.~~equivalent aging time and flow rate of 5 L min^{-1})), the ~~temperature~~temperatures in the PAM-OFR ~~is~~were generally 9-15 °**C** higher (Fig. 6a) than the ambient (26 °**C**). ~~In the vertical axial direction~~Vertically, the ~~enhanced~~ temperature ~~is~~increase was higher

345 at the top position (~14 °**C**) ~~than at~~compared to the bottom (~9 °**C**)), due to the warm air ascending in the PAM-OFR resulting from its lighter density. ~~We also found a~~A similar conclusion was found for BHK lamps (Fig. S7) with a lower temperature ~~enhancement~~increase and smaller temperature difference in the vertical direction for the same equivalent aging. Horizontally, the temperature distribution ~~is~~was symmetrical, ~~which shows~~with a slightly lower temperature value in the middle and ~~enhanced~~an increased temperature on the edges (Fig. 6b). These ~~temperature~~temperatures values were

350 measured until their reading varied no more than 0.1 °**C**. The lower center temperature ~~is probably caused by~~could be attributed to the faster flow rate (shorter residence time) of air mass in the middle due to the removal of the inlet diffuser and the longer distance from the lamps. However, the largest temperature gradient at different horizontal axial positions ~~is~~was within 2-3 °**C**, ~~suggesting~~indicating that the general temperature distribution measured here ~~is similar~~was comparable to ~~the distributions~~that when the inlet diffuser ~~is~~was installed. For different probing depths, Fig. 3 generally ~~shows~~showed

355 that the ~~enhanced~~ temperature ~~is~~increase was lower near the inlet and higher from the middle position to the back in the central line, ~~which is~~mainly due to ~~that~~ the airflow flowing from the inlet to the outlet ~~is~~ being warmed, as well as the set position of lamps ~~has~~having a gap with the front plate ~~with the input inlet~~, as demonstrated in Fig. 1.
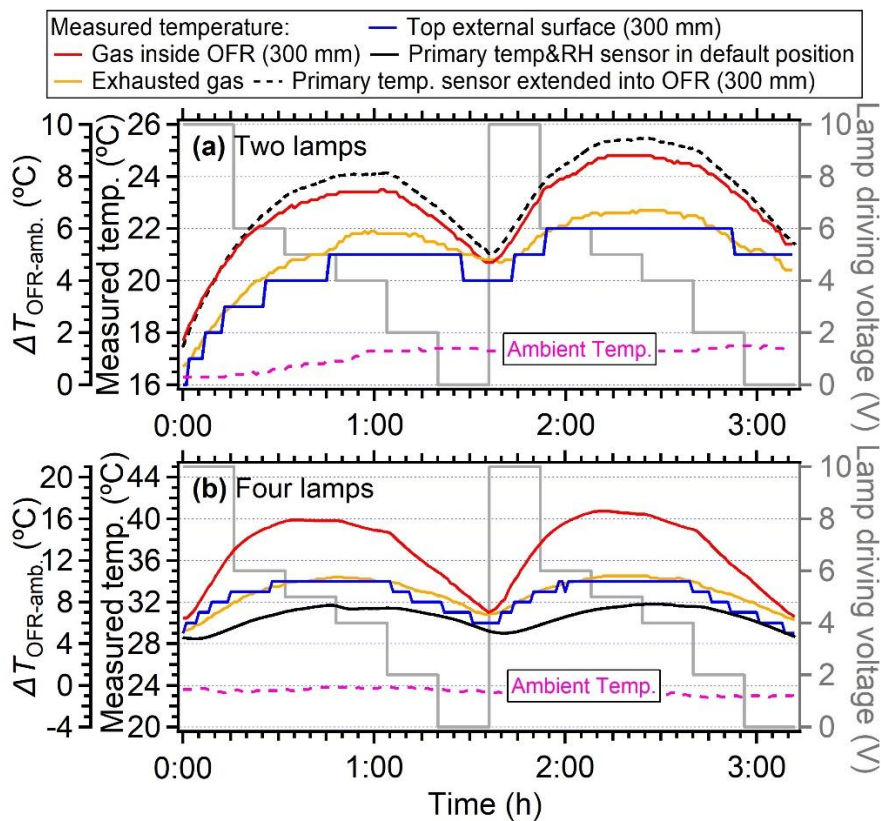
Figure 5: Temperature variation under different lamp driving voltage ~~cycled as~~cycles of 10-6-5-4-2-0 V for: (a) Two symmetrical lamps on the diagonal direction were used and the OFR backplate sensor was extended into the PAM-OFR (from the backplate) at a depth of 300 mm from the inlet. (b) Four lamps were used and the OFR sensor was set ~~in~~on the backplate. Each lamp setting ~~lasts~~was operated for a duration of 16 min. The flow rate of sampling air ~~is~~was 5 L min⁻¹ (residence time ~~is~~of 167 s).

3.1.4 Loss of heating energy in OFR

The gain of the heating energy inside the PAM-OFR generally comes from the UV lamps, while the energy loss inside the PAM-OFR is mainly through three pathways: (1) The ~~loss~~dissipation of energy through the exhaust air ~~of~~(from the ring flow set in this study) from the PAM-OFR; (2) The ~~dissipation of~~convection and radiation-induced heat energy transfer from the PAM-OFR ~~chambers (OFR metal tubes)~~surface to the ambient air ~~by convection and radiation.~~. (3) The energy loss through the purge nitrogen between the lamps and quartz sleeves (Fig. S8).
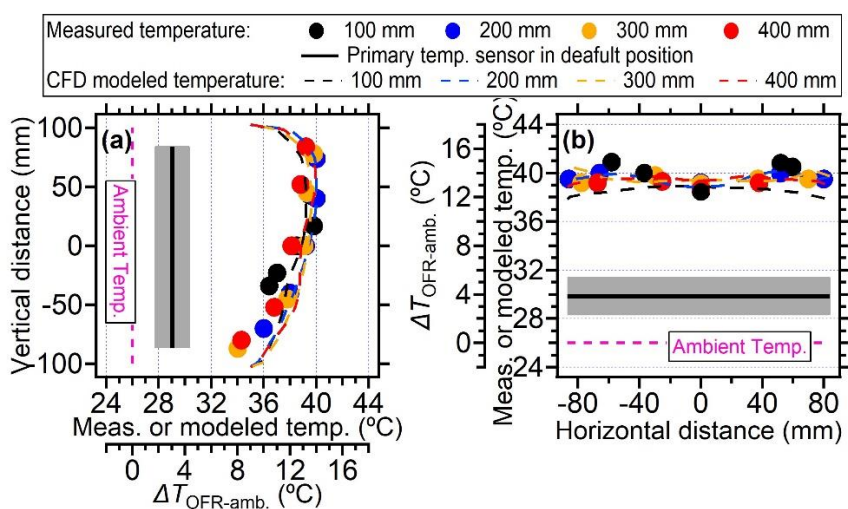
Figure 6: The temperature measured by external temperature sensor at different positions ~~inside~~ within the PAM-OFR or under different settings: (a) the measured and CFD modeled temperatures on the vertical direction at different probing depths; (b) the measured and CFD modeled temperatures on the horizontal direction at different probing depths. All the four lamps were turned on during measurement. The four lamps' driving voltages were 5 V. The black lines and grey shadings ~~are~~were the average ± standard deviation for temperature measured by the backplate sensor.

To ~~clarify~~elucidate the energy balance ~~of~~across the three pathways, we measured the temperatures of the PAM-OFR tube, the purge nitrogen, and the exhaust air. ~~In this case, we demonstrate the results under the~~Specifically, our findings were based on maximum lamp driving ~~voltage~~voltages of four UV lamps (10 V) ~~and~~at a flow rate of 5 L min^{-1}. Figure 4 ~~displays~~displayed the measured temperature of the PAM-OFR tube as a function of time and at different positions (inner vs external surface, bottom vs top surface). The temperature ~~of~~at the top external ~~surfaces increases~~surface increased as the gas temperature ~~inside~~within the PAM-OFR ~~gets higher, supporting~~rose, indicating that the PAM-OFR tube ~~receives~~absorbed the heating energy from lamps. The temperature detected at the inner surface of the OFR (40.5 °C) ~~is~~was lower than ~~the temperature~~that of gases (43.5 °C), ~~however,~~yet higher than that of the ~~outside of~~external tube surfaces (34 °C). The lower temperature of the external surface ~~of the OFR~~ than the air masses inside ~~of~~ the PAM-OFR could be attributed to i) there are heat losses on the OFR ~~is probably because i) the~~tube surface since the ambient air temperature (23 °C) is substantially lower than that of the OFR tubes, resulting in heat transfer. This heat transfer was also reflected by the diminishing temperature gradient between inner and external OFR tube surfaces (40.5→34 °C). We further measured the temperature of purged nitrogen at a default flow rate of 0.2 L min^{-1}. In this case, the temperature of exhausted nitrogen was ~32 °C (output), which was 9 °C higher than the temperature of input nitrogen (23 °C). ii) When the temperature equilibrium between the air and OFR was not balanced, an additional reason will cause the lower temperature in OFR tube. The aluminum OFR chamber has a higher thermal mass than the air. Although the specific heat capacity of metal (0.908 J g^{-1} K^{-1} at 301.60 K) is similar to that of air (1.005 J g^{-1} K^{-1} at 300 K) (Giauque and Meads, 2002; Kieffer, 1956), the flow tube is ~~much~~considerably heavier than the air due to ~~much~~its significantly higher density ~~of the former~~ (2700 Kg m^{-3} vs 1.29 Kg m^{-3}), resulting in a lower temperature ~~of~~for the OFR tube than the inner air.

In addition to the air inside the PAM-OFR, the temperature of exhausted air (from ~~OFR~~the ring flow, Fig. S1) was also examined closely. A temperature sensor was set in the Teflon Tee connector near the output of the PAM-OFR backplate. We found a slightly lower temperature ~~enhancement~~increase (≤5 °C, Fig. 5a) in the exhausted air ~~than~~compared

370

375

380

385

390

395

13

to the ~~values of~~ air measured directly inside the PAM-OFR~~, which is~~. This discrepancy was probably ~~influenced by~~due to
the ~~colder~~cooler surfaces of the fitting or sampling lines. Using ~~the measured~~these temperatures shown above, we ~~can~~
roughly ~~calculate~~calculated the fraction of energy loss among three pathways. Detailed information on ~~the~~ calculation
~~process can~~could be found in Sect. S2 of the supporting information. Those model results ~~suggest~~indicated that after 105
min of heating~~up~~, 51% of the total power (35.6 W, 8.9 W for each lamp, 4 lamps in total) during the heating process ~~is~~was
converted into energy ~~that leads to~~causing the temperature increase of the PAM-OFR. The remaining 49% of power ~~is~~was
lost due to the conversion efficiency or converted into other energy that ~~does~~did not cause the warming of airflow inside
the PAM-OFR. For the fraction (51%) of energy that ~~causes~~causing warming, the ~~fraction of~~ energy loss fractions through
purged nitrogen gas (at flow rate 0.2 L min^{-1}), heated air, and OFR tubes ~~is~~were 0.3%, 9.8%, and 89.9%, respectively~~, as~~
~~shown in~~ (Fig. S9a~~.~~). This ~~suggests~~indicated that the ~~heating~~dominant pathway for heat transfer was through metal tubes
~~would be the dominant pathway.~~. Cooling the OFR tubes ~~is a good way to keep~~was an effective method to maintain the
PAM-OFR near ambient temperature. As shown in the following sect. 3.5, with two fans blowing on the OFR tube, the
heat dissipation of the OFR tube increases, resulting in a ~~much~~significantly lower ~~increase in~~ temperature increase inside
the PAM-OFR.

In some OFR systems, a higher flow rate of nitrogen-purged air was applied (Zhao et al., 2021; Bruns et al., 2015; Li
et al., 2019). ~~E.g.,~~For example, Li et al. (2019) set the purged nitrogen flow rate at around 30 L min^{-1} for their custom-
designed OFR system with exterior lamps to keep the temperature at around 25 °**C**. We ~~tried~~attempted to introduce a
nitrogen gas flow at 20 L min^{-1} through the lamps to increase the energy loss for the ~~ARI~~PAM-OFR. This ~~is~~was almost
the maximum flow rate of purged nitrogen ~~we can test~~that could be tested due to the small inner diameter of the fitting
connected to the lamp tubes. After nitrogen was injected at such a high flow rate, we found the temperature of the lamp
sleeve, the inner surface of flow tubes, and gas inside the PAM-OFR dropped from 62, 40.5, and 44 °**C** (four lamps at 10
V) to 42, 34 and 36.5 °**C** (36-51% ~~decreases~~decreased in temperature increase, with ambient temperature at 23 °**C**),
respectively. Based on the measured temperature, we found the energy loss fraction through purged nitrogen increased
from 0.3% to 32% (Fig. S9b). This ~~is~~was helpful, but it still ~~cannot~~could not balance the heating energy input from the UV
lamps. The temperatures of air in the PAM-OFR (36.5°**C**) ~~are~~were still ~~much~~significantly higher than the room temperature
(23 °**C**). The large consumption of pure nitrogen gas for running such a high flow rate would also ~~be~~pose a challenge for
long-term experiments, especially for field studies.

3.1.5 Artificially low temperature measured by primary T/RH sensor in ARI OFR

During the experiment, we found that the primary T/RH sensor installed in the OFR backplate (see the sensor in Fig.
S1) always showed a ~~much~~significantly lower temperature (by 1-14 °**C**) than the temperature sensor ~~probing~~probed inside
~~of~~ the PAM-OFR~~, as shown in~~ (Figs. 3-6~~.~~). We ~~suspect~~hypothesized that the lower temperatures detected by the primary
sensor at the default backplate position were mainly ~~caused by~~due to the direct contact of this sensor with the metal
backplate which ~~is~~was at lower temperatures. When the primary sensor was placed ~~around~~at 300 mm into the PAM-OFR
from the backplate (closer to the lamps than the centerline, as the default location of the sensor on the backplate was not in
the centerline, Fig. s1), a similar temperature was measured by the primary T/RH sensor and the one ~~probing~~probed into
the PAM-OFR (maximum difference of 1 °**C**), as shown in Fig. 5a. This ~~suggests~~indicated that the primary T/RH sensor
in the backplate with default OFR settings ~~might lead~~led to underestimation of the temperature inside of the PAM-OFR,
which should be verified and corrected by the users based on the configuration of their instrument.

14

3.2 Temperature influence on the flow field

In this section, we discuss the impact of ~~enhanced~~elevated temperature on fluid dynamics ~~inside~~within the PAM-OFR based on Computational Fluid Dynamics (CFD) simulations. Detailed setting parameters were introduced in Sect. 2.3. The temperature field where the voltages of four UV lamps were all set to 5 V was tested here. As shown in Figs. 6a and b, the simulated temperature distribution generally ~~shows~~showed good agreement with the values measured directly with the temperature sensor ~~inside~~within the PAM-OFR, validating the reasonableness and reliability of both simulated and measured temperature ~~distribution in OFR.~~distributions. In Fig. 7a, the simulated 2-D temperature distributions ~~display~~revealed the hottest air (up to 45 °C) ~~wrapped around~~encircling the UV lamps. The rest ~~of the~~ air parcels ~~have~~exhibited a ~~very large~~pronounced vertical axial temperature gradient (~10 °C~) and the air~), with ~~higher~~ temperatures ~~between~~ranging from 35-45 °C ~~remains~~persisting in the upper ~~position~~region of flow tubes. Such a ~~high~~pronounced temperature gradient ~~will lead~~was anticipated to ~~substantial~~induce significant recirculation ~~inside~~within the PAM-OFR, ~~based on~~as evidenced by the Richardson number calculation (Ri = 3974, which is far above 10 and indicates the existence of turbulence) (Huang et al., 2017; Holman, 2010). Details of the Ri calculation can be found in Sect. S3 of the supporting information.

To investigate the non-isothermal effect on fluid dynamics ~~inside~~within the PAM-OFR, the simulated flow distributions with and without heating effects are demonstrated in Figs. 7c-j. As illustrated in Figs. 7c-d, the flow velocity ~~of flow is highest after~~peaked following injection through an inlet diffuser, resulting in recirculation near the edge of the walls. The other place showing a higher air velocity ~~of air is~~was around the output of exit (Figs. 7d and S10), which ~~is~~was generally used for particle output ~~measurement~~measurements. In addition to aerosol sampling, the air for gas phase measurements was usually sampled through a perforated ring flow manifold in the back of the PAM-OFR to obtain more even and better-mixed air (Fig. S1). Under the typical operating ~~condition~~conditions, the flow distribution when both gas and aerosol were sampled ~~might~~would be different from that when only the aerosol line was applied. However, ~~adding the extra output of~~incorporating the additional gas phase ~~would greatly add~~output significantly increases to the complexity of this CFD simulation. Thus, to simplify the simulation, we ~~set~~designated the airflow to be ~~only~~ sampled solely through the exit port located ~~in~~at the center of the OFR backplate. Moreover, ~~when~~variations in the flow ratio between gas and aerosol lines ~~is different,~~would alter the flow distribution ~~inside~~within the PAM-OFR ~~would be changed~~.

~~When~~Upon activation of the UV light~~, there~~ was ~~on, the~~a significant alteration in flow distribution ~~changed substantially and had more~~, characterized by an increased presence of flow bifurcation and recirculation, as shown in Figs. 7e and 7f. There ~~is~~was a ~~large~~pronounced recirculation in the lower ~~part~~region of the flow tube. ~~A clearer demonstration of the~~This recirculation ~~can be seen~~was further elucidated in Figs. 7g-j and Fig. S10. ~~When no~~In the absence of heat ~~effect was introduced in~~effects within the PAM-OFR, the 1-D flow profile generally exhibited symmetry in the vertical direction (Fig. 7h). A slight distortion on the 1-D flow profile in the horizontal direction ~~is~~was reasonable due to the influence of the random motion and pressure gradient of gas (Fig. 7g). ~~When~~In the presence of a vertical axial temperature gradient ~~exists~~, 1-D flow profiles ~~are~~exhibited a skewed pattern due to the buoyancy of the ~~warm~~warmer air. ~~The~~This recirculation effect manifested when the temperature gradient ~~is~~was larger, as well as when the flow rate ~~is~~was lower, ~~thus can~~leading to substantially ~~change~~alterations in both the residence time distribution (RTD) and its average value (τ_{avg}). τ_{avg} can be calculated as the sum of the integrals of signal (such as the signal of SO_2 after introducing SO_2 pulses) over time versus the sum of the signals (Huang et al., 2017).
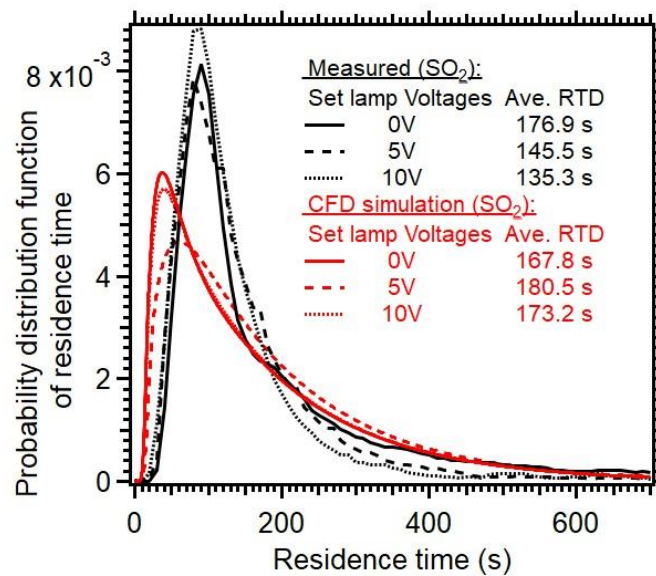
The average RTD values ~~inside~~within the PAM-OFR under heat and non-heat scenarios were also measured and simulated in Fig. 8. Similar to the modeled results in Huang et al. (2017) and the measured results in Lambe et al. (2019),

15

the measured RTDs under higher temperatures in this study exhibit shorter τ_{avg} (135-145 s at 5-10 V vs~~.~~ 177 s at 0 V) due to the acceleration of air upon heating. ~~The~~This acceleration ~~is~~was mainly reflected in the early arrival time and shorter tails, as shown in Fig. 8. Huang et al. (2017) found that ~~when the flow tube is under non-isothermal conditions~~ even ~~a~~

~~small~~minor temperature ~~deviation~~deviations (0.2 °C) ~~can create~~in non-isothermal conditions could induce secondary ~~flow thus~~flows, thereby significantly affecting the RTD and τ_{avg} ~~substantially.~~. The RTD variation ~~of the RTD~~when lamps were turned on and off ~~was~~were also simulated in the CFD model, as shown in Fig. 8. Compared with the measured results, the simulated RTD generally ~~shows~~exhibited an ~~early~~earlier arrival time and broader distribution at different light settings. The simulated τ_{avg} upon heating (173-180 s) ~~is higher than~~exceeded the value when lights were off (167 s), indicating that

the recirculation in the model introduced by heating ~~prolongs~~prolonged the τ_{avg} rather than reducing ~~the τ_{avg}. The higher~~ ~~τ_{avg} when lamps were on than off contrasts with the~~it. This discrepancy from the observed trend ~~found~~ in ~~the measured~~ τ_{avg} (Huang et al., 2017; Lambe et al., 2019) could be attributed to that the recirculation was weighted more in the calculation than the real conditions, which also ~~emphasizes~~underscored the ~~challenge~~complexities of accurately simulating the orthogonal forces ~~caused~~induced by ~~the forced convection by the~~both pressure gradient-driven forced convection

(horizontal) and buoyancy-induced free convection (vertical) (Huang et al., 2017). Note the simulated τ_{avg} under a lamp setting of 10 V (173 s) ~~is~~was lower than the τ_{avg} under 5 V (180 s~~), the~~). This trend ~~of which is consistent~~aligned with the measured results, suggesting the ~~enhanced~~increased gas diffusion upon heating was properly considered except the recirculation.
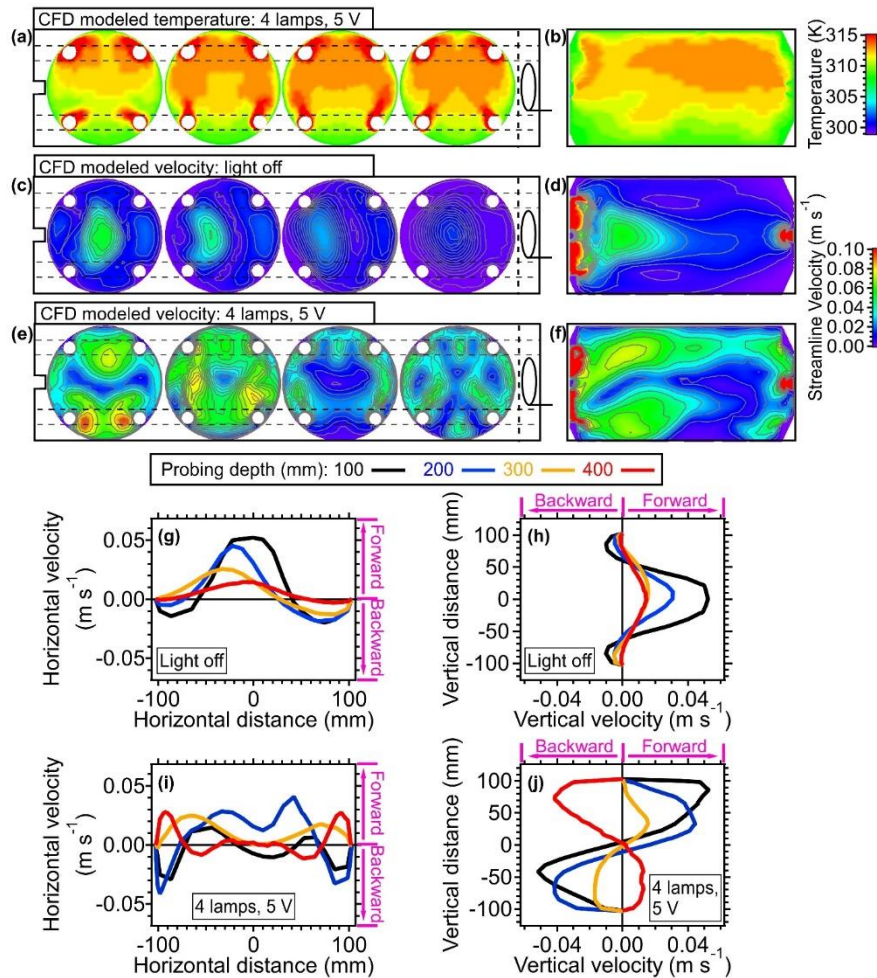
Figure 7: (a) Three-dimensional simulation results demonstrating the cross-sectional temperature profiles. ~~–~~(b) Simulated lateral temperature profile inside of the OFR based on CFD simulation. ~~–~~Panel (a) and (b) were simulated with conditions that four lamps were set to be 5 V.~~–~~ (c) Three-dimensional simulation results illustrating cross-sectional velocity profiles and (d) lateral velocity profiles based on CFD simulation results. Panel (c) and (d) were simulated with conditions that lamps ~~are~~were off (room temperature: 25 ℃). (e-f) the same plots as panels (c~~) and~~ ~~(-~~d) with four lamps ~~being~~ set ~~on~~to 5 ~~volts. Enhanced temperature influences in panels (e) and (d) were considered~~V. One-dimensional velocity profiles at (g) horizontal and (h) vertical directions inside the OFR at room temperature, ~~One~~and one-dimensional velocity profiles at (i) horizontal and (h) vertical directions ~~under~~with four lamps ~~being~~ set to 5 ~~volts~~V.

In summary, the heating introduced from four lamps set to 5 V ~~can decrease~~decreased τ_{avg} by 18-23% ~~relative~~in comparison to dark OFR experimental conditions. This ~~is~~was considered as an upper limit variation on τ_{avg} for a typical OFR setting where the ~~voltage of lamps was~~lamp voltages were usually below 3 V to obtain OH exposures of less than 5 days. The variation of RTD ~~changes~~altered the exposure time of gas/aerosol species ~~in~~within the PAM-OFR, which ~~can~~could impact the gas and particle oxidation conditions. In the following sections, this impact will be systematically discussed.


Figure 8: Residence time distribution (RTD) of SO₂ ~~inside~~within the PAM-OFR under different lamp settings. A 2 s pulser of SO₂ was injected into the OFR. The average RTD values were also estimated here. The simulated results from CFD models ~~are~~were shown in red lines.

3.3 Temperature influence on gas-phase reaction and OH exposure

In this section, the temperature influence on gas-phase reactions was systematically investigated. We ~~take~~took the oxidation of SO₂ ~~inside~~within OFR as an example to simulate its gas-phase reaction with oxidants (mainly OH) ~~under~~across a temperature range ~~from~~of 25 °C to 40 °C (binned with 5 °C) using the KinSim Model. The ~~25 °C~~simulation ~~represents~~at 25 °C emulated the typical laboratory ~~condition~~conditions, while 40 °C ~~was~~simulation represented the approximate temperature observed at the upper limit of lamp voltage (5-10 V, ~~corresponds~~corresponded to photochemical age ~10-30

17

520 days, Fig. 2). In addition, to account for the RTD influences on gas-phase ~~reaction~~reactions under different temperatures, the scenarios with measured RTD distributions under 25 °**C** and 40 °**C** were both simulated here.

In general, when the temperature variation ~~inside of~~within OFR (the same RTD as measured at 25 °C being applied for cases at different temperatures) was considered, the influences of temperature ~~enhancement~~increase due to lamp heating on the gas-phase reaction rate ~~are very minor.~~were minimal. The ~~concentration~~concentrations of OH, HO$_2$, O$_3$, and O(^{1}D)

525 all showed a maximum of ~5% increase at the highest photon flux, which ~~is~~was consistent with the simulated results using the same KinSim model in Li et al. (2015). The SO$_2$ decay and OH exposure also ~~show~~showed negligible variations in the model (Fig. 9e and 9f). When the temperature influences on the RTD were taken into account, the variation trend of oxidant concentration was mixed due to the combined negative effect of the reduced average residence time (τ_{avg}) and the positive effect of temperature on oxidant concentration (Li et al., 2015). The parameter ~~that was~~most influenced ~~is~~was OH exposure,

530 which ~~shows~~showed 18-20% lower values at 40 °**C** than at 25 °**C** due to the shorter residence time (τ_{avg}) upon heating. Our ~~result suggests the~~results suggested that an increase ~~of~~in temperature ~~inside of~~within OFR due to lamp heating would have a ~~very minor~~minimal to negligible impact on ~~the~~ gas-phase reactions, whereas parameters related to the RTD distribution (e.g., OH exposure) ~~shall~~should be considered in the current and future experiments.
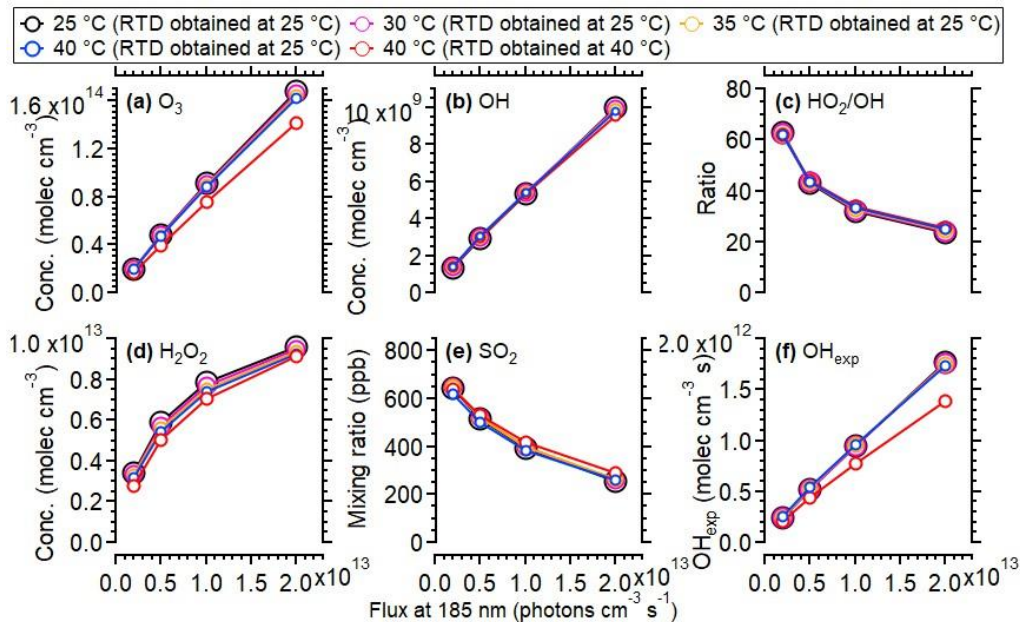
535 **Figure 9: Simulated concentrations of different oxidants from 25 to 40 °C ~~in~~within the OFR ~~based on~~utilizing the radical mechanism of the KinSim model. 800 ppb of initial SO₂ and 2.2% water vapor mixing ratio (25 °C, 70% RH) were used. The simulated results using measured RTD at 25 and 40 °C ~~are also~~were both shown.**

3.4 Temperature influence on ~~SOA formation~~the evaporation of ambient OA

~~The temperature can influence the SOA formation through changing gas/particle partitioning and RO₂ fate, thus~~

540 ~~affecting the SOA yield and chemical composition (Takekawa et al., 2003; Li et al., 2007; Zhang et al., 2015; Price et al.,~~ ~~2016; Quéléver et al., 2019; Kristensen et al., 2020; Atkinson et al., 1987).~~ Here, we estimated the ~~OA~~potential losses of input ambient OA due to evaporation under enhanced temperature in OFR. This estimation is mainly based on literature results and modeling work.

For the existing OA which is sampled into the OFR, the evaporation of input OA upon heating can be roughly estimated

545 based on the results ~~of~~from thermal denuder (TD) experiments~~, in which the~~. These experiments involved heating aerosols

18

~~were heated~~ from ambient/room temperatures (20-25 °**C**) to ~~higher~~elevated temperatures (typically 60-200 °**C**) ~~at~~over a typical residence time of 10-60 s (typically ~20 s) (Huffman et al., 2009; Xu et al., 2020; Hu et al., 2016; Saha et al., 2017; Kolesar et al., 2015; Saha and Grieshop, 2016; Lee et al., 2011). Previous studies suggest the evaporation of aerosol is kinetically limited, which varies with temperature, residence time, OA mass and volatility, phase state and dissociation rates for oligomers (Cappa, 2010; Riipinen et al., 2010; Roldin et al., 2014; Schobesberger et al., 2018). Based on the previous TD studies, ~~the~~an evaporation rate of 1×10^{-4}-2.5×10^{-4} per (°**C**·second) was usually observed under 50 °**C** of TD for ambient OA (typical average mass concentration: 10-30 µg m^{-3}) (Huffman et al., 2009; Feng et al., 2023; Paciga et al., 2016). In an OFR experiment conducted on an aircraft, Nault et al. (2018) found an average mass loss of ambient OA ~~is~~was ~32% due to ~~enhanced~~increased temperature in a dark OFR compared to the unperturbed air sampled (+17 °**C** on average) at a residence time of 150 s. ~~That~~This OFR experiment showed an evaporation rate of 1.2×10^{-4} per (°**C**·second), which ~~is~~was within the range of reported values obtained ~~with~~from the higher temperature TD experiments (1×10^{-4}-2.5×10^{-4} per (°**C**·second)). Theoretically, when the temperature enhancement was assumed to be ~5 °**C** and a residence time of 160 s was applied, a mass loss of 8-20% was estimated for ambient OA in OFR. The ~~enhanced~~increased temperature ~~inside of~~within OFR ~~might~~would also impact other semi-volatile inorganic species, e.g., ammonium nitrate (Heim et al., 2020).

3.5 Temperature influence on the SOA formation

The temperature can influence the SOA formation through changing gas/particle partitioning and RO$_2$ fate, thus affecting the SOA yield and chemical composition (Takekawa et al., 2003; Li et al., 2007; Zhang et al., 2015; Price et al., 2016; Quéléver et al., 2019; Kristensen et al., 2020; Atkinson et al., 1987). Obvious SOA decrease mass was observed in OFR at different temperatures.

For the newly formed SOA in the OFR, the temperature impact was simulated based on the SOM model (He et al., 2022; Eluri et al., 2018). Specifically, the kinetic phase partitioning of SOA generated via OH-oxidation of typical ambient VOCs was simulated (Figs. 10-11, S12-17) as a function of OFR temperature ranging from 20-40 °**C** (binned in 5 °**C**) and OA mass concentration from 1 to 80 µg m^{-3}. ~~ ~~Note that the results, including SOA yield, size distribution, and O:C ratio for n-dodecane (Figs. 10 and 11), α-pinene (Figs. S12 and S15), toluene (Figs. S13 and S16) and m-xylene (Figs. S14 and S17~~)~~), were examined under both high NOx and low NOx conditions. For dodecane, the simulated temperature-dependent SOA under high NOx condition in the SOM model was generally ~~is~~consistent with the chamber results ~~obtained~~presented in Lamkaddam et al. (2017).

Generally, the higher temperatures result in lower SOA yields due to the increased evaporation of gas-phase products (Hildebrandt et al., 2009; Warren et al., 2009; Qi et al., 2010; Denjean et al., 2015). As shown in Figs. 10a and S12-S14, when RTD at 25 °**C** was used for different temperatures, the SOA yield of different VOC species including dodecane, α-pinene, toluene, and xylene ~~can~~could decrease by ~~~~~20% for a typical temperature ~~enhancement~~increase of 5 °**C** in the OFR, and by up to 40-50% at 40 °**C** compared to the values at a typical 25 °**C** under high NOx condition. This ~~decrease~~decline in SOA yield ~~signifies the substantial influences of~~indicated significant temperature effects on SOA formation ~~inside of~~within the OFR due to heating. To confirm the model results, we did a simple laboratory experiment and found the formed SOA masses was indeed substantially decreased in OFR due to the heating effect (Fig. S19), which is consistent with the simulated model results. The simulated particle size also ~~shows~~showed decreases as the OFR temperature ~~goes up~~increased. The higher SOA mass and larger size of particles formed at lower temperatures ~~are~~were consistent with more gas-to-particle phase partitioning, and ~~have~~had also been observed in various temperature-controlled chamber studies

585 (Clark et al., 2016; Lamkaddam et al., 2017; Boyd et al., 2017; Gao et al., 2022; Pathak et al., 2007; Tillmann et al., 2010; Price et al., 2016; Kristensen et al., 2020). When the measured RTD at 40 °C was applied in the model, an even lower SOA yield was achieved due to the shorter residence time of reactants. However, this influence was weaker than the directly influences caused by the temperature increase on SOA formation. A decreased of ~8% of dodecane SOA yield was found at 40 °C under high NOx condition and 10% under low NOx compared to the results with RTD measured at 25 °C (Fig.

590 10). Under low NOx conditions, a smaller reduction in size distribution (Fig. 11 and Figs. S15-S17) and SOA yield, which arewere 5-10% for a temperature enhancementincrease of 5 °C and up to 15-35% for 15 °C as shown in Fig. 10 and Figs. S12-S14), was found compared withto high NOx conditions. TheThis smaller reduction was mainly due to the formation of more SOA with lower volatility being formed under low NOx conditions (e.g., acids, hydroperoxide) than theunder high NOx conditions (Kroll and Seinfeld, 2008; Srivastava et al., 2022; Presto et al., 2005; Aruffo et al., 2022). The parameters

595 of the SOM model were obtained based on fitting the results to the chamber results under high and low NOx conditions, respectively (Eluri et al., 2018; Cappa et al., 2016), thus, thethese parameters were set such that the volatility of SOA decreasesdecreased larger as a function of the functional groups added under low NOx conditionconditions than theunder high NOx conditionconditions (Cappa et al., 2013). Note that in the model we did not specifically treat the RO_2 fate e.g., a varied fraction of highly oxygenated organic molecules from autoxidation underat different temperatures. Using a constant

600 yield for HOMs in the model mightcould lead to a lower HOMs mass fraction in total SOA underat high temperatures, which would result in an underestimation of the oxidation level and an overestimation of the volatility of SOA formed under low NOx conditions (Bianchi et al., 2019). In addition, the wall loss was corrected in the SOM model with a constant wall loss rate of 2.5×10^{-3} s^{-1}, which has been verified in the comparison of SOA model work between OFR and chamber studies (He et al., 2022). In theory, when the temperature of the OFR tube increasesincreased, the wall loss rate of low

605 volatile organic compounds shallshould be smaller than under ambient temperature. Therefore, using a constant wall loss rate here mightwould underestimate the SOA yield.

In previous studies, to correct forthe heating effects on SOA yield, Chen et al. (2013) and Lambe et al. (2015b) correctedadjusted the SOA yield by 2% per K of temperature riseincrease relative to 298 K (Stanier et al., 2008). However, this is a rough correction, because the SOA yields of different precursors and reaction conditions are affected by

610 temperature by different amounts.in varying degrees. For example, 0.41-0.52% per K was found for dodecane under high NOx conditions based on the SOM model while 0.87-0.89% per K was found for α-pinene (Table S4). Note that in the OFR experiments, the decreasereduction of SOA yield mightcould be even larger due to the potential mass loss of seed OA upon heating in the OFR. The simulated results from the SOM model here provideprovided an approximate reference to help recalibrate the SOA formation inside of OFRs. As theThe detailed numbers calculated by the SOM model for

615 different species under high and low NOx conditions can be seen in Table S4. For a specific recalibration, e.g., mixed precursors, a more detailed model or temperature-controlled experiments considering the mixing effect of precursors can be performed (Mcfiggans et al., 2019).

For the SOA chemical composition, the higher temperature insidewithin the OFR resultsled to an increase in increased O:C ratios of SOA, e.g., ~0.35 (25 °C) vs. ~0.42 (40 °C) in dodecane experiments under high NOx conditions and ~0.23

620 (25 °C) vs. ~0.28 (40 °C) under low NOx condition. The enhancedincreased O:C ratio under higher temperatures was also found in the chamber results for m-xylene/NOx photooxidation in Qi et al. (2010) and O_3 oxidation of α-pinene in Denjean et al. (2015). The higher O:C underat higher temperatures was probably caused by the evaporation of semi-volatile and less-oxidized components with increased temperatures (Clark et al., 2016; Gao et al., 2022).
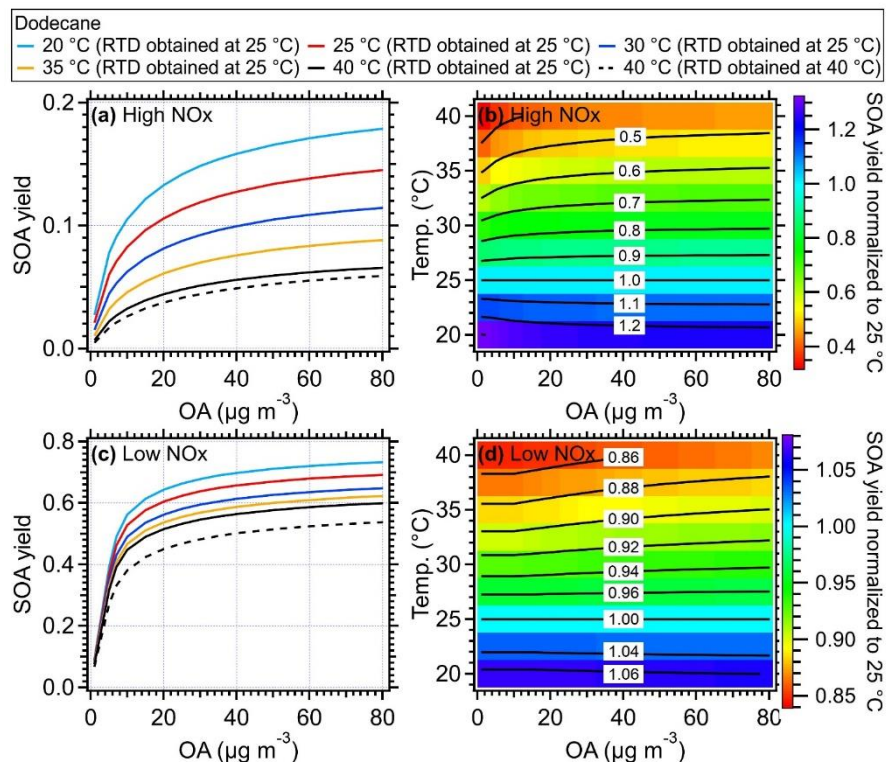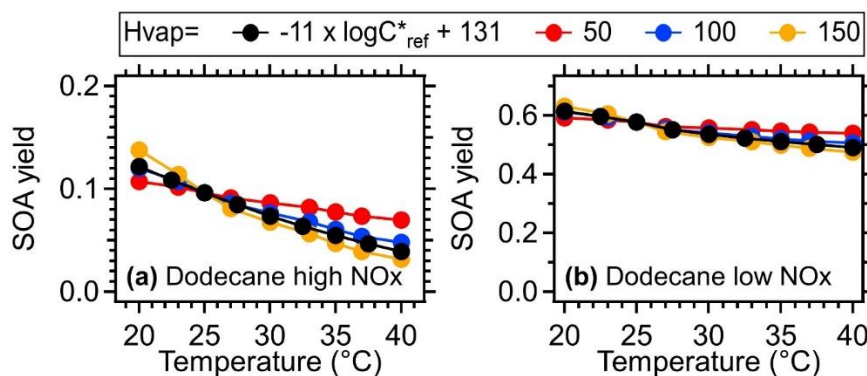
Figure 10: Simulated SOA yield of dodecane as a function of mass concentration of organic aerosol and temperature ~~inside~~within the OFR ~~for~~under (a) high NOx and (c) low NOx conditions, respectively. The simulated results using the measured RTD obtained at 40 °C ~~are~~were shown as black dashed lines. The ratio of SOA yield of dodecane from different temperatures compared to that of 25 °C under (b) high NOx and (d) low NOx conditions. The equivalent aging time ~~is~~was 1 day by assuming the OH concentration ~~is equivalent~~equated to 1.5×10^{6} molecule cm^{−3} (Mao et al., 2009).

In the model, the evaporated SOA mass as a function of temperature was mainly determined by the enthalpy (H_i^{vap}), as described by the Clausius–Clapeyron Equation (~~E.q~~Eq. (1)). A ~~varied~~variable enthalpy H_i^{vap} dependent on saturation concentration (C*, $H_i^{vap} = -11 \times log C_{ref}^*$) was applied as the default setting based on Epstein et al. (2010). Various experimental studies using ~~thermodenuder for measuring~~thermodenuders to measure OA volatility ~~show~~showed that the ambient H_i^{vap} for OA ~~might vary in~~varied within a range of 50-150 kJ mol^{-1} (Epstein et al., 2010; Saha et al., 2017; Cappa and Jimenez, 2010). To further explore the sensitivity of temperature-dependent SOA formation ~~toward~~to enthalpy, we ~~demonstrate~~demonstrated the SOA yield as a function of temperature under constant H_i^{vap} values in Fig. 12 and S18. The results ~~suggest~~suggested that the SOA yield obtained with ~~varied~~varying H_i^{vap} ~~is~~was generally ~~similar~~comparable to that when a constant H_i^{vap} of 100 kJ mol^{-1} was applied, which is the most commonly reported H_i^{vap} for ambient OA. Higher H_i^{vap} suggests that the SOA formation is more sensitive to the temperatures. When the upper (150 kJ mol^{-1}) and lower limit (50 kJ mol^{-1}) of H_i^{vap} ~~are~~were applied, the simulated results of SOA yield ~~suggest~~suggested a maximum of 22% and 90% variation, respectively, under high NOx ~~condition~~conditions and 18% and 42% variation, respectively, for low NOx ~~condition~~conditions based on different species and ~~temperature~~temperatures.
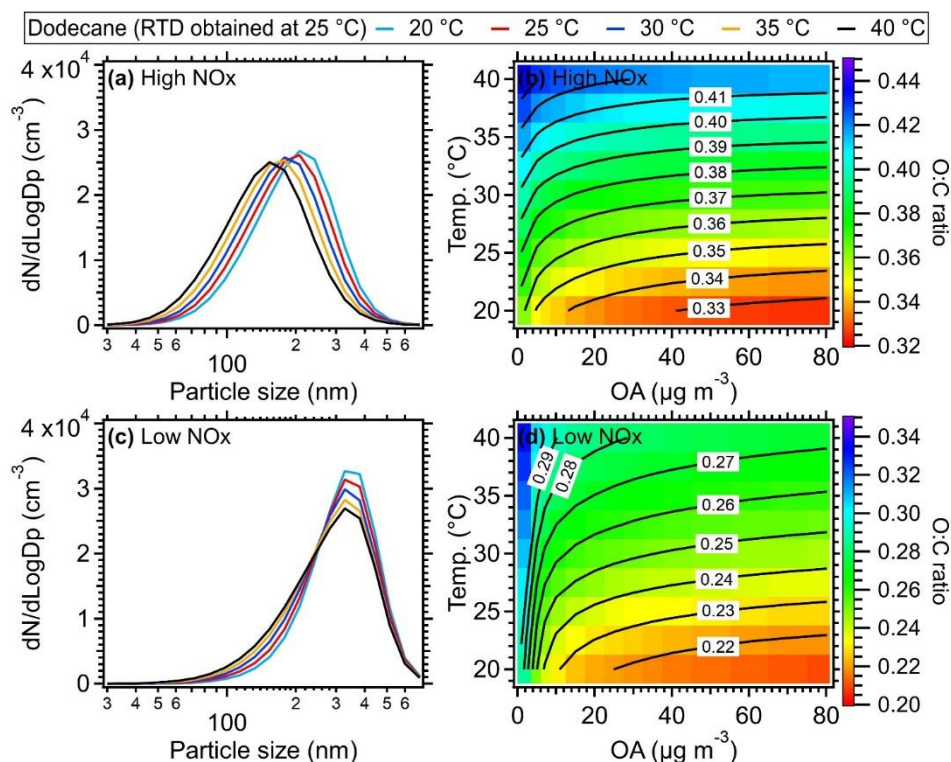
Figure 11: Size distribution of dodecane under different temperatures and 30 μg m^{-3} organic aerosol for (a) high NOx and (c) low NOx conditions, respectively. The O:C ratio of dodecane under different temperatures and organic aerosol concentration under (b) high and (d) low NOx conditions. The equivalent aging time ~~is~~was 1 day by assuming the OH concentration ~~is equivalent~~equated to 1.5×10^6 molecule cm^{-3} (Mao et al., 2009).

Figure 12: SOA yield of dodecane as a function of temperature under different H_i^{vap} values (Unit: kJ mol^{-1}). The mass concentration of organic aerosol ~~is~~was assumed to be 15 μg m^{-3}. The equivalent aging time ~~is~~was 1 day by assuming the OH concentration ~~is equivalent~~equated to 1.5×10^6 molecule cm^{-3} (Mao et al., 2009).

In addition to the direct influences, the increase of temperature within OFR decreases the relative humidity (RH), which can also impact SOA formation. However, the literatures show that the impact of RH on SOA formation remains inconclusive. For example, Tillmann et al. (2010) found the SOA yield was higher at humid conditions (RH: 40-70%) compared to dry conditions (RH: 0-10%) as the RH influenced the formation of products in α-pinene ozonolysis experiments. In contrast, Zhang et al. (2019) found the SOA yield of m-xylene-OH oxidation decreased as RH increased in a chamber study, as the high RH led to the less formation of oligomers and inhibited the reaction of RO$_2$ autoxidation. Thus, elucidating the influence of humidity on various SOA formations is still a challenge and falls outside the purview of

660 our research topic here. In addition, given the short residence time within OFR (seconds to minutes), the impact of liquid phase reactions to SOA formation should be minimal.

In summary, the heating effect ~~introduced~~induced by the lamps ~~can have an important impact on~~could significantly influence the SOA formation ~~inside of~~within OFR for certain high-OH exposure applications~~, which shows~~. This showed varied extents for different precursors and reaction conditions. ~~The simulated~~Simulation results ~~suggest~~suggested that the
665 ~~deceased~~decreased ratio of SOA output ~~vs~~to preexisting OA at higher OH exposures (e.g., equivalent aging time >~5 days under low NOx conditions) observed in previous ~~experiments~~studies (Hu et al., 2022; Lambe et al., 2015a; Ortega et al., 2016; Palm et al., 2016; Saha et al., 2018) ~~might~~may not only due to heterogeneous ~~reaction~~reactions and/or enhanced gas-phase reaction~~, but~~. Instead, it could also ~~probably caused by~~be attributed to the heating evaporation. However, the yield and ambient OFR results under equivalent aging time <~4 days ~~shall still~~should be remained valid (Palm et al., 2018). The
670 ~~enhanced~~ temperature ~~might~~increase would also impact the phase of aerosols by changing the chemical composition of OA (viscosity, O:C, etc.), as the PAM-OFR temperature ~~covers~~covered the usual range of glass transition temperature of ambient OA (2-87 °C) (Li et al., 2020b; Derieux et al., 2018). The impact of ~~enhanced~~ temperature increases on the phase state (i.e., viscosity) of aerosol phases, wall loss or other effects needs to be further studied.

3.~~5~~6 Approaches to reduce the heating effect

675 In the PAM-OFR, one approach to ~~reducing~~reduce the heating influence of the lamps is to ~~decrease~~shorten the OFR residence time, at the expense of decreasing the maximum achievable OH exposure and time available for LVOC condensation onto aerosols ~~(Peng and Jimenez (2020)~~(Peng and Jimenez, 2020). Another ~~approach~~method involves using fewer lamps ~~at~~with lower voltage settings; for example, using two lamps at less than 3 V maintains a temperature ~~enhancement~~increase of less than 5 °C while still achieving OH exposures of up to 5 days under low NOx conditions. In
680 addition, it can also be useful to ~~increase~~enhance heat transfer away from the PAM-OFR~~,~~ to reduce its operating temperature e.g., blowing air with fans or air conditioners. To ~~test~~verify this, we used two ~~big~~large fans (45 cm in diameter at a distance of 30 cm from the PAM-OFR) ~~pointed to~~directed towards the lower parts of the PAM-OFR. We found the maximum delta temperature (OFR minus ambient air) for a typical high light setting decreased from 16 °C to 7 °C (44% deduction), as shown in Fig. 13. ~~That test showed~~This experiment demonstrated that blowing the flow tube with fans is ~~a~~
685 ~~very efficient~~an extremely effective way to ~~offset~~compensate for the ~~lamps~~lamp heating, and is simple ~~with no~~without major trade-offs. ~~Designing~~Moving the UV lamps outside the tube and designing a cooling system on the outer surface of OFR ~~by using~~with circulating water or cold air ~~might~~can also be ~~a good way~~effective ways to ~~better control~~improve the temperature control inside of OFR (Watne et al., 2018; Xu and Collins, 2021; Huang et al., 2017; Liu et al., 2018; Chu et al., 2016; Zhao et al., 2021; Li et al., 2019), however, ~~it would~~these will require a substantial redesign of the hardware of
690 OFR tubes and are beyond the scope of this manuscript. And mounting the lamps outside of the OFR limits the use of OFR185 mode due to the low transmission efficiency of quartz glass for light at 185 nm (Simonen et al., 2017) and OFR254 mode is usually used. Cooling down the OFR would also affect RTD since the heater transfer occurs via convection inside of OFR, which needs to be further investigated in the future.
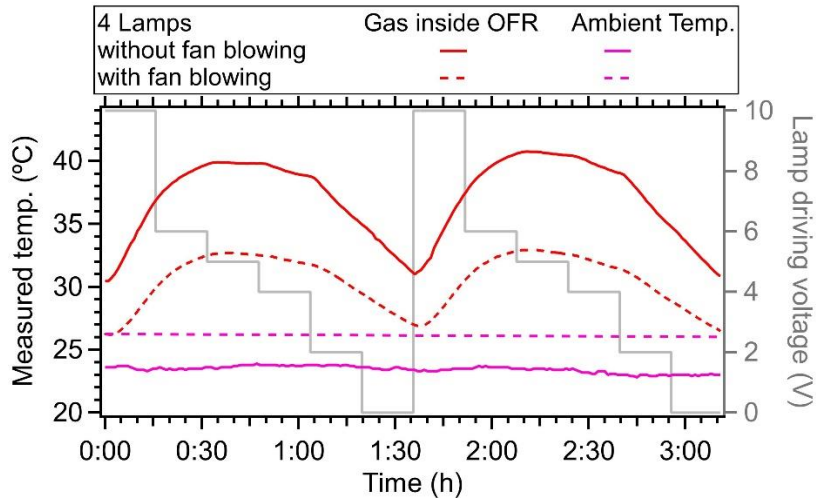
Figure 13: The measured temperature in OFR with or without fan bellowing on the flow tube in the laboratory. The ambient temperature was also shown. Two fans were used, with a diameter of 45 cm and a rotation rate of 1400 r min^{-1}.
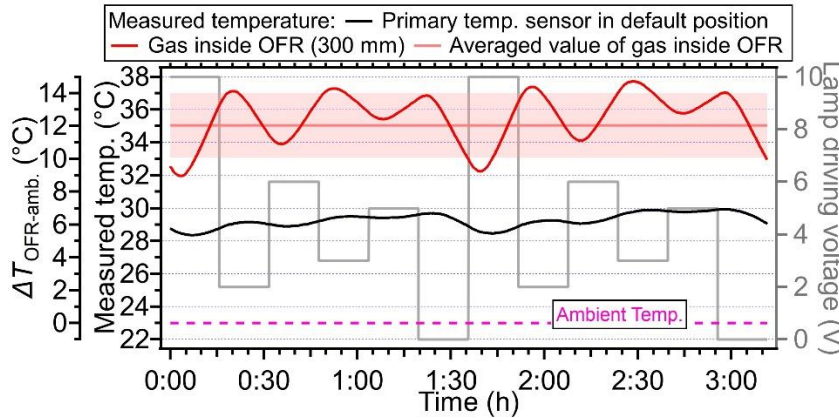
Figure 14: The measured temperature variation when lamp driving voltage cycles were set in a non-monotonic pattern (10-2-6-3-5-0 V for one cycle). The red line and shading ~~are~~were the average temperature and standard deviation (35.05±1.97 °C) measured at the centerline (probing distance: 300 mm) inside ~~the PAM-~~OFR. The purple dotted lines ~~represent~~represented the ambient temperature. Each lamp voltage was set for 16 min.

24
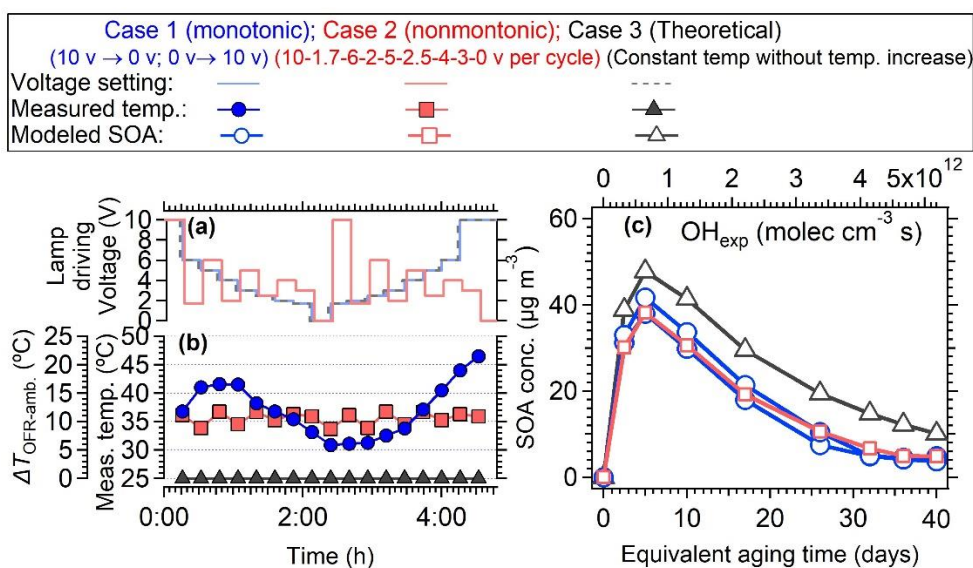
Figure 15: (a, b) The temperature variation with lamp driving voltage ~~is~~was **explored using a monotone (10→0→10V) and non-monotone pattern lamp power change pattern, respectively. (c) the modeled SOA formation from oxidation of 10 ppb toluene (OM=30 μg m⁻³) with OH radicals as a function of OH exposure. The SOA formation under monotone and non-monotone scenarios** ~~are~~were **both simulated. The case 3 of "theoretical" indicates the temperature** ~~were~~was **set to be constant (i.e., 25 ℃).**

The voltage setting strategy in the PAM-OFR also can be improved. In most of the OFR laboratory and field studies, OFR users usually changed the light setting monotonously from 0 to 10 V or from 10 to 0 V, which ~~results~~resulted in a continuously changing temperature ~~inside of~~within the PAM-OFR (Fig. 2, Fig. 5 and Fig. S4), therefore resulting in a variable SOA formation yield ~~under~~at different temperatures (Fig. 10). To mitigate the variable heating effect, we suggest alternating between high and low voltage settings to minimize the heat accumulation. Fig. 14 ~~shows~~showed an example of such a light setting cycle using 10-2-6-3-5-0 V. In such a way, although the average temperature ~~inside of~~within the PAM-OFR ~~is~~was still higher than the ambient temperature, the variation of measured temperature ~~in~~within~~in~~ the PAM-OFR can be ~~kept~~maintained within a narrow range ~~and has~~, exhibiting a smaller temperature deviation (±1.97 ℃) compared to the usual settings (Fig. 14a, ±4.76 ℃). ~~Another advantage is that in such a way, the~~ Furthermore, this method allowed for less uncertainly in the variation trend of SOA yield as a function of OH exposure ~~would have fewer uncertainties~~ compared to those performed under monotonically increasing or decreasing light settings. As shown in Fig. 15c, when using the measured temperature to simulate the SOA formation from toluene in the OFR, the SOA showed two different trends (2-32% differences) when monotonic and non-monotonic light ~~settings~~setting cycles were applied. The SOA formed from the proposed non-monotonic lamp setting cycle ~~shows~~showed better agreement on ~~the variation of~~ mass concentration variation (Fig. 15c) and mass ratio (Fig. ~~S19~~S20) compared ~~with~~to the SOA formation at 25 ℃ (40.4-80.0% for non-monotone setting vs~~.~~. 32.9-87.3% for monotone setting), which would introduce fewer uncertainties in the SOA yield and other aspects, e.g., chemical composition.

4 Conclusion

We systematically measured the temperature distribution ~~inside of~~within the lamp-enclosed Aerodyne PAM oxidation flow reactor. ~~It is found~~Our findings indicated that the lamps ~~inside of~~within the PAM-OFR ~~create~~generated heating energy, thus leading to temperature increase ~~inside of~~within the PAM-OFR. ~~A brief summary of the temperature increase and its~~

730 ~~influencing factors can be found~~The rise in ~~Table A1. The enhanced~~ air temperature ~~increases as a function of~~was proportional to the ~~setting of~~ lamp driving voltage (OH exposures) and the number of lamps applied, ~~decreases as a function of~~while it decreased with increasing flow rate due to ~~a~~ shorter residence ~~time~~times at higher flows. The distribution of ~~enhanced~~this temperature increase varied ~~with~~depending on special ~~position due to~~positions, influenced by the complex ~~effects~~interplay of thermal transfer and flow mixing. With default lamps from Light Source Inc. installed, the temperature

735 increase of air in the PAM-OFR ~~is~~was generally below 5 °C (at central line) when the driving ~~voltage~~voltages of two lamps ~~is~~were below 3 V (typically < 5 days of equivalent atmospheric OH exposure under low-NOx conditions) and the flow rate ~~is~~was 5 L min^{-1} (average residence time, τ_{avg} ~~=~~=150-180 s). ~~T~~The ~~usage~~use of BHK lamps typically ~~yields~~resulted in a smaller temperature ~~enhancement~~increase in the PAM-OFR at the same ~~OH$_{exp}$~~OH exposure due to ~~its~~their lower power dissipation. The heating energy loss of the OFR system ~~is~~was mainly through the walls of the reaction chamber,

740 ~~then~~followed by exiting air ~~inside of~~within the PAM-OFR and/or purged nitrogen.

The impact of ~~the enhanced~~ temperature increase on the flow distribution, gas, and aerosol phase chemistry ~~inside of~~within the PAM-OFR was systematically evaluated. The pulsed tracer ~~measurement results suggest the enhanced~~measurements suggested that the increased temperature in the PAM-OFR ~~accelerates~~accelerated the diffusion, ~~thus resulting in~~leading to a shorter average residence time (τ_{avg}). Although box model simulation results ~~show~~showed

745 that the temperature increase in OFR ~~has~~had a negligible impact on gas-phase oxidant concentrations (<~5%), however, ~~has~~had a certain impact on the τ_{avg} related parameters, e.g., OH exposure (~20% ~~decreases results from~~decreased due to a temperature increase of 15 °C).

The increase of temperature has larger impacts on ~~the~~ aerosol phase chemistry than on ~~the~~ gas phase. When the ~~enhanced~~ temperature ~~inside~~increase within the OFR ~~is around~~was 5 °C at a flow rate of 5 L min^{-1}, the evaporation loss of

750 ambient OA was found to be 8-20% based on thermodenuder and field experiments. The simulation from the SOM model ~~suggests~~suggested the SOA yield from four typical precursors (n-dodecane, α-pinene, toluene, and m-xylene) ~~can~~could decrease <20% under high NOx conditions and <10% under low NOx conditions when the temperature in OFR ~~increases~~increased by 5 °C. ~~With the increase of~~As temperature increased, the size distributions also ~~show~~showed a substantial decrease while ~~increases in the~~while O:C ratios ~~were found.~~ showed an increase. This work

755 ~~demonstrates~~demonstrated the substantial influence of temperature on SOA formation and highlights the ~~need for consideration~~necessity of ~~the~~considering temperature ~~impact~~effects when using the PAM-OFR ~~as a tool~~ for ~~investigating~~ aerosol chemistry research. Based on the SOM model simulation results in Table S4, we recommend 0.19-1.6% and 0.26-3% per K for temperature effect correction for SOA yield from four typical precursors under high NOx and low NOx conditions, respectively.

760 In general, applying higher flow rate and lower lamp power, cooling the reactor with fans are recommended to keep the temperature ~~enhancement~~increase low in the OFR system. In addition, to control the variation of enhanced temperature introduced by the monotonic trend for lamp settings (e.g., 0→10 V or 10→0 V), we propose to set the voltage with high and low voltage alternatively (e.g., 10-2-6-3-5-0 V) to ~~improve~~reduce the heating accumulation and keep the temperature variation within a narrow range. In summary, our evaluation of the temperature ~~enhancement~~increase inside of lamp-

765 enclosed OFR helps to improve our understanding of flow distribution and chemistry inside of this ~~OFR~~ type of OFR, which can help to reduce the uncertainty of OFR usage in the future.

Appendix

Table A1: Summary on the effect of different dimensional factors on the temperature of air inside of OFR, as well as the impact of temperature enhancement on flow, gas and aerosol chemistry inside OFR.

Factors influence on temperature (T) of air inside OFR		
	Impact factors	**Effect**
Heating energy input	Driving voltage of lamps	Driving voltage↑ → T↑
	Number of lamps	NO. of lamp used ↑ → T↑
	Lamp types	No differences for the same brand
	Lamps lasting time	Time↑ → T↑ before balance
	Setting voltage sequence	Set voltage ↑ monotonically → T↑; Set voltage ↓ monotonically → usually delayed T ↑ peak
Heating energy loss	Flow rate (corresponds to Residence time distribution, RTD)	Flow rate ↑ (RTD ↓) →T↓
	N_2 purge air	Flow rate ↑ or N_2 temperature ↓ → T↓
	Surrounding T of OFR	Surrounding T↓ → T↓
	Metal tube temperature	Metal tube T↓ → T↓
Temperature distribution	Measured position	Closer to lamp sleeve → T↑
	Vertical	Generally, T ↑ in the upper position
	Horizontal	Symmetrically distributed.
	Probing depth	Probing depth↑→T↑ for ARI OFR; Probing depth↑→T↓ for Penn State OFR
Temperature influences on flow, gas, and aerosol chemistry		
	Factors being influenced	**Effect**
Flow	Average RTD	T↑ → RTD ↓
Gas-phase	absolute concentration of oxidants	T↑ → Minor impact (<5%)
	OH exposures	T↑→ OH exposure ↓
	HOM yield	T↑→ HOM yield ↑
Aerosol-phase	input/seed OA	T↑→ OA masses ↓
	SOA yield*	T↑→ SOA yield ↓
	Size distribution of SOA*	T↑→ Peak sizes ↓
	Oxidation level of SOA*	T↑→ Oxidation level ↓

770 *More impact on high NOx regime than low NOx regime.

References

Adams, P. J. and Seinfeld, J. H.: Predicting global aerosol size distributions in general circulation models, J Geophys Res-Atmos, 107, https://doi.org/10.1029/2001jd001010, 2002.

790 Ahlberg, E., Ausmeel, S., Eriksson, A., Holst, T., Karlsson, T., Brune, W. H., Frank, G., Roldin, P., Kristensson, A., and Svenningsson, B.: No Particle Mass Enhancement from Induced Atmospheric Ageing at a Rural Site in Northern Europe, Atmosphere, 10, 408, https://doi.org/10.3390/atmos10070408, 2019.

Akherati, A., Cappa, C. D., Kleeman, M. J., Docherty, K. S., Jimenez, J. L., Griffith, S. M., Dusanter, S., Stevens, P. S., and Jathar, S. H.: Simulating secondary organic aerosol in a regional air quality model using the statistical oxidation model –
795 Part 3: Assessing the influence of semi-volatile and intermediate-volatility organic compounds and NOx, Atmospheric Chemistry and Physics, 19, 4561-4594, https://doi.org/10.5194/acp-19-4561-2019, 2019.

Akherati, A., He, Y., Coggon, M. M., Koss, A. R., Hodshire, A. L., Sekimoto, K., Warneke, C., de Gouw, J., Yee, L., Seinfeld, J. H., Onasch, T. B., Herndon, S. C., Knighton, W. B., Cappa, C. D., Kleeman, M. J., Lim, C. Y., Kroll, J. H., Pierce, J. R., and Jathar, S. H.: Oxygenated Aromatic Compounds are Important Precursors of Secondary Organic Aerosol in Biomass-
800 Burning Emissions, Environ Sci Technol, 54, 8568-8579, https://doi.org/10.1021/acs.est.0c01345, 2020.

Aruffo, E., Wang, J., Ye, J., Ohno, P., Qin, Y., Stewart, M., McKinney, K., Di Carlo, P., and Martin, S. T.: Partitioning of Organonitrates in the Production of Secondary Organic Aerosols from alpha-Pinene Photo-Oxidation, Environ Sci Technol, 56, 5421-5429, https://doi.org/10.1021/acs.est.1c08380, 2022.

Atkinson, R., Aschmann, S., and Winer, A.: Alkyl nitrate formation from the reaction of a series of branched RO2 radicals
805 with NO as a function of temperature and pressure, Journal of Atmospheric Chemistry, 5, 91-102, https://doi.org/10.1007/bf00192505, 1987.

Bahreini, R., Middlebrook, A. M., Brock, C. A., de Gouw, J. A., McKeen, S. A., Williams, L. R., Daumit, K. E., Lambe, A. T., Massoli, P., Canagaratna, M. R., Ahmadov, R., Carrasquillo, A. J., Cross, E. S., Ervens, B., Holloway, J. S., Hunter, J. F., Onasch, T. B., Pollack, I. B., Roberts, J. M., Ryerson, T. B., Warneke, C., Davidovits, P., Worsnop, D. R., and Kroll, J.
810 H.: Mass spectral analysis of organic aerosol formed downwind of the Deepwater Horizon oil spill: field studies and laboratory confirmations, Environ Sci Technol, 46, 8025-8034, https://doi.org/10.1021/es301691k, 2012.

Bianchi, F., Kurten, T., Riva, M., Mohr, C., Rissanen, M. P., Roldin, P., Berndt, T., Crounse, J. D., Wennberg, P. O., Mentel, T. F., Wildt, J., Junninen, H., Jokinen, T., Kulmala, M., Worsnop, D. R., Thornton, J. A., Donahue, N., Kjaergaard, H. G., and Ehn, M.: Highly Oxygenated Organic Molecules (HOM) from Gas-Phase Autoxidation Involving Peroxy Radicals: A
815 Key Contributor to Atmospheric Aerosol, Chem Rev, 119, 3472-3509, https://doi.org/10.1021/acs.chemrev.8b00395, 2019.

Boyd, C. M., Nah, T., Xu, L., Berkemeier, T., and Ng, N. L.: Secondary Organic Aerosol (SOA) from Nitrate Radical Oxidation of Monoterpenes: Effects of Temperature, Dilution, and Humidity on Aerosol Formation, Mixing, and Evaporation, Environ Sci Technol, 51, 7831-7841, https://doi.org/10.1021/acs.est.7b01460, 2017.

Bruns, E. A., El Haddad, I., Keller, A., Klein, F., Kumar, N. K., Pieber, S. M., Corbin, J. C., Slowik, J. G., Brune, W. H.,
820 Baltensperger, U., and Prévôt, A. S. H.: Inter-comparison of laboratory smog chamber and flow reactor systems on organic aerosol yield and composition, Atmospheric Measurement Techniques, 8, 2315-2332, https://doi.org/10.5194/amt-8-2315-2015, 2015.

Burkholder, J. B., Sander, S. P., Abbatt, J., Barker, J. R., Cappa, C., Crounse, J. D., Dibble, T. S., Huie, R. E., Kolb, C. E., Kurylo, M. J., Orkin, V. L., Percival, C. J., Wilmouth, D. M., and Wine, P. H.: "Chemical Kinetics and Photochemical
825 Data for Use in Atmospheric Studies, Evaluation No. 19", JPL Publication 19-5, Jet Propulsion Laboratory, Pasadena, 2019 http://jpldataeval.jpl.nasa.gov.

Cappa, C. D.: A model of aerosol evaporation kinetics in a thermodenuder, Atmospheric Measurement Techniques, 3, 579-592, https://doi.org/10.5194/amt-3-579-2010, 2010.

Cappa, C. D. and Jimenez, J. L.: Quantitative estimates of the volatility of ambient organic aerosol, Atmospheric Chemistry
830 and Physics, 10, 5409-5424, https://doi.org/10.5194/acp-10-5409-2010, 2010.

Cappa, C. D. and Wilson, K. R.: Multi-generation gas-phase oxidation, equilibrium partitioning, and the formation and evolution of secondary organic aerosol, Atmospheric Chemistry and Physics, 12, 9505-9528, https://doi.org/10.5194/acp-12-9505-2012, 2012.

Cappa, C. D., Zhang, X., Loza, C. L., Craven, J. S., Yee, L. D., and Seinfeld, J. H.: Application of the Statistical Oxidation
835 Model (SOM) to Secondary Organic Aerosol formation from photooxidation of of C12 alkanes, Atmospheric Chemistry and Physics, 13, 1591-1606, https://doi.org/10.5194/acp-13-1591-2013, 2013.

Cappa, C. D., Jathar, S. H., Kleeman, M. J., Docherty, K. S., Jimenez, J. L., Seinfeld, J. H., and Wexler, A. S.: Simulating secondary organic aerosol in a regional air quality model using the statistical oxidation model – Part 2: Assessing the influence of vapor wall losses, Atmospheric Chemistry and Physics, 16, 3041-3059, https://doi.org/10.5194/acp-16-3041-
840 2016, 2016.

Carter, W., Cockeriii, D., Fitz, D., Malkina, I., Bumiller, K., Sauer, C., Pisano, J., Bufalino, C., and Song, C.: A new environmental chamber for evaluation of gas-phase chemical mechanisms and secondary aerosol formation, Atmospheric Environment, 39, 7768-7788, https://doi.org/10.1016/j.atmosenv.2005.08.040, 2005.

845 Charnawskas, J. C., Alpert, P. A., Lambe, A. T., Berkemeier, T., O'Brien, R. E., Massoli, P., Onasch, T. B., Shiraiwa, M., Moffet, R. C., Gilles, M. K., Davidovits, P., Worsnop, D. R., and Knopf, D. A.: Condensed-phase biogenic-anthropogenic interactions with implications for cold cloud formation, Faraday Discuss, 200, 165-194, https://doi.org/10.1039/c7fd00010c, 2017.

Chen, S., Brune, W. H., Lambe, A. T., Davidovits, P., and Onasch, T. B.: Modeling organic aerosol from the oxidation of α-pinene in a Potential Aerosol Mass (PAM) chamber, Atmospheric Chemistry and Physics, 13, 5017-5031,
850 https://doi.org/10.5194/acp-13-5017-2013, 2013.

Chen, W., Ye, Y., Hu, W., Zhou, H., Pan, T., Wang, Y., Song, W., Song, Q., Ye, C., Wang, C., Wang, B., Huang, S., Yuan, B., Zhu, M., Lian, X., Zhang, G., Bi, X., Jiang, F., Liu, J., Canonaco, F., Prevot, A. S. H., Shao, M., and Wang, X.: Real-Time Characterization of Aerosol Compositions, Sources, and Aging Processes in Guangzhou During PRIDE-GBA 2018 Campaign, Journal of Geophysical Research: Atmospheres, 126, e2021JD035114, https://doi.org/10.1029/2021jd035114,
855 2021.

Cheng, X., Chen, Q., Jie Li, Y., Zheng, Y., Liao, K., and Huang, G.: Highly oxygenated organic molecules produced by the oxidation of benzene and toluene in a wide range of OH exposure and NO<sub><i>x</i></sub> conditions, Atmospheric Chemistry and Physics, 21, 12005-12019, https://doi.org/10.5194/acp-21-12005-2021, 2021.

Chu, B., Liu, Y., Ma, Q., Ma, J., He, H., Wang, G., Cheng, S., and Wang, X.: Distinct potential aerosol masses under different
860 scenarios of transport at a suburban site of Beijing, J Environ Sci (China), 39, 52-61, https://doi.org/10.1016/j.jes.2015.11.003, 2016.

Clark, C. H., Kacarab, M., Nakao, S., Asa-Awuku, A., Sato, K., and Cocker, D. R., 3rd: Temperature Effects on Secondary Organic Aerosol (SOA) from the Dark Ozonolysis and Photo-Oxidation of Isoprene, Environ Sci Technol, 50, 5564-5571, https://doi.org/10.1021/acs.est.5b05524, 2016.

865 Cocker, D. R., 3rd, Flagan, R. C., and Seinfeld, J. H.: State-of-the-art chamber facility for studying atmospheric aerosol chemistry, Environ Sci Technol, 35, 2594-2601, https://doi.org/10.1021/es0019169, 2001.

Cooper, P. L. and Abbatt, J. P. D.: Heterogeneous Interactions of OH and HO2 Radicals with Surfaces Characteristic of Atmospheric Particulate Matter, The Journal of Physical Chemistry, 100, 2249-2254, https://doi.org/10.1021/jp952142z, 1996.

870 Denjean, C., Formenti, P., Picquet-Varrault, B., Camredon, M., Pangui, E., Zapf, P., Katrib, Y., Giorio, C., Tapparo, A., Temime-Roussel, B., Monod, A., Aumont, B., and Doussin, J. F.: Aging of secondary organic aerosol generated from the ozonolysis of α-pinene: effects of ozone, light and temperature, Atmospheric Chemistry and Physics, 15, 883-897, https://doi.org/10.5194/acp-15-883-2015, 2015.

DeRieux, W.-S. W., Li, Y., Lin, P., Laskin, J., Laskin, A., Bertram, A. K., Nizkorodov, S. A., and Shiraiwa, M.: Predicting
875 the glass transition temperature and viscosity of secondary organic material using molecular composition, Atmospheric Chemistry and Physics, 18, 6331-6351, https://doi.org/10.5194/acp-18-6331-2018, 2018.

Donahue, N. M., Robinson, A. L., Stanier, C. O., and Pandis, S. N.: Coupled partitioning, dilution, and chemical aging of semivolatile organics, Environ Sci Technol, 40, 2635-2643, https://doi.org/10.1021/es052297c, 2006.

Eluri, S., Cappa, C. D., Friedman, B., Farmer, D. K., and Jathar, S. H.: Modeling the formation and composition of secondary
880 organic aerosol from diesel exhaust using parameterized and semi-explicit chemistry and thermodynamic models, Atmospheric Chemistry and Physics, 18, 13813-13838, https://doi.org/10.5194/acp-18-13813-2018, 2018.

Epstein, S. A., Riipinen, I., and Donahue, N. M.: A semiempirical correlation between enthalpy of vaporization and saturation concentration for organic aerosol, Environ Sci Technol, 44, 743-748, https://doi.org/10.1021/es902497z, 2010.

Ezell, M. J., Johnson, S. N., Yu, Y., Perraud, V., Bruns, E. A., Alexander, M. L., Zelenyuk, A., Dabdub, D., and Finlayson-
885 Pitts, B. J.: A New Aerosol Flow System for Photochemical and Thermal Studies of Tropospheric Aerosols, Aerosol Science and Technology, 44, 329-338, https://doi.org/10.1080/02786821003639700, 2010.

Feng, S., Gao, D., Liao, F., Zhou, F., and Wang, X.: The health effects of ambient PM2.5 and potential mechanisms, Ecotoxicol Environ Saf, 128, 67-74, https://doi.org/10.1016/j.ecoenv.2016.01.030, 2016.

Feng, T., Wang, Y., Hu, W., Zhu, M., Song, W., Chen, W., Sang, Y., Fang, Z., Deng, W., Fang, H., Yu, X., Wu, C., Yuan,
890 B., Huang, S., Shao, M., Huang, X., He, L., Lee, Y. R., Huey, L. G., Canonaco, F., Prevot, A. S. H., and Wang, X.: Impact of aging on the sources, volatility, and viscosity of organic aerosols in Chinese outflows, Atmos. Chem. Phys., 23, 611-636, https://doi.org/10.5194/acp-23-611-2023, 2023.

Gao, L., Song, J., Mohr, C., Huang, W., Vallon, M., Jiang, F., Leisner, T., and Saathoff, H.: Kinetics, SOA yields and chemical composition of secondary organic aerosol from β-caryophyllene ozonolysis with and without nitrogen oxides between 213
895 and 313 K, Atmospheric Chemistry and Physics, 22, 6001-6020, https://doi.org/10.5194/acp-22-6001-2022, 2022.

George, I. J., Vlasenko, A., Slowik, J. G., Broekhuizen, K., and Abbatt, J. P. D.: Heterogeneous oxidation of saturated organic aerosols by hydroxyl radicals: uptake kinetics, condensed-phase products, and particle size change, Atmospheric Chemistry and Physics, 7, 4187-4201, https://doi.org/10.5194/acp-7-4187-2007, 2007.

Ghia, U., Ghia, K. N., and Shin, C. T.: High-Resolutions for incompressible flow using the Navier-Stokes equations and a
900 multigrid method, Journal of Computational Physics, 48, 387-411, https://doi.org/10.1016/0021-9991(82)90058-4, 1982.

Giauque, W. F. and Meads, P. F.: The Heat Capacities and Entropies of Aluminum and Copper from 15 to 300°K, Journal of the American Chemical Society, 63, 1897-1901, https://doi.org/10.1021/ja01852a027, 2002.

Hallquist, M., Wenger, J. C., Baltensperger, U., Rudich, Y., Simpson, D., Claeys, M., Dommen, J., Donahue, N. M., George, C., Goldstein, A. H., Hamilton, J. F., Herrmann, H., Hoffmann, T., Iinuma, Y., Jang, M., Jenkin, M. E., Jimenez, J. L.,
905   Kiendler-Scharr, A., Maenhaut, W., McFiggans, G., Mentel, T. F., Monod, A., Prévôt, A. S. H., Seinfeld, J. H., Surratt, J. D., Szmigielski, R., and Wildt, J.: The formation, properties and impact of secondary organic aerosol: current and emerging issues, Atmospheric Chemistry and Physics, 9, 5155-5236, https://doi.org/10.5194/acp-9-5155-2009, 2009.

Hanson, D. R. and Lovejoy, E. R.: The Reaction of ClONO2 with Submicrometer Sulfuric Acid Aerosol, Science, 267, 1326-1328, https://doi.org/10.1126/science.267.5202.1326, 1995.

910 He, Y., Lambe, A. T., Seinfeld, J. H., Cappa, C. D., Pierce, J. R., and Jathar, S. H.: Process-Level Modeling Can Simultaneously Explain Secondary Organic Aerosol Evolution in Chambers and Flow Reactors, Environ Sci Technol, 56, 6262-6273, https://doi.org/10.1021/acs.est.1c08520, 2022.

He, Y., Akherati, A., Nah, T., Ng, N. L., Garofalo, L. A., Farmer, D. K., Shiraiwa, M., Zaveri, R. A., Cappa, C. D., Pierce, J. R., and Jathar, S. H.: Particle Size Distribution Dynamics Can Help Constrain the Phase State of Secondary Organic
915   Aerosol, Environ Sci Technol, 55, 1466-1476, https://doi.org/10.1021/acs.est.0c05796, 2021.

Heim, E. W., Dibb, J., Scheuer, E., Jost, P. C., Nault, B. A., Jimenez, J. L., Peterson, D., Knote, C., Fenn, M., Hair, J., Beyersdorf, A. J., Corr, C., and Anderson, B. E.: Asian dust observed during KORUS-AQ facilitates the uptake and incorporation of soluble pollutants during transport to South Korea, Atmospheric Environment, 224, https://doi.org/10.1016/j.atmosenv.2020.117305, 2020.

920 Hildebrandt, L., Donahue, N. M., and Pandis, S. N.: High formation of secondary organic aerosol from the photo-oxidation of toluene, Atmospheric Chemistry and Physics, 9, 2973-2986, https://doi.org/10.5194/acp-9-2973-2009, 2009.

Hodshire, A. L., Palm, B. B., Alexander, M. L., Bian, Q., Campuzano-Jost, P., Cross, E. S., Day, D. A., de Sá, S. S., Guenther, A. B., Hansel, A., Hunter, J. F., Jud, W., Karl, T., Kim, S., Kroll, J. H., Park, J.-H., Peng, Z., Seco, R., Smith, J. N., Jimenez, J. L., and Pierce, J. R.: Constraining nucleation, condensation, and chemistry in oxidation flow reactors using size-
925   distribution measurements and aerosol microphysical modeling, Atmospheric Chemistry and Physics, 18, 12433-12460, https://doi.org/10.5194/acp-18-12433-2018, 2018.

Holman, J. P.: Heat Transfer, 10 edn, McGraw-Hill, New York, USA, 2010.

Hu, W., Palm, B. B., Day, D. A., Campuzano-Jost, P., Krechmer, J. E., Peng, Z., de Sá, S. S., Martin, S. T., Alexander, M. L., Baumann, K., Hacker, L., Kiendler-Scharr, A., Koss, A. R., de Gouw, J. A., Goldstein, A. H., Seco, R., Sjostedt, S. J.,
930   Park, J.-H., Guenther, A. B., Kim, S., Canonaco, F., Prévôt, A. S. H., Brune, W. H., and Jimenez, J. L.: Volatility and lifetime against OH heterogeneous reaction of ambient isoprene-epoxydiols-derived secondary organic aerosol (IEPOX-SOA), Atmospheric Chemistry and Physics, 16, 11563-11580, https://doi.org/10.5194/acp-16-11563-2016, 2016.

Hu, W., Zhou, H., Chen, W., Ye, Y., Pan, T., Wang, Y., Song, W., Zhang, H., Deng, W., Zhu, M., Wang, C., Wu, C., Ye, C., Wang, Z., Yuan, B., Huang, S., Shao, M., Peng, Z., Day, D. A., Campuzano-Jost, P., Lambe, A. T., Worsnop, D. R.,
935   Jimenez, J. L., and Wang, X.: Oxidation Flow Reactor Results in a Chinese Megacity Emphasize the Important Contribution of S/IVOCs to Ambient SOA Formation, Environ Sci Technol, 56, 6880-6893, https://doi.org/10.1021/acs.est.1c03155, 2022.

Huang, R. J., Zhang, Y., Bozzetti, C., Ho, K. F., Cao, J. J., Han, Y., Daellenbach, K. R., Slowik, J. G., Platt, S. M., Canonaco, F., Zotter, P., Wolf, R., Pieber, S. M., Bruns, E. A., Crippa, M., Ciarelli, G., Piazzalunga, A., Schwikowski, M., Abbaszade,
940   G., Schnelle-Kreis, J., Zimmermann, R., An, Z., Szidat, S., Baltensperger, U., El Haddad, I., and Prevot, A. S.: High secondary aerosol contribution to particulate pollution during haze events in China, Nature, 514, 218-222, https://doi.org/10.1038/nature13774, 2014.

Huang, Y., Coggon, M. M., Zhao, R., Lignell, H., Bauer, M. U., Flagan, R. C., and Seinfeld, J. H.: The Caltech Photooxidation Flow Tube reactor: design, fluid dynamics and characterization, Atmospheric Measurement Techniques, 10, 839-867,
945   https://doi.org/10.5194/amt-10-839-2017, 2017.

Huffman, J. A., Docherty, K. S., Aiken, A. C., Cubison, M. J., Ulbrich, I. M., DeCarlo, P. F., Sueper, D., Jayne, J. T., Worsnop, D. R., Ziemann, P. J., and Jimenez, J. L.: Chemically-resolved aerosol volatility measurements from two megacity field studies, Atmospheric Chemistry and Physics, 9, 7161-7182, https://doi.org/10.5194/acp-9-7161-2009, 2009.

Ihalainen, M., Tiitta, P., Czech, H., Yli-Pirilä, P., Hartikainen, A., Kortelainen, M., Tissari, J., Stengel, B., Sklorz, M.,
950   Suhonen, H., Lamberg, H., Leskinen, A., Kiendler-Scharr, A., Harndorf, H., Zimmermann, R., Jokiniemi, J., and Sippula, O.: A novel high-volume Photochemical Emission Aging flow tube Reactor (PEAR), Aerosol Science and Technology, 53, 276-294, https://doi.org/10.1080/02786826.2018.1559918, 2019.

Jathar, S. H., Cappa, C. D., Wexler, A. S., Seinfeld, J. H., and Kleeman, M. J.: Multi-generational oxidation model to simulate secondary organic aerosol in a 3-D air quality model, Geoscientific Model Development, 8, 2553-2567,
955   https://doi.org/10.5194/gmd-8-2553-2015, 2015.

Jathar, S. H., Cappa, C. D., Wexler, A. S., Seinfeld, J. H., and Kleeman, M. J.: Simulating secondary organic aerosol in a regional air quality model using the statistical oxidation model – Part 1: Assessing the influence of constrained multi-generational ageing, Atmospheric Chemistry and Physics, 16, 2309-2322, https://doi.org/10.5194/acp-16-2309-2016, 2016.

Jensen, L. N., Canagaratna, M. R., Kristensen, K., Quéléver, L. L. J., Rosati, B., Teiwes, R., Glasius, M., Pedersen, H. B.,
960   Ehn, M., and Bilde, M.: Temperature and volatile organic compound concentrations as controlling factors for chemical

composition of α-pinene-derived secondary organic aerosol, Atmospheric Chemistry and Physics, 21, 11545-11562, https://doi.org/10.5194/acp-21-11545-2021, 2021.

Jimenez, J. L., Canagaratna, M. R., Donahue, N. M., Prevot, A. S., Zhang, Q., Kroll, J. H., DeCarlo, P. F., Allan, J. D., Coe, H., Ng, N. L., Aiken, A. C., Docherty, K. S., Ulbrich, I. M., Grieshop, A. P., Robinson, A. L., Duplissy, J., Smith, J. D., Wilson, K. R., Lanz, V. A., Hueglin, C., Sun, Y. L., Tian, J., Laaksonen, A., Raatikainen, T., Rautiainen, J., Vaattovaara, P., Ehn, M., Kulmala, M., Tomlinson, J. M., Collins, D. R., Cubison, M. J., Dunlea, E. J., Huffman, J. A., Onasch, T. B., Alfarra, M. R., Williams, P. I., Bower, K., Kondo, Y., Schneider, J., Drewnick, F., Borrmann, S., Weimer, S., Demerjian, K., Salcedo, D., Cottrell, L., Griffin, R., Takami, A., Miyoshi, T., Hatakeyama, S., Shimono, A., Sun, J. Y., Zhang, Y. M., Dzepina, K., Kimmel, J. R., Sueper, D., Jayne, J. T., Herndon, S. C., Trimborn, A. M., Williams, L. R., Wood, E. C., Middlebrook, A. M., Kolb, C. E., Baltensperger, U., and Worsnop, D. R.: Evolution of organic aerosols in the atmosphere, Science, 326, 1525-1529, https://doi.org/10.1126/science.1180353, 2009.

Kang, E., Root, M. J., Toohey, D. W., and Brune, W. H.: Introducing the concept of Potential Aerosol Mass (PAM), Atmospheric Chemistry and Physics, 7, 5727-5744, https://doi.org/10.5194/acp-7-5727-2007, 2007.

Kang, E., Lee, M., Brune, W. H., Lee, T., Park, T., Ahn, J., and Shang, X.: Photochemical aging of aerosol particles in different air masses arriving at Baengnyeong Island, Korea, Atmospheric Chemistry and Physics, 18, 6661-6677, https://doi.org/10.5194/acp-18-6661-2018, 2018.

Katrib, Y., Biskos, G., Buseck, P. R., Davidovits, P., Jayne, J. T., Mochida, M., Wise, M. E., Worsnop, D. R., and Martin, S. T.: Ozonolysis of mixed oleic-acid/stearic-acid particles: reaction kinetics and chemical morphology, J Phys Chem A, 109, 10910-10919, https://doi.org/10.1021/jp054714d, 2005.

Keller, A., Kalbermatter, D. M., Wolfer, K., Specht, P., Steigmeier, P., Resch, J., Kalberer, M., Hammer, T., and Vasilatou, K.: The organic coating unit, an all-in-one system for reproducible generation of secondary organic matter aerosol, Aerosol Science and Technology, 56, 947-958, https://doi.org/10.1080/02786826.2022.2110448, 2022.

Khalaj, F., Rivas-Ubach, A., Anderton, C. R., China, S., Mooney, K., and Faiola, C. L.: Acyclic Terpenes Reduce Secondary Organic Aerosol Formation from Emissions of a Riparian Shrub, ACS Earth and Space Chemistry, 5, 1242-1253, https://doi.org/10.1021/acsearthspacechem.0c00300, 2021.

Kieffer, W. F.: Tables of thermal properties of gases, Journal of Chemical Education, 33, A477, https://doi.org/10.1021/ed033pA477.1, 1956.

Klyta, J. and Czaplicka, M.: Determination of secondary organic aerosol in particulate matter – Short review, Microchemical Journal, 157, https://doi.org/10.1016/j.microc.2020.104997, 2020.

Knopf, D. A., Anthony, L. M., and Bertram, A. K.: Reactive uptake of O3 by multicomponent and multiphase mixtures containing oleic acid, J Phys Chem A, 109, 5579-5589, https://doi.org/10.1021/jp0512513, 2005.

Kolesar, K. R., Chen, C., Johnson, D., and Cappa, C. D.: The influences of mass loading and rapid dilution of secondary organic aerosol on particle volatility, Atmospheric Chemistry and Physics, 15, 9327-9343, https://doi.org/10.5194/acp-15-9327-2015, 2015.

Kramer, A. L., Suski, K. J., Bell, D. M., Zelenyuk, A., and Massey Simonich, S. L.: Formation of Polycyclic Aromatic Hydrocarbon Oxidation Products in alpha-Pinene Secondary Organic Aerosol Particles Formed through Ozonolysis, Environ Sci Technol, 53, 6669-6677, https://doi.org/10.1021/acs.est.9b01732, 2019.

Kristensen, K., Jensen, L. N., Quéléver, L. L. J., Christiansen, S., Rosati, B., Elm, J., Teiwes, R., Pedersen, H. B., Glasius, M., Ehn, M., and Bilde, M.: The Aarhus Chamber Campaign on Highly Oxygenated Organic Molecules and Aerosols (ACCHA): particle formation, organic acids, and dimer esters from α-pinene ozonolysis at different temperatures, Atmospheric Chemistry and Physics, 20, 12549-12567, https://doi.org/10.5194/acp-20-12549-2020, 2020.

Kroll, J. H. and Seinfeld, J. H.: Chemistry of secondary organic aerosol: Formation and evolution of low-volatility organics in the atmosphere, Atmospheric Environment, 42, 3593-3624, https://doi.org/10.1016/j.atmosenv.2008.01.003, 2008.

Lambe, A., Massoli, P., Zhang, X., Canagaratna, M., Nowak, J., Daube, C., Yan, C., Nie, W., Onasch, T., Jayne, J., Kolb, C., Davidovits, P., Worsnop, D., and Brune, W.: Controlled nitric oxide production via O(1D)+N2O reactions for use in oxidation flow reactor studies, Atmospheric Measurement Techniques, 10, 2283-2298, https://doi.org/10.5194/amt-10-2283-2017, 2017.

Lambe, A. T., Ahern, A. T., Wright, J. P., Croasdale, D. R., Davidovits, P., and Onasch, T. B.: Oxidative aging and cloud condensation nuclei activation of laboratory combustion soot, Journal of Aerosol Science, 79, 31-39, https://doi.org/10.1016/j.jaerosci.2014.10.001, 2015a.

Lambe, A. T., Krechmer, J. E., Peng, Z., Casar, J. R., Carrasquillo, A. J., Raff, J. D., Jimenez, J. L., and Worsnop, D. R.: HOx and NOx production in oxidation flow reactors via photolysis of isopropyl nitrite, isopropyl nitrite-d7, and 1,3-propyl dinitrite at λ = 254, 350, and 369nm, Atmospheric Measurement Techniques, 12, 299-311, https://doi.org/10.5194/amt-12-299-2019, 2019.

Lambe, A. T., Onasch, T. B., Massoli, P., Croasdale, D. R., Wright, J. P., Ahern, A. T., Williams, L. R., Worsnop, D. R., Brune, W. H., and Davidovits, P.: Laboratory studies of the chemical composition and cloud condensation nuclei (CCN) activity of secondary organic aerosol (SOA) and oxidized primary organic aerosol (OPOA), Atmospheric Chemistry and Physics, 11, 8913-8928, https://doi.org/10.5194/acp-11-8913-2011, 2011a.

Lambe, A. T., Chhabra, P. S., Onasch, T. B., Brune, W. H., Hunter, J. F., Kroll, J. H., Cummings, M. J., Brogan, J. F., Parmar, Y., Worsnop, D. R., Kolb, C. E., and Davidovits, P.: Effect of oxidant concentration, exposure time, and seed particles on

secondary organic aerosol chemical composition and yield, Atmospheric Chemistry and Physics, 15, 3063-3075, https://doi.org/10.5194/acp-15-3063-2015, 2015b.

Lambe, A. T., Ahern, A. T., Williams, L. R., Slowik, J. G., Wong, J. P. S., Abbatt, J. P. D., Brune, W. H., Ng, N. L., Wright, J. P., Croasdale, D. R., Worsnop, D. R., Davidovits, P., and Onasch, T. B.: Characterization of aerosol photooxidation flow reactors: heterogeneous oxidation, secondary organic aerosol formation and cloud condensation nuclei activity measurements, Atmospheric Measurement Techniques, 4, 445-461, https://doi.org/10.5194/amt-4-445-2011, 2011b.

Lamkaddam, H., Gratien, A., Pangui, E., Cazaunau, M., Picquet-Varrault, B., and Doussin, J. F.: High-NOx Photooxidation of n-Dodecane: Temperature Dependence of SOA Formation, Environ Sci Technol, 51, 192-201, https://doi.org/10.1021/acs.est.6b03821, 2017.

Lee, B.-H., Pierce, J. R., Engelhart, G. J., and Pandis, S. N.: Volatility of secondary organic aerosol from the ozonolysis of monoterpenes, Atmospheric Environment, 45, 2443-2452, https://doi.org/10.1016/j.atmosenv.2011.02.004, 2011.

Lei, Z., Olson, N. E., Zhang, Y., Chen, Y., Lambe, A. T., Zhang, J., White, N. J., Atkin, J. M., Banaszak Holl, M. M., Zhang, Z., Gold, A., Surratt, J. D., and Ault, A. P.: Morphology and Viscosity Changes after Reactive Uptake of Isoprene Epoxydiols in Submicrometer Phase Separated Particles with Secondary Organic Aerosol Formed from Different Volatile Organic Compounds, ACS Earth and Space Chemistry, 6, 871-882, https://doi.org/10.1021/acsearthspacechem.1c00156, 2022.

Li, J., Wang, W., Li, K., Zhang, W., Peng, C., Zhou, L., Shi, B., Chen, Y., Liu, M., Li, H., and Ge, M.: Temperature effects on optical properties and chemical composition of secondary organic aerosol derived from n-dodecane, Atmospheric Chemistry and Physics, 20, 8123-8137, https://doi.org/10.5194/acp-20-8123-2020, 2020a.

Li, K., Liggio, J., Lee, P., Han, C., Liu, Q., and Li, S.-M.: Secondary organic aerosol formation from α-pinene, alkanes, and oil-sands-related precursors in a new oxidation flow reactor, Atmospheric Chemistry and Physics, 19, 9715-9731, https://doi.org/10.5194/acp-19-9715-2019, 2019.

Li, Q., Hu, D., Leungsakul, S., and Kamens, R. M.: Large outdoor chamber experiments and computer simulations: (I) Secondary organic aerosol formation from the oxidation of a mixture of d-limonene and α-pinene, Atmospheric Environment, 41, 9341-9352, https://doi.org/10.1016/j.atmosenv.2007.09.017, 2007.

Li, R., Palm, B. B., Ortega, A. M., Hlywiak, J., Hu, W., Peng, Z., Day, D. A., Knote, C., Brune, W. H., de Gouw, J. A., and Jimenez, J. L.: Modeling the radical chemistry in an oxidation flow reactor: radical formation and recycling, sensitivities, and the OH exposure estimation equation, J Phys Chem A, 119, 4418-4432, https://doi.org/10.1021/jp509534k, 2015.

Li, Y., Day, D. A., Stark, H., Jimenez, J. L., and Shiraiwa, M.: Predictions of the glass transition temperature and viscosity of organic aerosols from volatility distributions, Atmospheric Chemistry and Physics, 20, 8103-8122, https://doi.org/10.5194/acp-20-8103-2020, 2020b.

Liao, K., Chen, Q., Liu, Y., Li, Y. J., Lambe, A. T., Zhu, T., Huang, R. J., Zheng, Y., Cheng, X., Miao, R., Huang, G., Khuzestani, R. B., and Jia, T.: Secondary Organic Aerosol Formation of Fleet Vehicle Emissions in China: Potential Seasonality of Spatial Distributions, Environ Sci Technol, 55, 7276-7286, https://doi.org/10.1021/acs.est.0c08591, 2021.

Link, M. F., Friedman, B., Fulgham, R., Brophy, P., Galang, A., Jathar, S. H., Veres, P., Roberts, J. M., and Farmer, D. K.: Photochemical processing of diesel fuel emissions as a large secondary source of isocyanic acid (HNCO), Geophysical Research Letters, 43, 4033-4041, https://doi.org/10.1002/2016gl068207, 2016.

Liu, J., Chu, B., Chen, T., Liu, C., Wang, L., Bao, X., and He, H.: Secondary Organic Aerosol Formation from Ambient Air at an Urban Site in Beijing: Effects of OH Exposure and Precursor Concentrations, Environ Sci Technol, 52, 6834-6841, https://doi.org/10.1021/acs.est.7b05701, 2018.

Liu, T., Zhou, L., Liu, Q., Lee, B. P., Yao, D., Lu, H., Lyu, X., Guo, H., and Chan, C. K.: Secondary Organic Aerosol Formation from Urban Roadside Air in Hong Kong, Environ Sci Technol, 53, 3001-3009, https://doi.org/10.1021/acs.est.8b06587, 2019.

Louvaris, E. E., Karnezi, E., Kostenidou, E., Kaltsonoudis, C., and Pandis, S. N.: Estimation of the volatility distribution of organic aerosol combining thermodenuder and isothermal dilution measurements, Atmospheric Measurement Techniques, 10, 3909-3918, https://doi.org/10.5194/amt-10-3909-2017, 2017.

Mao, J., Ren, X., Brune, W. H., Olson, J. R., Crawford, J. H., Fried, A., Huey, L. G., Cohen, R. C., Heikes, B., Singh, H. B., Blake, D. R., Sachse, G. W., Diskin, G. S., Hall, S. R., and Shetter, R. E.: Airborne measurement of OH reactivity during INTEX-B, Atmospheric Chemistry and Physics, 9, 163-173, https://doi.org/10.5194/acp-9-163-2009, 2009.

Martin-Reviejo, M. and Wirtz, K.: Is benzene a precursor for secondary organic aerosol?, Environ Sci Technol, 39, 1045-1054, https://doi.org/10.1021/es049802a, 2005.

McFiggans, G., Mentel, T. F., Wildt, J., Pullinen, I., Kang, S., Kleist, E., Schmitt, S., Springer, M., Tillmann, R., Wu, C., Zhao, D., Hallquist, M., Faxon, C., Le Breton, M., Hallquist, A. M., Simpson, D., Bergstrom, R., Jenkin, M. E., Ehn, M., Thornton, J. A., Alfarra, M. R., Bannan, T. J., Percival, C. J., Priestley, M., Topping, D., and Kiendler-Scharr, A.: Secondary organic aerosol reduced by mixture of atmospheric vapours, Nature, 565, 587-593, https://doi.org/10.1038/s41586-018-0871-y, 2019.

Mitroo, D., Sun, Y., Combest, D. P., Kumar, P., and Williams, B. J.: Assessing the degree of plug flow in oxidation flow reactors (OFRs): a study on a potential aerosol mass (PAM) reactor, Atmospheric Measurement Techniques, 11, 1741-1756, https://doi.org/10.5194/amt-11-1741-2018, 2018.

1080 Murschell, T. and Farmer, D. K.: Atmospheric OH Oxidation of Three Chlorinated Aromatic Herbicides, Environ Sci Technol, 52, 4583-4591, https://doi.org/10.1021/acs.est.7b06025, 2018.

Myhre, G., Shindell, D., Bréon, F.-M., Collins, W., Fuglestvedt, J., Huang, J., Koch, D., Lamarque, J.-F., Lee, D., Mendoza, B., Nakajima, T., Robock, A., Stephens, G., Takemura, T., and Zhang, H.: Anthropogenic and Natural Radiative Forcing, in: Climate Change 2013: The Physical Science Basis. Contribution of Working Group I to the Fifth Assessment Report of
1085 the Intergovernmental Panel on Climate Change, edited by: Stocker, T. F., Qin, D., Plattner, G.-K., Tignor, M., Allen, S. K., Boschung, J., Nauels, A., Xia, Y., Bex, V., and Midgley, P. M., p. 659, Cambridge University Press, Cambridge, United Kingdom and New York, NY, USA, United Kingdom and New York, NY, USA, available at: https://www.ipcc.ch/report/ar5/wg1/ (last access: 6 December 2017), 2013.

Nault, B. A., Campuzano-Jost, P., Day, D. A., Schroder, J. C., Anderson, B., Beyersdorf, A. J., Blake, D. R., Brune, W. H.,
1090 Choi, Y., Corr, C. A., de Gouw, J. A., Dibb, J., DiGangi, J. P., Diskin, G. S., Fried, A., Huey, L. G., Kim, M. J., Knote, C. J., Lamb, K. D., Lee, T., Park, T., Pusede, S. E., Scheuer, E., Thornhill, K. L., Woo, J.-H., and Jimenez, J. L.: Secondary organic aerosol production from local emissions dominates the organic aerosol budget over Seoul, South Korea, during KORUS-AQ, Atmospheric Chemistry and Physics, 18, 17769-17800, https://doi.org/10.5194/acp-18-17769-2018, 2018.

Nault, B. A., Jo, D. S., McDonald, B. C., Campuzano-Jost, P., Day, D. A., Hu, W., Schroder, J. C., Allan, J., Blake, D. R.,
1095 Canagaratna, M. R., Coe, H., Coggon, M. M., DeCarlo, P. F., Diskin, G. S., Dunmore, R., Flocke, F., Fried, A., Gilman, J. B., Gkatzelis, G., Hamilton, J. F., Hanisco, T. F., Hayes, P. L., Henze, D. K., Hodzic, A., Hopkins, J., Hu, M., Huey, L. G., Jobson, B. T., Kuster, W. C., Lewis, A., Li, M., Liao, J., Nawaz, M. O., Pollack, I. B., Peischl, J., Rappenglück, B., Reeves, C. E., Richter, D., Roberts, J. M., Ryerson, T. B., Shao, M., Sommers, J. M., Walega, J., Warneke, C., Weibring, P., Wolfe, G. M., Young, D. E., Yuan, B., Zhang, Q., de Gouw, J. A., and Jimenez, J. L.: Secondary organic aerosols from
1100 anthropogenic volatile organic compounds contribute substantially to air pollution mortality, Atmospheric Chemistry and Physics, 21, 11201-11224, https://doi.org/10.5194/acp-21-11201-2021, 2021.

Nel, A.: Atmosphere. Air pollution-related illness: effects of particles, Science, 308, 804-806, https://doi.org/10.1126/science.1108752, 2005.

Ni, J., Yu, G., Guo, Q., Liang, Q., and Zhou, Z.: Experimental and Numerical Study of the Flow Field and Temperature Field
1105 for a Large-Scale Radiant Syngas Cooler, Industrial & Engineering Chemistry Research, 49, 4452-4461, https://doi.org/10.1021/ie100014r, 2010.

Ortega, A. M., Day, D. A., Cubison, M. J., Brune, W. H., Bon, D., de Gouw, J. A., and Jimenez, J. L.: Secondary organic aerosol formation and primary organic aerosol oxidation from biomass-burning smoke in a flow reactor during FLAME-3, Atmospheric Chemistry and Physics, 13, 11551-11571, https://doi.org/10.5194/acp-13-11551-2013, 2013.
1110 Ortega, A. M., Hayes, P. L., Peng, Z., Palm, B. B., Hu, W., Day, D. A., Li, R., Cubison, M. J., Brune, W. H., Graus, M., Warneke, C., Gilman, J. B., Kuster, W. C., de Gouw, J., Gutiérrez-Montes, C., and Jimenez, J. L.: Real-time measurements of secondary organic aerosol formation and aging from ambient air in an oxidation flow reactor in the Los Angeles area, Atmospheric Chemistry and Physics, 16, 7411-7433, https://doi.org/10.5194/acp-16-7411-2016, 2016.

Paciga, A., Karnezi, E., Kostenidou, E., Hildebrandt, L., Psichoudaki, M., Engelhart, G. J., Lee, B. H., Crippa, M., Prévôt, A.
1115 S. H., Baltensperger, U., and Pandis, S. N.: Volatility of organic aerosol and its components in the megacity of Paris, Atmos. Chem. Phys., 16, 2013-2023, https://doi.org/10.5194/acp-16-2013-2016, 2016.

Palm, B. B., Campuzano-Jost, P., Ortega, A. M., Day, D. A., Kaser, L., Jud, W., Karl, T., Hansel, A., Hunter, J. F., Cross, E. S., Kroll, J. H., Peng, Z., Brune, W. H., and Jimenez, J. L.: In situ secondary organic aerosol formation from ambient pine forest air using an oxidation flow reactor, Atmospheric Chemistry and Physics, 16, 2943-2970, https://doi.org/10.5194/acp-
1120 16-2943-2016, 2016.

Palm, B. B., Campuzano-Jost, P., Day, D. A., Ortega, A. M., Fry, J. L., Brown, S. S., Zarzana, K. J., Dube, W., Wagner, N. L., Draper, D. C., Kaser, L., Jud, W., Karl, T., Hansel, A., Gutiérrez-Montes, C., and Jimenez, J. L.: Secondary organic aerosol formation from in situ OH, O3, and NO3 oxidation of ambient forest air in an oxidation flow reactor, Atmospheric Chemistry and Physics, 17, 5331-5354, https://doi.org/10.5194/acp-17-5331-2017, 2017.
1125 Palm, B. B., de Sá, S. S., Day, D. A., Campuzano-Jost, P., Hu, W., Seco, R., Sjostedt, S. J., Park, J.-H., Guenther, A. B., Kim, S., Brito, J., Wurm, F., Artaxo, P., Thalman, R., Wang, J., Yee, L. D., Wernis, R., Isaacman-VanWertz, G., Goldstein, A. H., Liu, Y., Springston, S. R., Souza, R., Newburn, M. K., Alexander, M. L., Martin, S. T., and Jimenez, J. L.: Secondary organic aerosol formation from ambient air in an oxidation flow reactor in central Amazonia, Atmospheric Chemistry and Physics, 18, 467-493, https://doi.org/10.5194/acp-18-467-2018, 2018.
1130 Pankow, J. F.: An absorption model of gas/particle partitioning of organic compounds in the atmosphere, Atmospheric Environment, 28, 185-188, https://doi.org/10.1016/1352-2310(94)90093-0, 1994.

Park, G., Kim, K., Kang, S., Park, T., Ban, J., and Lee, T.: The Chemical Characteristics and Formation of Potential Secondary Aerosol (PSA) using an Oxidation Flow Reactor (OFR) in the Summer: Focus on the Residential Area, Suwon, Journal of Korean Society for Atmospheric Environment, 35, 786-801, https://doi.org/10.5572/kosae.2019.35.6.786, 2019.
1135 Park, Y. and Kim, H.: Real time measurements of the secondary organic aerosol formation and aging from ambient air using an oxidation flow reactor in seoul during winter, Environ Pollut, 327, 121464, https://doi.org/10.1016/j.envpol.2023.121464, 2023.

Patankar, S. V. and Spalding, D. B.: A calculation procedure for heat, mass and momentum transfer in three-dimensional parabolic flows, International Journal of Heat and Mass Transfer, 15, 1787-1806, https://doi.org/10.1016/0017-9310(72)90054-3, 1972.

Pathak, R. K., Stanier, C. O., Donahue, N. M., and Pandis, S. N.: Ozonolysis of α-pinene at atmospherically relevant concentrations: Temperature dependence of aerosol mass fractions (yields), Journal of Geophysical Research, 112, D03201, https://doi.org/10.1029/2006jd007436, 2007.

Paulsen, D., Dommen, J., Kalberer, M., Prevot, A. S., Richter, R., Sax, M., Steinbacher, M., Weingartner, E., and Baltensperger, U.: Secondary organic aerosol formation by irradiation of 1,3,5-trimethylbenzene-NOx-H2O in a new reaction chamber for atmospheric chemistry and physics, Environ Sci Technol, 39, 2668-2678, https://doi.org/10.1021/es0489137, 2005.

Peng, Z. and Jimenez, J. L.: Radical chemistry in oxidation flow reactors for atmospheric chemistry research, Chem Soc Rev, 49, 2570-2616, https://doi.org/10.1039/c9cs00766k, 2020.

Peng, Z., Lee-Taylor, J., Orlando, J. J., Tyndall, G. S., and Jimenez, J. L.: Organic peroxy radical chemistry in oxidation flow reactors and environmental chambers and their atmospheric relevance, Atmospheric Chemistry and Physics, 19, 813-834, https://doi.org/10.5194/acp-19-813-2019, 2019.

Peng, Z., Day, D. A., Stark, H., Li, R., Lee-Taylor, J., Palm, B. B., Brune, W. H., and Jimenez, J. L.: HOx radical chemistry in oxidation flow reactors with low-pressure mercury lamps systematically examined by modeling, Atmospheric Measurement Techniques, 8, 4863-4890, https://doi.org/10.5194/amt-8-4863-2015, 2015.

Peng, Z., Palm, B. B., Day, D. A., Talukdar, R. K., Hu, W., Lambe, A. T., Brune, W. H., and Jimenez, J. L.: Model Evaluation of New Techniques for Maintaining High-NO Conditions in Oxidation Flow Reactors for the Study of OH-Initiated Atmospheric Chemistry, ACS Earth and Space Chemistry, 2, 72-86, https://doi.org/10.1021/acsearthspacechem.7b00070, 2018.

Pierce, J. R., Chen, K., and Adams, P. J.: Contribution of primary carbonaceous aerosol to cloud condensation nuclei: processes and uncertainties evaluated with a global aerosol microphysics model, Atmospheric Chemistry and Physics, 7, 5447-5466, https://doi.org/10.5194/acp-7-5447-2007, 2007.

Poschl, U.: Atmospheric aerosols: composition, transformation, climate and health effects, Angew Chem Int Ed Engl, 44, 7520-7540, https://doi.org/10.1002/anie.200501122, 2005.

Presto, A. A., Hartz, K. E., and Donahue, N. M.: Secondary organic aerosol production from terpene ozonolysis. 2. Effect of NOx concentration, Environ Sci Technol, 39, 7046-7054, https://doi.org/10.1021/es050400s, 2005.

Price, D. J., Kacarab, M., Cocker, D. R., Purvis-Roberts, K. L., and Silva, P. J.: Effects of temperature on the formation of secondary organic aerosol from amine precursors, Aerosol Science and Technology, 50, 1216-1226, https://doi.org/10.1080/02786826.2016.1236182, 2016.

Qi, L., Nakao, S., Tang, P., and Cocker, D. R.: Temperature effect on physical and chemical properties of secondary organic aerosol from m-xylene photooxidation, Atmospheric Chemistry and Physics, 10, 3847-3854, https://doi.org/10.5194/acp-10-3847-2010, 2010.

Quéléver, L. L. J., Kristensen, K., Normann Jensen, L., Rosati, B., Teiwes, R., Daellenbach, K. R., Peräkylä, O., Roldin, P., Bossi, R., Pedersen, H. B., Glasius, M., Bilde, M., and Ehn, M.: Effect of temperature on the formation of highly oxygenated organic molecules (HOMs) from alpha-pinene ozonolysis, Atmospheric Chemistry and Physics, 19, 7609-7625, https://doi.org/10.5194/acp-19-7609-2019, 2019.

Riipinen, I., Pierce, J. R., Donahue, N. M., and Pandis, S. N.: Equilibration time scales of organic aerosol inside thermodenuders: Evaporation kinetics versus thermodynamics, Atmospheric Environment, 44, 597-607, https://doi.org/10.1016/j.atmosenv.2009.11.022, 2010.

Robbins, R. C. and Cadle, R. D.: Kinetics of the Reaction between Gaseous Ammonia and Sulfuric Acid Droplets in an Aerosol, The Journal of Physical Chemistry, 62, 469-471, https://doi.org/10.1021/j150562a025, 2002.

Roldin, P., Eriksson, A. C., Nordin, E. Z., Hermansson, E., Mogensen, D., Rusanen, A., Boy, M., Swietlicki, E., Svenningsson, B., Zelenyuk, A., and Pagels, J.: Modelling non-equilibrium secondary organic aerosol formation and evaporation with the aerosol dynamics, gas- and particle-phase chemistry kinetic multilayer model ADCHAM, Atmospheric Chemistry and Physics, 14, 7953-7993, https://doi.org/10.5194/acp-14-7953-2014, 2014.

Rollins, A. W., Kiendler-Scharr, A., Fry, J. L., Brauers, T., Brown, S. S., Dorn, H. P., Dubé, W. P., Fuchs, H., Mensah, A., Mentel, T. F., Rohrer, F., Tillmann, R., Wegener, R., Wooldridge, P. J., and Cohen, R. C.: Isoprene oxidation by nitrate radical: alkyl nitrate and secondary organic aerosol yields, Atmospheric Chemistry and Physics, 9, 6685-6703, https://doi.org/10.5194/acp-9-6685-2009, 2009.

Rowe, J. P., Lambe, A. T., and Brune, W. H.: Technical Note: Effect of varying the λ = 185 and 254 nm photon flux ratio on radical generation in oxidation flow reactors, ACP, https://doi.org/10.5194/acp-2020-642, 2020.

Saha, P. K. and Grieshop, A. P.: Exploring Divergent Volatility Properties from Yield and Thermodenuder Measurements of Secondary Organic Aerosol from alpha-Pinene Ozonolysis, Environ Sci Technol, 50, 5740-5749, https://doi.org/10.1021/acs.est.6b00303, 2016.

Saha, P. K., Reece, S. M., and Grieshop, A. P.: Seasonally Varying Secondary Organic Aerosol Formation From In-Situ Oxidation of Near-Highway Air, Environ Sci Technol, 52, 7192-7202, https://doi.org/10.1021/acs.est.8b01134, 2018.

Saha, P. K., Khlystov, A., Yahya, K., Zhang, Y., Xu, L., Ng, N. L., and Grieshop, A. P.: Quantifying the volatility of organic aerosol in the southeastern US, Atmospheric Chemistry and Physics, 17, 501-520, https://doi.org/10.5194/acp-17-501-2017, 2017.

1200 Sbai, S. E., Li, C., Boreave, A., Charbonnel, N., Perrier, S., Vernoux, P., Bentayeb, F., George, C., and Gil, S.: Atmospheric photochemistry and secondary aerosol formation of urban air in Lyon, France, J Environ Sci (China), 99, 311-323, https://doi.org/10.1016/j.jes.2020.06.037, 2021.

Schobesberger, S., D'Ambro, E. L., Lopez-Hilfiker, F. D., Mohr, C., and Thornton, J. A.: A model framework to retrieve thermodynamic and kinetic properties of organic aerosol from composition-resolved thermal desorption measurements,
1205 Atmospheric Chemistry and Physics, 18, 14757-14785, https://doi.org/10.5194/acp-18-14757-2018, 2018.

Sengupta, D., Samburova, V., Bhattarai, C., Kirillova, E., Mazzoleni, L., Iaukea-Lum, M., Watts, A., Moosmüller, H., and Khlystov, A.: Light absorption by polar and non-polar aerosol compounds from laboratory biomass combustion, Atmospheric Chemistry and Physics, 18, 10849-10867, https://doi.org/10.5194/acp-18-10849-2018, 2018.

Shah, R. U., Coggon, M. M., Gkatzelis, G. I., McDonald, B. C., Tasoglou, A., Huber, H., Gilman, J., Warneke, C., Robinson,
1210 A. L., and Presto, A. A.: Urban Oxidation Flow Reactor Measurements Reveal Significant Secondary Organic Aerosol Contributions from Volatile Emissions of Emerging Importance, Environ Sci Technol, 54, 714-725, https://doi.org/10.1021/acs.est.9b06531, 2020.

Shih, T.-H., Liou, W. W., Shabbir, A., Yang, Z., and Zhu, J.: A new k-ϵ eddy viscosity model for high reynolds number turbulent flows, Computers & Fluids, 24, 227-238, https://doi.org/10.1016/0045-7930(94)00032-t, 1995.

1215 Siemens, K., Morales, A., He, Q., Li, C., Hettiyadura, A. P. S., Rudich, Y., and Laskin, A.: Molecular Analysis of Secondary Brown Carbon Produced from the Photooxidation of Naphthalene, Environ Sci Technol, 56, 3340-3353, https://doi.org/10.1021/acs.est.1c03135, 2022.

Simon, M., Dada, L., Heinritzi, M., Scholz, W., Stolzenburg, D., Fischer, L., Wagner, A. C., Kürten, A., Rörup, B., He, X.-C., Almeida, J., Baalbaki, R., Baccarini, A., Bauer, P. S., Beck, L., Bergen, A., Bianchi, F., Bräkling, S., Brilke, S., Caudillo,
1220 L., Chen, D., Chu, B., Dias, A., Draper, D. C., Duplissy, J., El-Haddad, I., Finkenzeller, H., Frege, C., Gonzalez-Carracedo, L., Gordon, H., Granzin, M., Hakala, J., Hofbauer, V., Hoyle, C. R., Kim, C., Kong, W., Lamkaddam, H., Lee, C. P., Lehtipalo, K., Leiminger, M., Mai, H., Manninen, H. E., Marie, G., Marten, R., Mentler, B., Molteni, U., Nichman, L., Nie, W., Ojdanic, A., Onnela, A., Partoll, E., Petäjä, T., Pfeifer, J., Philippov, M., Quéléver, L. L. J., Ranjithkumar, A., Rissanen, M. P., Schallhart, S., Schobesberger, S., Schuchmann, S., Shen, J., Sipilä, M., Steiner, G., Stozhkov, Y., Tauber, C., Tham,
1225 Y. J., Tomé, A. R., Vazquez-Pufleau, M., Vogel, A. L., Wagner, R., Wang, M., Wang, D. S., Wang, Y., Weber, S. K., Wu, Y., Xiao, M., Yan, C., Ye, P., Ye, Q., Zauner-Wieczorek, M., Zhou, X., Baltensperger, U., Dommen, J., Flagan, R. C., Hansel, A., Kulmala, M., Volkamer, R., Winkler, P. M., Worsnop, D. R., Donahue, N. M., Kirkby, J., and Curtius, J.: Molecular understanding of new-particle formation from α-pinene between −50 and +25 ∘C, Atmospheric Chemistry and Physics, 20, 9183-9207, https://doi.org/10.5194/acp-20-9183-2020, 2020.

1230 Simonen, P., Saukko, E., Karjalainen, P., Timonen, H., Bloss, M., Aakko-Saksa, P., Rönkkö, T., Keskinen, J., and Dal Maso, M.: A new oxidation flow reactor for measuring secondary aerosol formation of rapidly changing emission sources, Atmospheric Measurement Techniques, 10, 1519-1537, https://doi.org/10.5194/amt-10-1519-2017, 2017.

Srivastava, D., Li, W., Tong, S., Shi, Z., and Harrison, R. M.: Characterization of products formed from the oxidation of toluene and m-xylene with varying NO(x) and OH exposure, Chemosphere, 334, 139002,
1235 https://doi.org/10.1016/j.chemosphere.2023.139002, 2023.

Srivastava, D., Vu, T. V., Tong, S., Shi, Z., and Harrison, R. M.: Formation of secondary organic aerosols from anthropogenic precursors in laboratory studies, npj Climate and Atmospheric Science, 5, 22, https://doi.org/10.1038/s41612-022-00238-6, 2022.

Stanier, C. O., Donahue, N., and Pandis, S. N.: Parameterization of secondary organic aerosol mass fractions from smog
1240 chamber data, Atmospheric Environment, 42, 2276-2299, https://doi.org/10.1016/j.atmosenv.2007.12.042, 2008.

Sumlin, B., Fortner, E., Lambe, A., Shetty, N. J., Daube, C., Liu, P., Majluf, F., Herndon, S., and Chakrabarty, R. K.: Diel cycle impacts on the chemical and light absorption properties of organic carbon aerosol from wildfires in the western United States, Atmospheric Chemistry and Physics, 21, 11843-11856, https://doi.org/10.5194/acp-21-11843-2021, 2021.

Takekawa, H., Minoura, H., and Yamazaki, S.: Temperature dependence of secondary organic aerosol formation by photo-
1245 oxidation of hydrocarbons, Atmospheric Environment, 37, 3413-3424, https://doi.org/10.1016/s1352-2310(03)00359-5, 2003.

Tillmann, R., Hallquist, M., Jonsson, Å. M., Kiendler-Scharr, A., Saathoff, H., Iinuma, Y., and Mentel, T. F.: Influence of relative humidity and temperature on the production of pinonaldehyde and OH radicals from the ozonolysis of α-pinene, Atmospheric Chemistry and Physics, 10, 7057-7072, https://doi.org/10.5194/acp-10-7057-2010, 2010.

1250 Tkacik, D. S., Lambe, A. T., Jathar, S., Li, X., Presto, A. A., Zhao, Y., Blake, D., Meinardi, S., Jayne, J. T., Croteau, P. L., and Robinson, A. L.: Secondary organic aerosol formation from in-use motor vehicle emissions using a potential aerosol mass reactor, Environ Sci Technol, 48, 11235-11242, https://doi.org/10.1021/es502239v, 2014.

Wang, X., Liu, T., Bernard, F., Ding, X., Wen, S., Zhang, Y., Zhang, Z., He, Q., Lü, S., Chen, J., Saunders, S., and Yu, J.: Design and characterization of a smog chamber for studying gas-phase chemical mechanisms and aerosol formation,
1255 Atmospheric Measurement Techniques, 7, 301-313, https://doi.org/10.5194/amt-7-301-2014, 2014.

Warren, B., Austin, R. L., and Cocker, D. R.: Temperature dependence of secondary organic aerosol, Atmospheric Environment, 43, 3548-3555, https://doi.org/10.1016/j.atmosenv.2009.04.011, 2009.

Watne, A. K., Psichoudaki, M., Ljungstrom, E., Le Breton, M., Hallquist, M., Jerksjo, M., Fallgren, H., Jutterstrom, S., and Hallquist, A. M.: Fresh and Oxidized Emissions from In-Use Transit Buses Running on Diesel, Biodiesel, and CNG, Environ Sci Technol, 52, 7720-7728, https://doi.org/10.1021/acs.est.8b01394, 2018.

White, S., Angove, D., Li, K., Campbell, I., Element, A., Halliburton, B., Lavrencic, S., Cameron, D., Jamie, I., and Azzi, M.: Development of a new smog chamber for studying the impact of different UV lamps on SAPRC chemical mechanism predictions and aerosol formation, Environmental Chemistry, 15, https://doi.org/10.1071/en18005, 2018.

Xu, N. and Collins, D. R.: Design and characterization of a new oxidation flow reactor for laboratory and long-term ambient studies, Atmospheric Measurement Techniques, 14, 2891-2906, https://doi.org/10.5194/amt-14-2891-2021, 2021.

Xu, W., Li, Z., Lambe, A. T., Li, J., Liu, T., Du, A., Zhang, Z., Zhou, W., and Sun, Y.: Secondary organic aerosol formation and aging from ambient air in an oxidation flow reactor during wintertime in Beijing, China, Environ Res, 209, 112751, https://doi.org/10.1016/j.envres.2022.112751, 2022.

Xu, W., Takeuchi, M., Chen, C., Qiu, Y., Xie, C., Xu, W., Ma, N., Worsnop, D. R., Ng, N. L., and Sun, Y.: Estimation of particulate organic nitrates from thermodenuder-aerosol mass spectrometer measurements in North China Plain, Atmospheric Measurement Techniques Discussions, https://doi.org/10.5194/amt-2020-474, 2020.

Zhang, Q., Xu, Y., and Jia, L.: Secondary organic aerosol formation from OH-initiated oxidation of m-xylene: effects of relative humidity on yield and chemical composition, acp, 10.5194/acp-2019-20, 2019.

Zhang, X., McVay, R. C., Huang, D. D., Dalleska, N. F., Aumont, B., Flagan, R. C., and Seinfeld, J. H.: Formation and evolution of molecular products in alpha-pinene secondary organic aerosol, Proc Natl Acad Sci U S A, 112, 14168-14173, https://doi.org/10.1073/pnas.1517742112, 2015.

Zhao, R., Zhang, Q., Xu, X., Zhao, W., Yu, H., Wang, W., Zhang, Y., and Zhang, W.: Effect of experimental conditions on secondary organic aerosol formation in an oxidation flow reactor, Atmospheric Pollution Research, 12, 205-213, https://doi.org/10.1016/j.apr.2021.01.011, 2021.

Ziemann, P. J. and Atkinson, R.: Kinetics, products, and mechanisms of secondary organic aerosol formation, Chem Soc Rev, 41, 6582-6605, https://doi.org/10.1039/c2cs35122f, 2012.

Zong, T., Wu, Z., Wang, J., Bi, K., Fang, W., Yang, Y., Yu, X., Bao, Z., Meng, X., Zhang, Y., Guo, S., Chen, Y., Liu, C., Zhang, Y., Li, S. M., and Hu, M.: A new smog chamber system for atmospheric multiphase chemistry study: design and characterization, Atmos. Meas. Tech. Discuss., 2023, 1-25, https://doi.org/10.5194/amt-2023-34, 2023.

Supplementary material for:

A comprehensive evaluation of enhanced temperature influence on gas and aerosol chemistry in the lamp-enclosed oxidation flow reactor (OFR) system

5   Tianle Pan[1,2,3,4,5], Andrew T. Lambe[6], Weiwei Hu[1,2,4,5], Yicong He[7,a], Minghao Hu[8], Huaishan Zhou[1,2,3,4,5], Xinming Wang[1,2,4,5], Qingqing Hu[9], Hui Chen[9], Yue Zhao[10], Yuanlong Huang[11], Doug R. Worsnop[6,12], Zhe Peng[13,14], Melissa A. Morris[13,14], Douglas A. Day[13,14], Pedro Campuzano-Jost[13,14], Jose-Luis Jimenez[13,14], Shantanu H. Jathar[7]

[1]State Key Laboratory of Organic Geochemistry, Guangzhou Institute of Geochemistry, Chinese Academy of Sciences, Guangzhou 510640, China
10   [2]CAS Center for Excellence in Deep Earth Science, Guangzhou, 510640, China
[3]Chinese Academy of Sciences University, Beijing 100049, China
[4]Guangdong-Hong Kong-Macao, Joint Laboratory for Environmental Pollution and Control, Guangzhou Institute of Geochemistry, Chinese Academy of Science, Guangzhou 510640, China
15   [5]Guangdong Provincial Key Laboratory of Environmental Protection and Resources Utilization, Chinese Academy of Science, Guangzhou 510640, China
[6]Aerodyne Research Inc., Billerica, Massachusetts, 01821, United States
[7]Department of Mechanical Engineering, Colorado State University, Fort Collins, Colorado 80523, United States
[8]China-UK Low Carbon College, Shanghai Jiao Tong University, Shanghai, 201306, China
20   [9]Key Laboratory of Organic Compound Pollution Control Engineering, School of Environmental and Chemical Engineering, Shanghai University, 200444, Shanghai, China
[10]School of Environmental Science and Engineering, Shanghai Jiao Tong University, Shanghai, 200240, China
[11]Department of Environmental Science and Engineering, California Institute of Technology, Pasadena, California 91125, United States
25   [12]Institute for Atmospheric and Earth System Research (INAR) / Physics, Faculty of Science, University of Helsinki, Helsinki, 00014, Finland
[13]Cooperative Institute for Research in the Environmental Sciences (CIRES), University of Colorado at Boulder, Boulder, Colorado, 80309, United States
[14]Department of Chemistry, University of Colorado at Boulder, Boulder, Colorado 80309, United States
30   [a]now at: State Key Joint Laboratory of Environmental Simulation and Pollution Control, School of Environment, Tsinghua University, Beijing 100084, China

Correspondence to: Weiwei Hu (weiweihu@gig.ac.cn)

1

S1 Supply power for Light Source and BHK lamps

For the UV lamps from Light Source Inc., the supply power (8.9 W) was calculated as 185 mA/425 mA$\times$21 W, where 185 mA is the measured current controlled by the ballast at 10 VAC (full) output; 425 mA and 21 W are the manufacturer specified current and power. For BHK lamps, the supply power (6.3 W) was measured directly with a Kill-A-Watt sensor on the outlet of the lamp controller box at full AC output.

40

S2 Calculation of the heating energy in OFR

For the temperature measured for a lamp control voltage of 10 V (full AC power) and flow rate of 5 L min^{-1} (Fig. 4), we calculated the fraction of heating energy transferred from the UV lamps to the gas inside the OFR (f_g), the N_2 purge gas (f_{N_2}), and the OFR tube wall (f_s). Results were estimated on the assumption that all the electrical input power of the lamps was finally converted into heat, which led to the rise in temperature. We did not consider the heat exchange between the gas inside the OFR, N_2 purge gas, and OFR surface. The energy of gas inside the OFR（or N_2 inside the lamp sleeves）would be lost due to the gas (or N_2) entering and leaving the OFR (or lamps sleeve), depending on the flow rate and the temperature of the ambient gas (or N_2,0.2 and 20 L min^{-1}). Also, the OFR surface dissipate heat to the ambient air. Based on the timeseries of measured temperature in Fig. 4, the f_g, f_s, and f_{N_2} could be calculated as follows:

$$f_g = \frac{Q_g}{Q_{Total}} = \frac{C_g \times M_g \times \Delta T_{i-(i-1)} + C_g \times m_g \times \Delta T_{i-a}}{Q_{Total}} \quad (1)$$

$$f_s = \frac{Q_s}{Q_{Total}} = \frac{C_s \times M_s \times \Delta T_{j-(j-1)} + F \times A \times \Delta T_{j-a}}{Q_{Total}} \quad (2)$$

$$f_{N_2} = \frac{Q_{N_2}}{Q_{Total}} = \frac{C_{N_2} \times M_{N_2} \times \Delta T_{k-(k-1)} + C_{N_2} \times m_{N_2} \times \Delta T_{k-a}}{Q_{Total}} \quad (3)$$

Where Q_g, Q_s, and Q_{N_2} were the energy in 1 second of lamps allocated to the gas inside OFR, surface of OFR and N_2 purge gas, respectively; Q_{Total} is the total energy from 4 lamps in 1 s (35.6 J, 8.9 W for each lamp at full VAC). C_g, C_s and C_{N_2} were the specific heat capacity of gas (1.005 kJ kg^{-1} K^{-1} at 300 K), OFR surface (aluminium, 0.879 kJ kg^{-1} K^{-1} at 293 K) and N_2 (1.038 kJ kg^{-1} K^{-1} at 298 K); M_g, M_s and M_{N_2} were the mass of gas inside OFR, OFR surface, and N_2 in lamp sleeves; $\Delta T_{i-(i-1)}$ was the temperature difference between ith and (i-1)th second for gas inside OFR. $\Delta T_{j-(j-1)}$ and $\Delta T_{k-(k-1)}$ were similar, for the temperature of OFR surface and N_2 purge gas; m_g was the mass of gas entered or left OFR in one second; ΔT_{i-a} was the temperature difference between the gas left OFR at ith second and ambient air; F was the Heat dissipation area for OFR surface; A was the heat transfer coefficient (3.48 J m^{-2} s^{-1} K^{-1}) and ΔT_{j-a} was the temperature difference between the OFR surface at jth

second and ambient air; m_{N_2} was the mass entered or left lamps sleeve in one second; ΔT_{k-a} was the temperature difference between the N_2 left lamps sleeve at k^{th} second and ambient air. Results were shown in Fig. S8.

S3 Calculation of the Richardson number

65   The Richardson number, a dimensionless number that represents the ratio of buoyancy term to flow shear term, can be calculated as follow (Holman, 2010; Huang et al., 2017):

$$R_i = \frac{g\beta D^3 \Delta T/\nu^2}{(\rho U_{avg} D/\mu)^2} \sim \frac{gD}{T U_{avg}^2}\Delta T \qquad (4)$$

where g is the gravitational acceleration (9.78 m s^{-2}), β is the thermal expansion coefficient of air (T^{-1} for ideal gases), D is the diameter of the flow tube (202 mm), T is the temperature at centerline (39 °C), ΔT is the temperature difference between the 70   centerline and tube wall (4 °C), ν is the kinematic viscosity of air (m^2 s^{-1}), ρ is the density of air (kg m^{-3}), U_{avg} is the average velocity on the cross-section of the flow tube (m s^{-1}), calculated based on the flow rate (5 L min^{-1}) and D, μ is the dynamic viscosity (N s m^{-2}). When Ri<0.1, the natural convection is negligible; when Ri>10, the forced convection is negligible, and the buoyancy forces may lead to flow bifurcation and recirculation (Huang et al., 2017).

75   **Table S1: Temperature sensors used in temperature measurement.**

Temperature sensors	Model	Manufacturer
OFR RH/T sensor	Sensirion SHT21	Sensirion AG
Vaisala	HMT130	Vaisala Inc.
Thermocouple	TM-902C, type K	Shenzhen APUHUA Electronic Technology CO. LTD
CEM	DT-83	Shenzhen EVERBEST machinery industry, CO, LTD.

Table S2: Detailed parameters of OFR temperature experiments.

Exp.	Flow rate (L min⁻¹)	Control Voltage (V)	Lamps[1] (num. of lamps×lamp type)	Mesh screen[2]	OFR sensor Position[3]	Position of Probe within OFR[4]	Temp. of surface	Temp. of exhaust
1	5	5	4 × 185 covered	Back	In backplate	Vertical and horizontal at different depth	/[5]	/
2	5	10/6/5/4/2	4 × 185 covered	Back	In backplate	Different depth from the inlet in the center	/	/
3	3/5/7	5	4 × 185 covered	Back	In backplate	Different depth from the inlet in the center	/	/
4	5	10	4 × 185 covered	Back	In backplate	300 mm from the inlet in the center	Measured	/
5	5	10-6-5-4-2-0[6]	4 ×185 covered	Back	In backplate	300 mm from the inlet in the center	Measured	Measured
6	5	10-6-5-4-2-0	2 ×185 covered	Back	In backplate	300 mm from the inlet in the center	Measured	/
7	5	10-6-5-4-2-0	2 ×185 covered	/	300 mm from inlet	300 mm from the inlet in the center	Measured	Measured
8	5	10-6-5-4-2-0	4 × 185	Back	In backplate	300 mm from the inlet in the center	/	/
9	5	10-6-5-4-2-0	2 × 254	Back	In backplate	300 mm from the inlet in the center	/	/
10	5	10-6-5-4-2-0	4 ×185 covered	Front	300 mm from inlet	/	Measured	Measured
11	5	10-6-5-4-2-0	2 ×185 covered	Front	300 mm from inlet	/	Measured	Measured
12	5	10-2-6-3-5-0	4 ×185 covered	Back	In backplate	300 mm from the inlet in the center	/	/

[1] Three types of lamps were used (Figure S2). '185 covered' transmits both 185 and 254 nm radiation, with 80% surface covered with heat-shrink tubes. Lamps of '185' are the same type as '185 covered', but without covering. The lamp of '254' transmits only 254 nm radiation and is not covered.

[2] Two mesh screens are set inside OFR, one near the inlet (Front) and one near the outlet (Back).

[3] The OFR sensor is set in the backplate by default, as shown in Fig. S1.

[4] Extending the external temperature sensor into OFR from the inlet (so the 'Front' mesh screen must be removed). 4 depths were measured for Exp.1-3 (100, 200, 300, and 400 mm from the inlet, respectively)

[5] '/' means no installation or no measurement.

[6] Each voltage was set to last for 16 min.

Table S3: SOM parameters used in this study.

precursor	VOC surrogate	NOx	m_{frag}	ΔLVP	p_1	p_2	p_3	p_4	HOM yield[1]	reference
dodecane	dodecane	low	2	1.83	0.999	0.001	0.001	0.001		Cappa et al. (2013)
		high	0.2627	1.4629	0.9657	0.0010	0.0020	0.0314		Loza et al. (2014)
α-pinene	α-pinene	low	0.305	1.97	0.419	0.426	0.140	0.014	0.44%	Chhabra et al. (2011)
		high	0.1312	1.9139	0.5991	0.2923	0.1079	0.0007	0.44%	Chhabra et al. (2011)
toluene	toluene	low	1.31	1.77	0.185	0.001	0.002	0.812	0.1%	Zhang et al. (2014)
		high	1.3064	1.4169	0.5634	0.3413	0.0016	0.0937	0.1%	Zhang et al. (2014)
m-xylene	m-xylene	low	1.08	2.05	0.102	0.001	0.878	0.019	1.7%	Ng et al. (2007)
		high	0.0736	1.4601	0.1418	0.2971	0.4571	0.1040	1.7%	Ng et al. (2007)

[1] Values are obtained in Bianchi et al. (2019).

90 **Table S4: The modeled variation of SOA yield per temperature (K). The concentration of organic aerosol is 15 μg m^{-3} for all cases. The range of model temperature is 20-40 °C.**

precursors	NOx	H_i^{vap} evaporation enthalpy (kJ mol^{-1})			
		Equation[1]	50	100	150
dodecane	high	0.0041-0.0052	0.0019-0.0022	0.0036-0.0050	0.0053-0.0095
	low	0.0062-0.0074	0.0026-0.0029	0.0053-0.0070	0.0078-0.010
α-pinene	high	0.0087-0.0089	0.0037-0.0039	0.0077-0.0088	0.011-0.015
	low	0.011-0.013	0.0041-0.0053	0.0091-0.013	0.01-0.011
toluene	high	0.0060-0.0068	0.0023-0.0026	0.0050-0.0063	0.0075-0.010
	low	0.0083-0.023	0.0044-0.0068	0.0077-0.018	0.0095-0.030
m-xylene	high	0.0049-0.099	0.0025-0.0039	0.0045-0.0094	0.0064-0.016
	low	0.0078-0.018	0.0043-0.0063	0.0073-0.015	0.0091-0.023

[1] The equation is taken from Epstein et al. (2010), $H_i^{vap} = -11 \times \log C_{i,ref}^* + 131$.
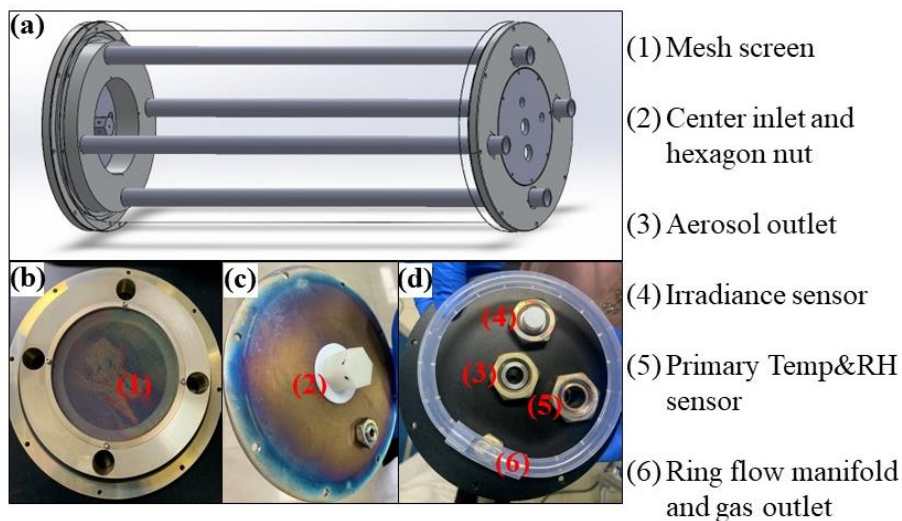
Figure S1: Schematic diagram of (a) OFR and UV lamps and photographs of (b) mesh screen near the inlet, (c) inlet and hexagon nut and (d) outlets and sensors of OFR.
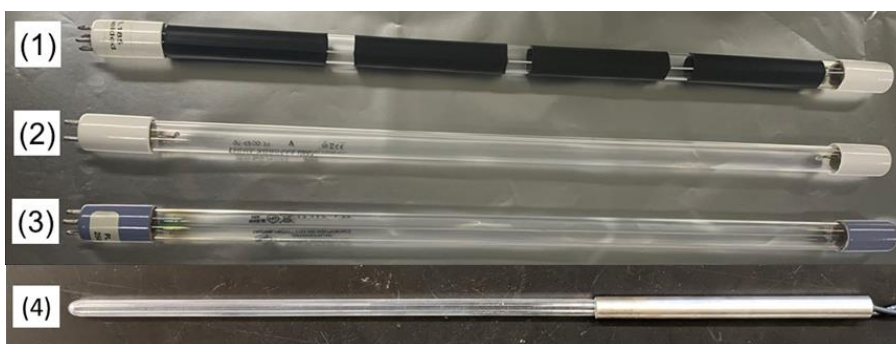
Figure S2: Four types of lamps used in this research. Type (1) transmits both 185 and 254 nm radiation, with 80% surface covered with heat shrink tubes (GPH436T5VH/4, Light Sources, Inc.). Type (2) is the same as type (1) but not covered. Type (3) transmits only 254 nm radiation and is not covered (GPH436T5L/4, Light Sources, Inc.). Type (4) transmits both 185 and 254 nm radiation (model no. 82-9304-03, BHK Inc.).
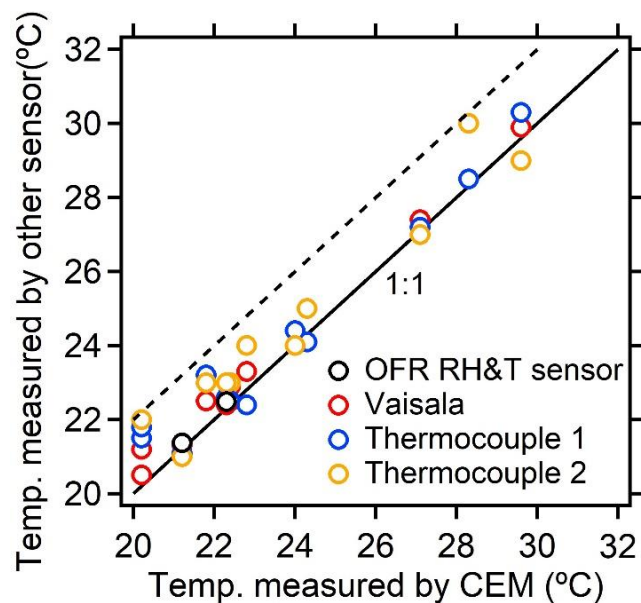
Figure S3: Comparison between different temperature measurements used in this research. The measured temperatures from the CEM sensor, which was used to measure the room temperature, are shown on the x-axis. The Vaisala sensor is used to measure the temperature inside the OFR. Thermocouple 1 and Thermocouple 2 are used to measure the temperature of the OFR exhaust and outside surface. Detailed information about different sensors can be found in Table S1.
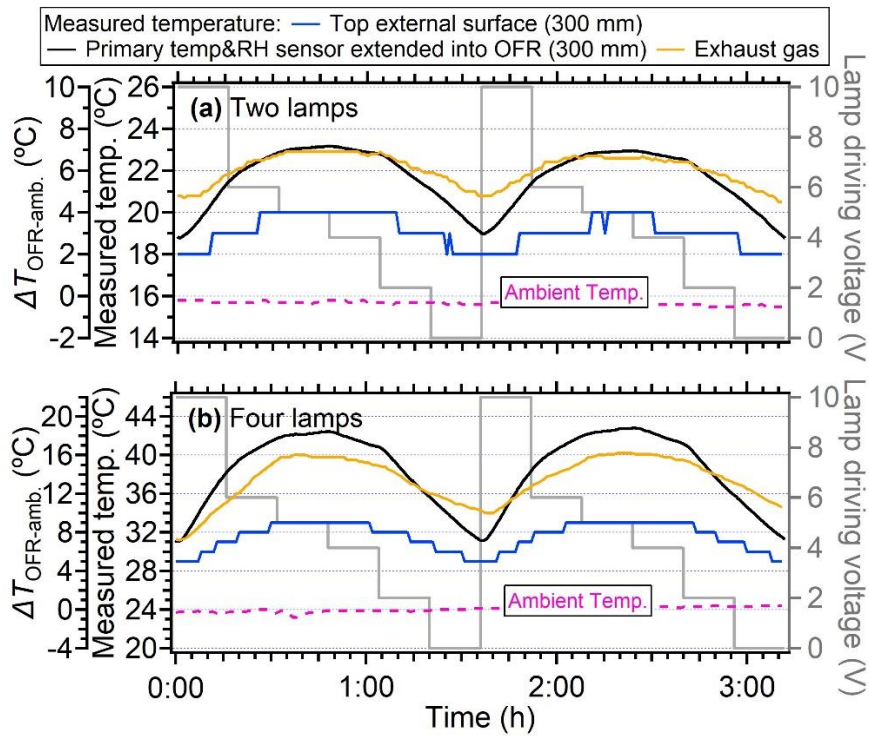
Figure S4: Temperature variation for (a) four lamps and (b) two lamps. In this case, the front plate with a hexagon nut and mesh screen was installed, and the OFR sensor set in the backplate was extended into the center of OFR (probing depth: 300 mm). The mesh screen near the back plate was removed.
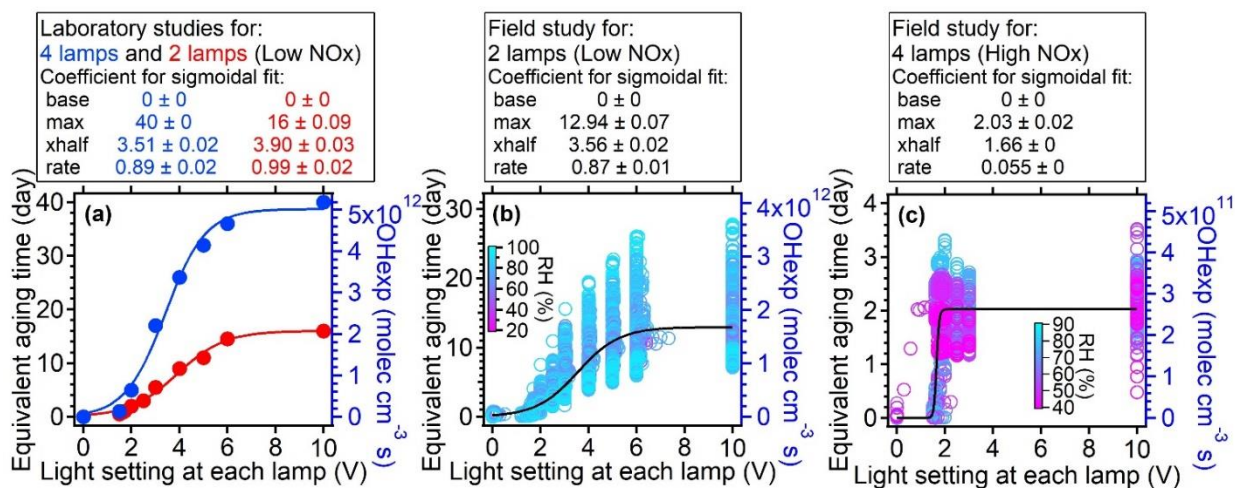
Figure S5: The correlation between OH exposures (right axis) and equivalent aging time (left axis) vs. light settings at each lamp. A sigmoidal function was used to fit the scatter plots. The OH exposures under low NOx condition in panel (a) and (b) ~~is~~were estimated based on the empirical parameterization in Hu et al. (2022), while OH exposures in panel (c) under high NOx conditions ~~is~~was estimated based on the parameterization reported in Peng et al. (2018). A water mixing ratio of ~~around~~ 1.88% (60% RH at 25 °C) under low NOx conditions was assumed in the laboratory studies (Panel (a)). The mixing ratio in field studies (Panel (b) and (c)) ~~was~~were measured directly by RH&T sensor. The input flow rate ~~is~~was 5 L min⁻¹, which corresponds to a residence time of 167 s.
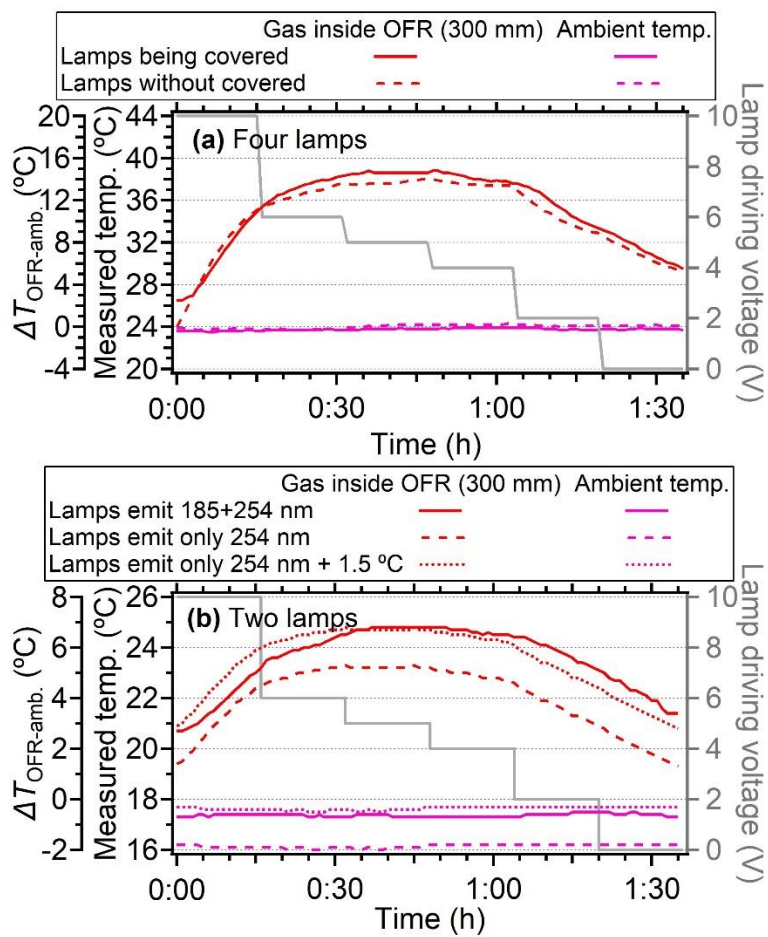
Figure S6: The measured temperature variation with different types of Light Source lamps: (a) lamps with 80% surface covered with heat-shrink tubes and lamps without covered, (b) lamps emit both 185 and 254 nm radiation and lamps emit only 254 nm radiation. The temperature of the gas inside OFR at a depth of 300 mm was measured.
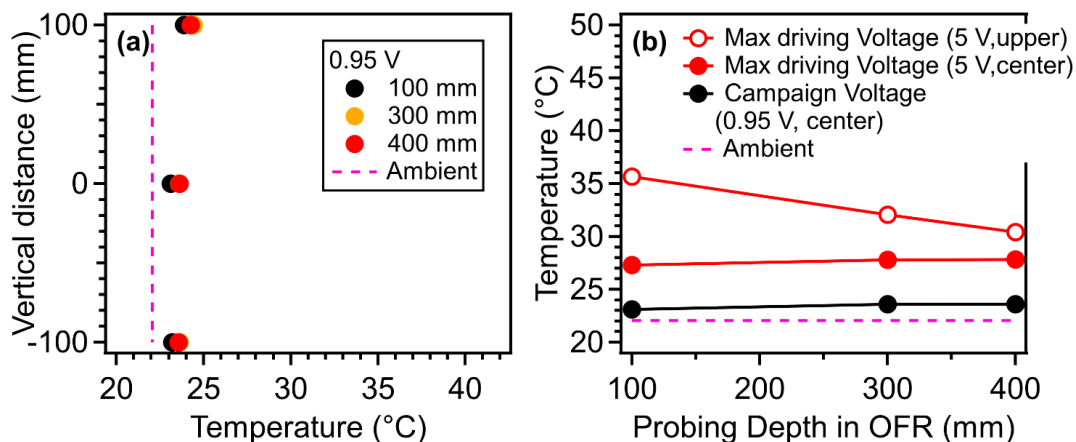
Figure S7: Temperature measured by an external temperature sensor for an OFR with BHK lamps (a) in the vertical direction at different depths inside OFR, with the driving voltage set to 0.95 V for two lamps; (b) the measured temperature at different depths inside the OFR under different driving voltages; the "upper" indicates the position of 100 mm in the vertical direction and the "center" indicated the position measured at centerline. Flow through the OFR was 4.5 L min^{-1}.
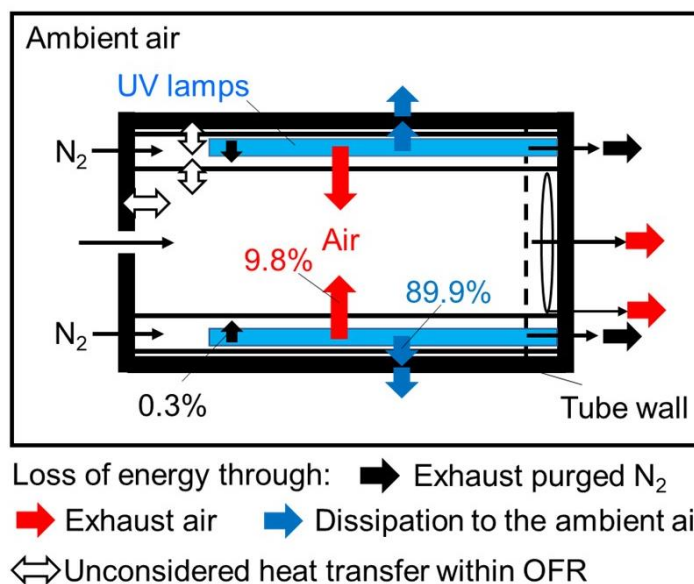
Figure S8: Schematic plot for the transfer of the heating energy ~~(orange arrows)~~ inside the OFR from the UV lamps and the loss of energy ~~(red arrows)~~ to the ambient air. The fraction of energy from the UV lamps ~~is~~was obtained from Fig. S9. Note that only the power leading to the temperature increase (51% of total power, which is 35.6 W based on the calculation in Sec S1 and S2) ~~of the~~within OFR ~~has been~~was considered for these three pathways.

12
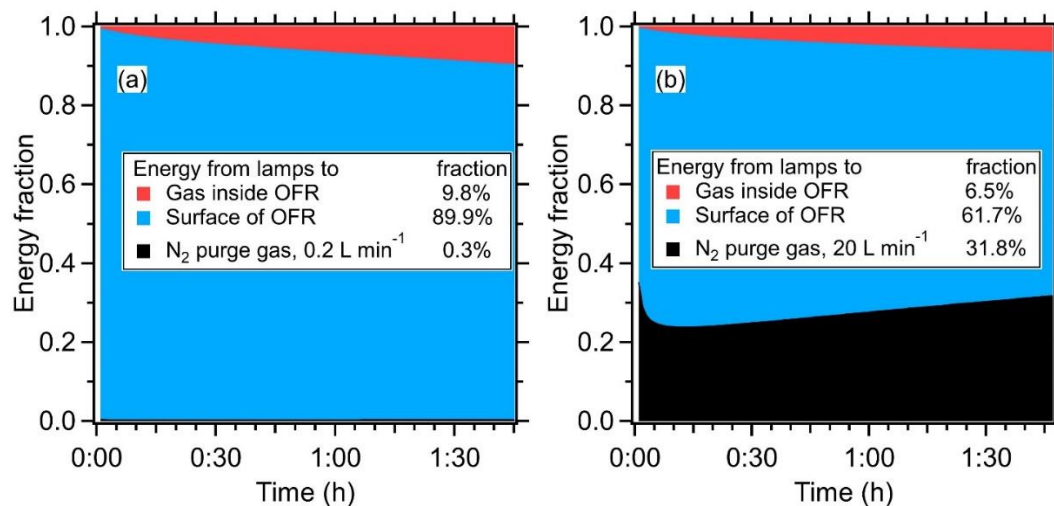
Figure S9: (a) Energy from UV lamps (51% (based on calculation in Sect. S2) of total power (35.6 W), 8.9 W for each lamp, 4 lamps in total) to gas inside OFR, surface of OFR and N_2 purge gas (0.2 L min^{-1}) as a function of time, with 4 lamps set to 10 V. The start time ~~is~~was when the lamps ~~are~~were turned on. The flow rate ~~is~~was 5 L min^{-1}. **(b)** Same as Fig. S9a, with the flow rate of N_2 purge gas increased to 20 L min^{-1}. Details of the energy calculation ~~are~~were presented in Sect. S2.
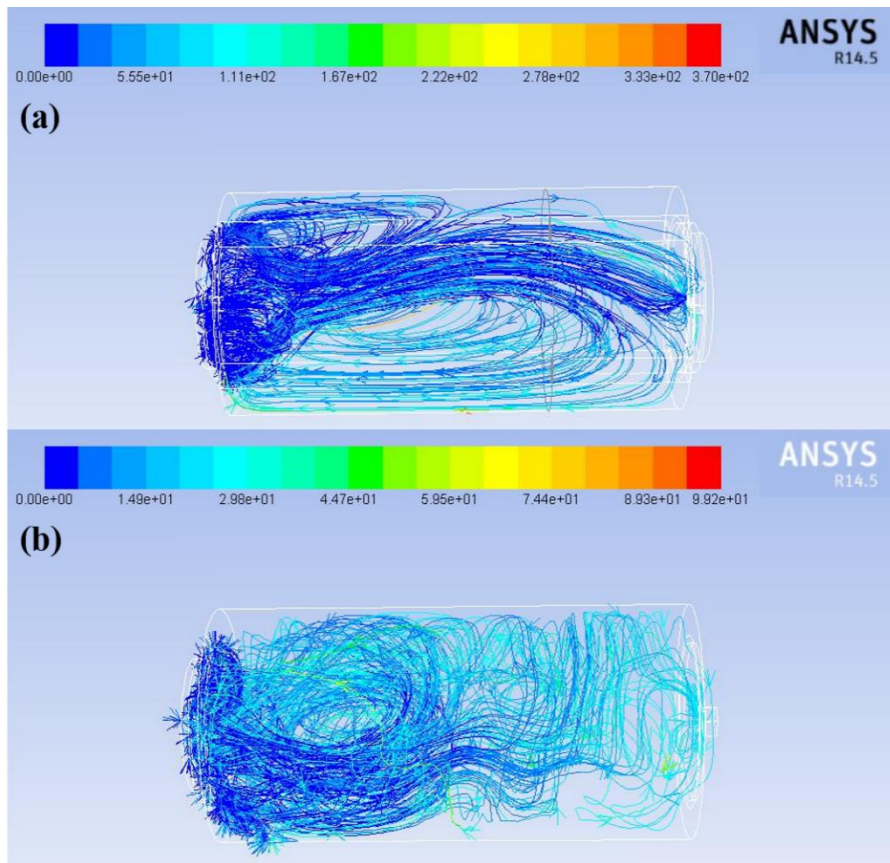
Figure S10: CFD simulation of the gases in OFR (a) without and (b) with the heating of lamps. In panel (b), the scenario of four lamps at 5 V was simulated.
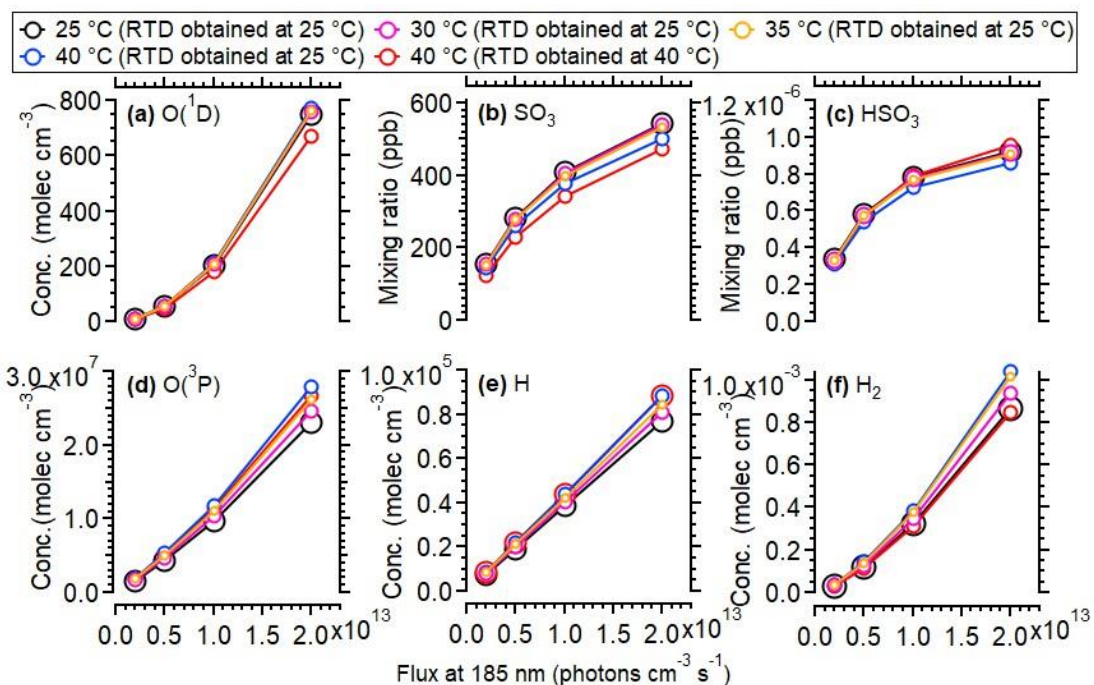
155

Figure S11: Simulated concentration of oxidant species from 25 to 40 °C in OFR as a function of OH exposure. In this scenario, the 800 ppb of initial SO₂, 2.2% water vapor mixing ratio (25 °C, 70% RH), and different photon flux at 185 nm and 254 nm (photon flux ratio of 254/185 nm= 0.05) were used. The simulated oxidant concentrations with measured RTD in OFR were also shown.
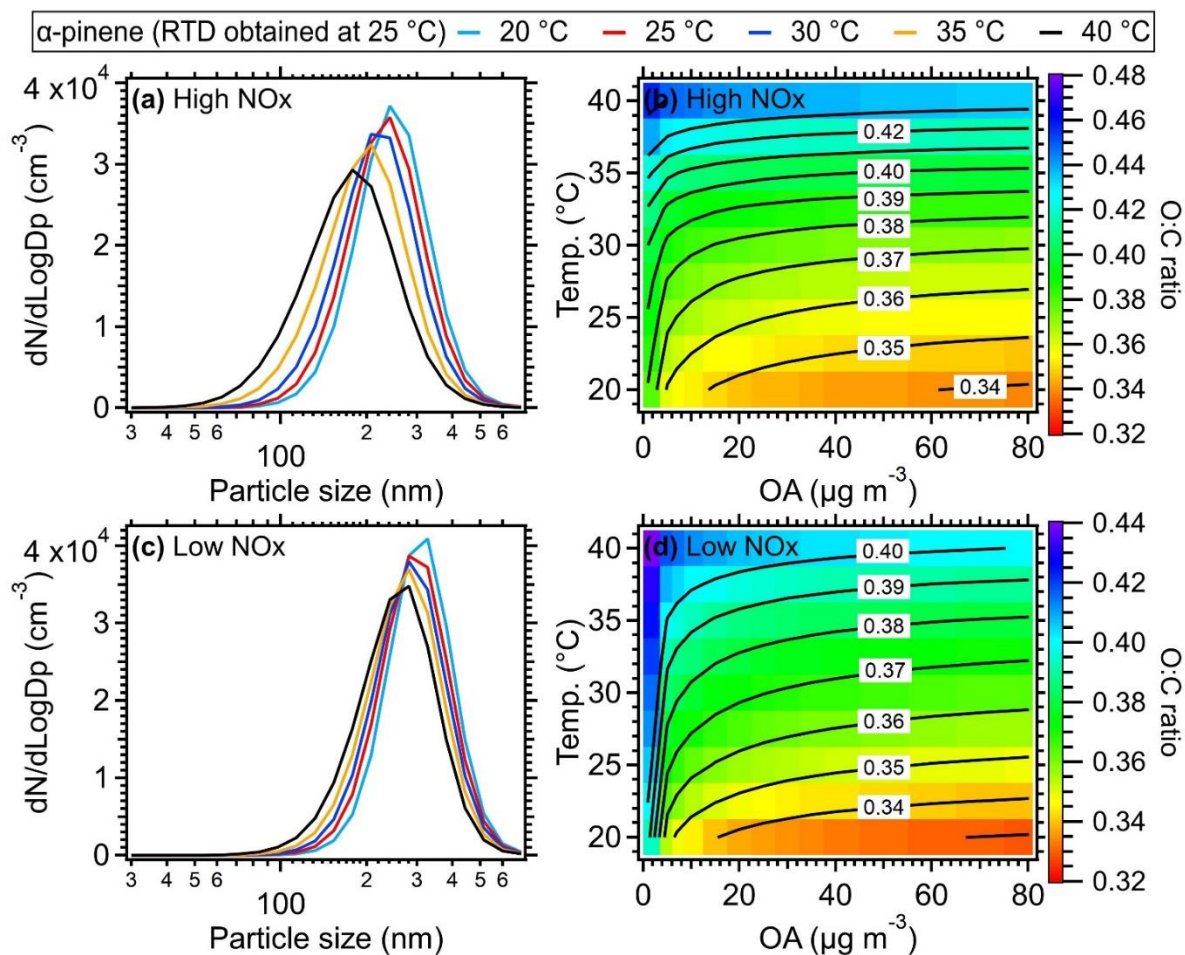
160
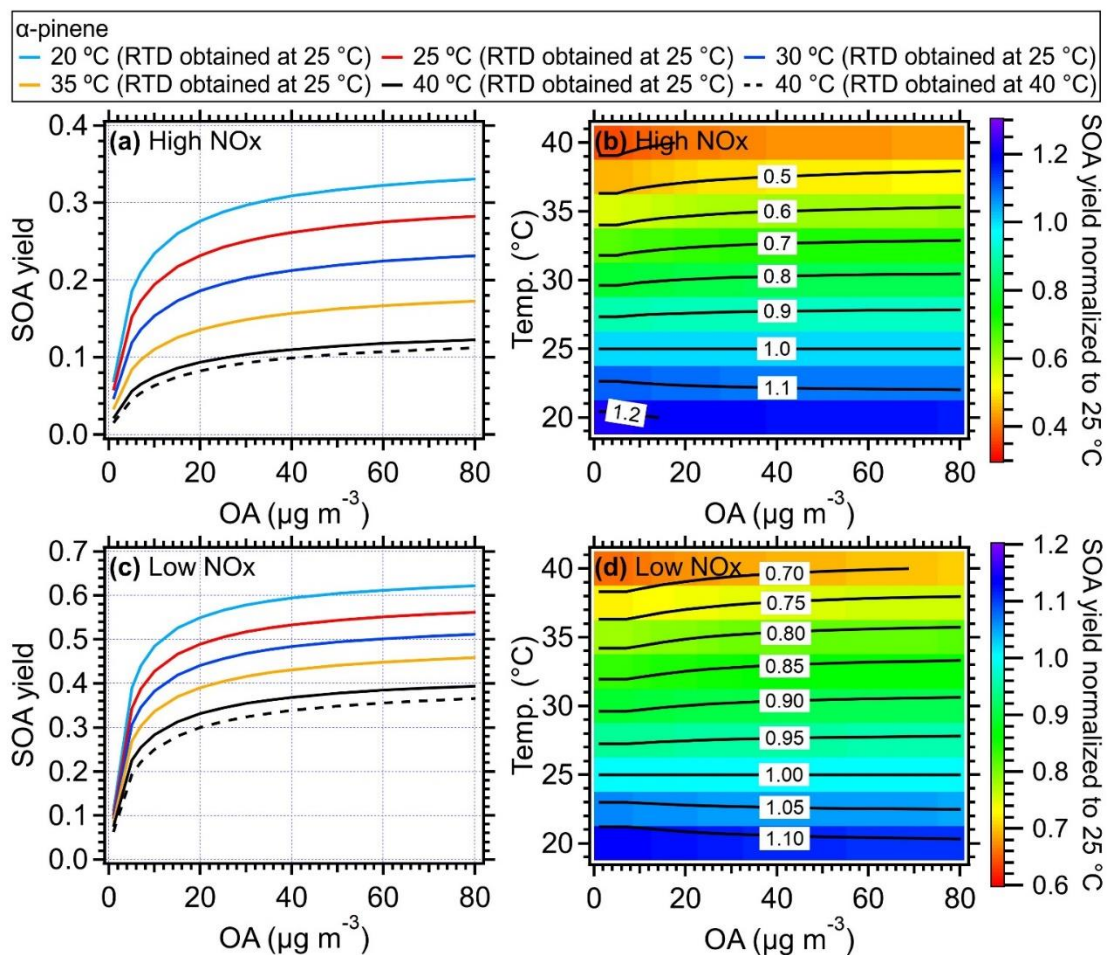
Figure S12: Simulated SOA yield of α-pinene as a function of mass concentration of organic aerosol and temperature inside of the OFR for (a) high NOx and (c) low NOx conditions, respectively. The simulated results using measured RTD obtained at 40 °C ~~are~~were shown as black dashed lines. The ratio of SOA yield of α-pinene from different temperatures compared to that of 25 °C under (b) high NOx and (d) low NOx conditions. The equivalent aging time ~~is~~was 0.5 days by assuming the OH concentration ~~is~~was equivalent to 1.5×10^6 molecule cm^{-3} (Mao et al., 2009).

16
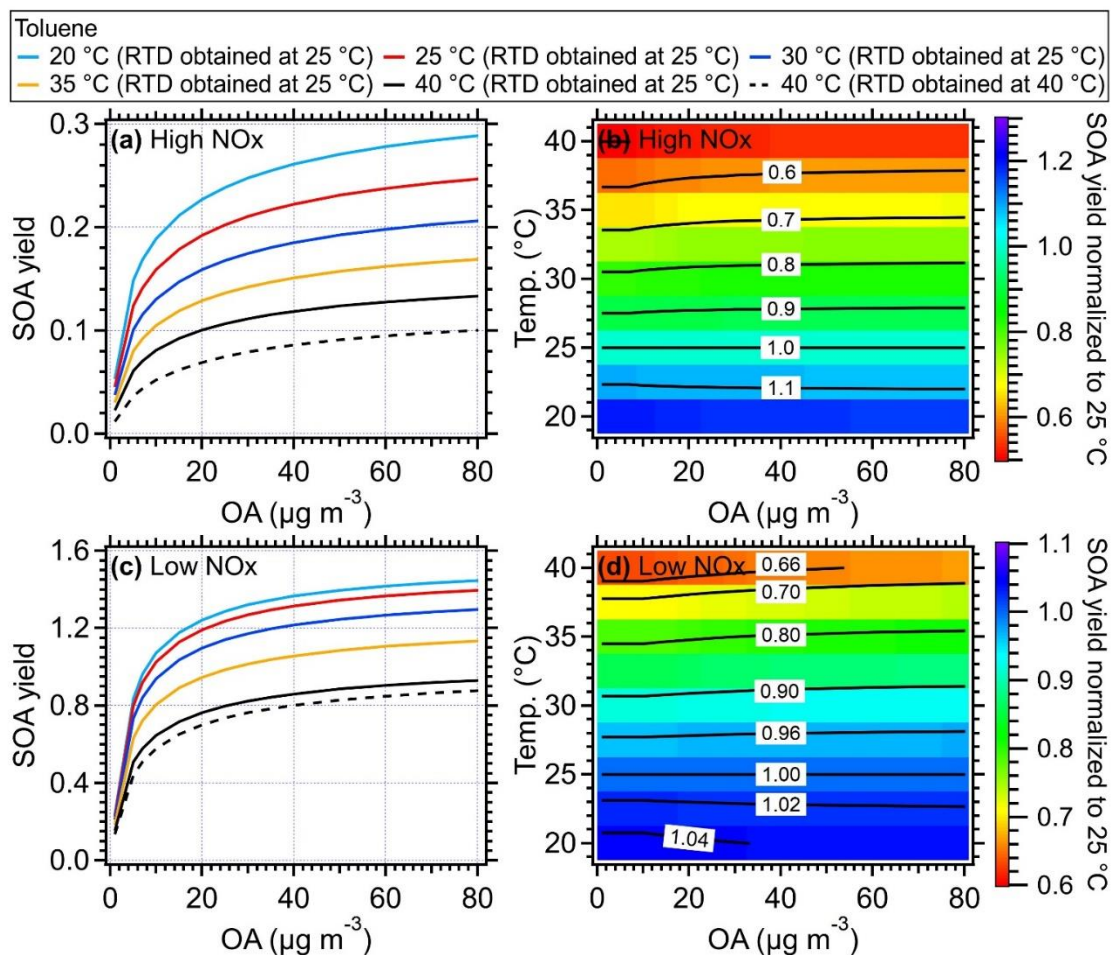
Figure S13: Simulated SOA yield of toluene as a function of mass concentration of organic aerosol and temperature inside of the OFR for (a) high NOx and (c) low NOx conditions, respectively. The simulated results using measured RTD obtained at 40 °C ~~are~~was shown as black dashed lines. The ratio of SOA yield of toluene from different temperatures compared to that of 25 °C under (b) high NOx and (d) low NOx conditions. The equivalent aging time ~~is~~was 1 day by assuming the OH concentration ~~is~~was equivalent to 1.5×10^6 molecule cm^{-3} (Mao et al., 2009).
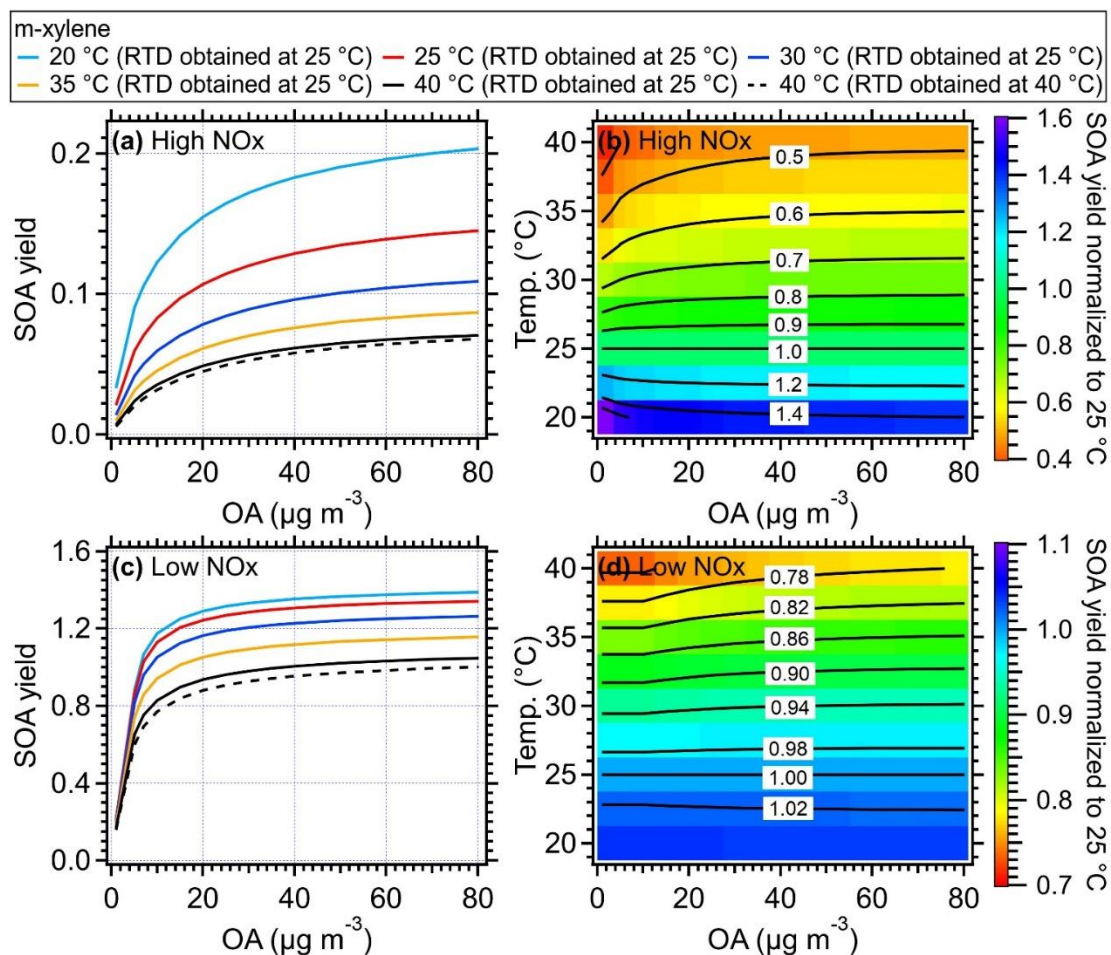
Figure S14: Simulated SOA yield of xylene as a function of mass concentration of organic aerosol and temperature inside of the OFR for (a) high NOx and (c) low NOx conditions, respectively. The simulated results using measured RTD obtained at 40 °C ~~are~~were **shown as black dashed lines. The ratio of SOA yield of xylene from different temperatures compared to that of 25 °C under (b) high NOx and (d) low NOx conditions. The equivalent aging time** ~~is~~was **1 day by assuming the OH concentration** ~~is~~was **equivalent to 1.5×10^6 molecule cm^{-3} (Mao et al., 2009).**
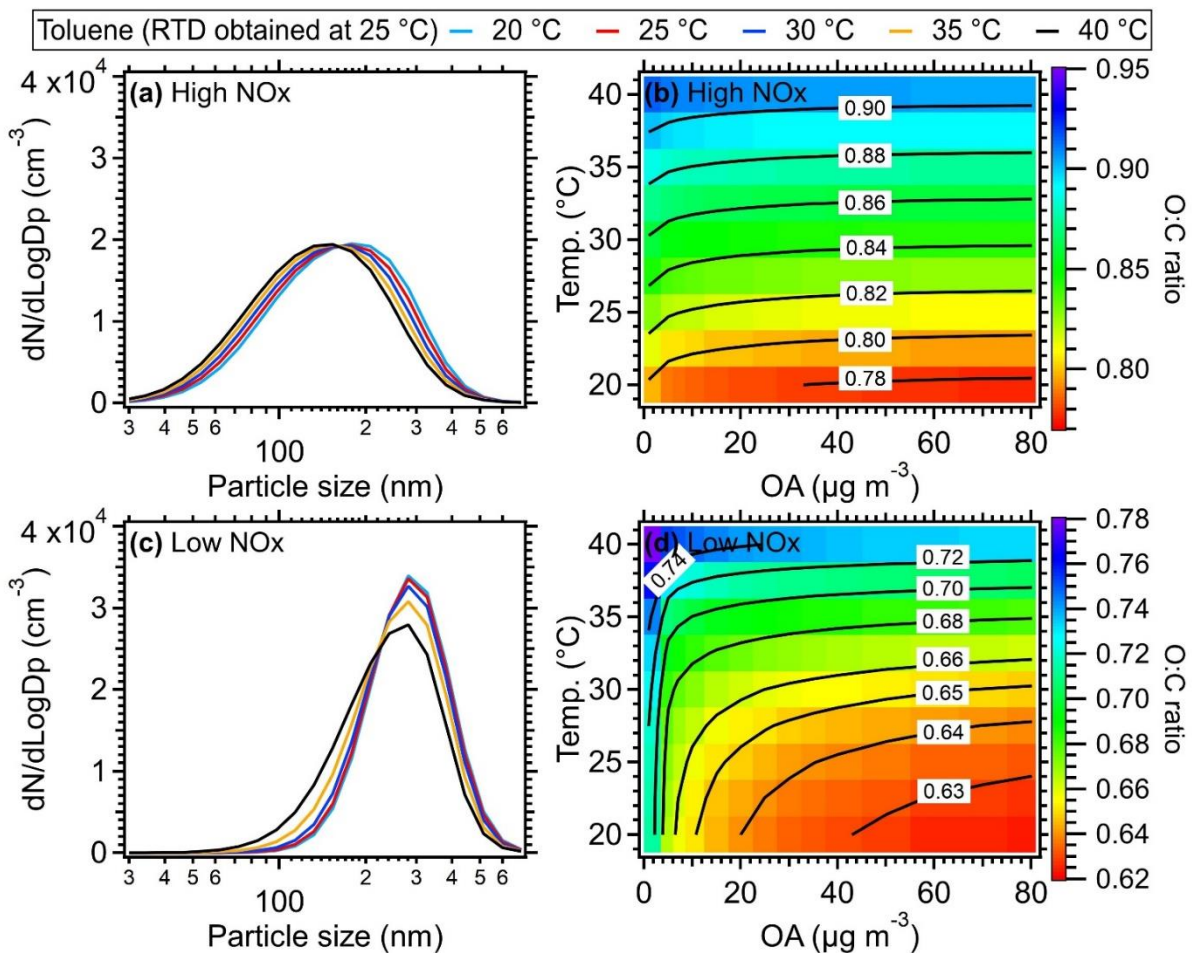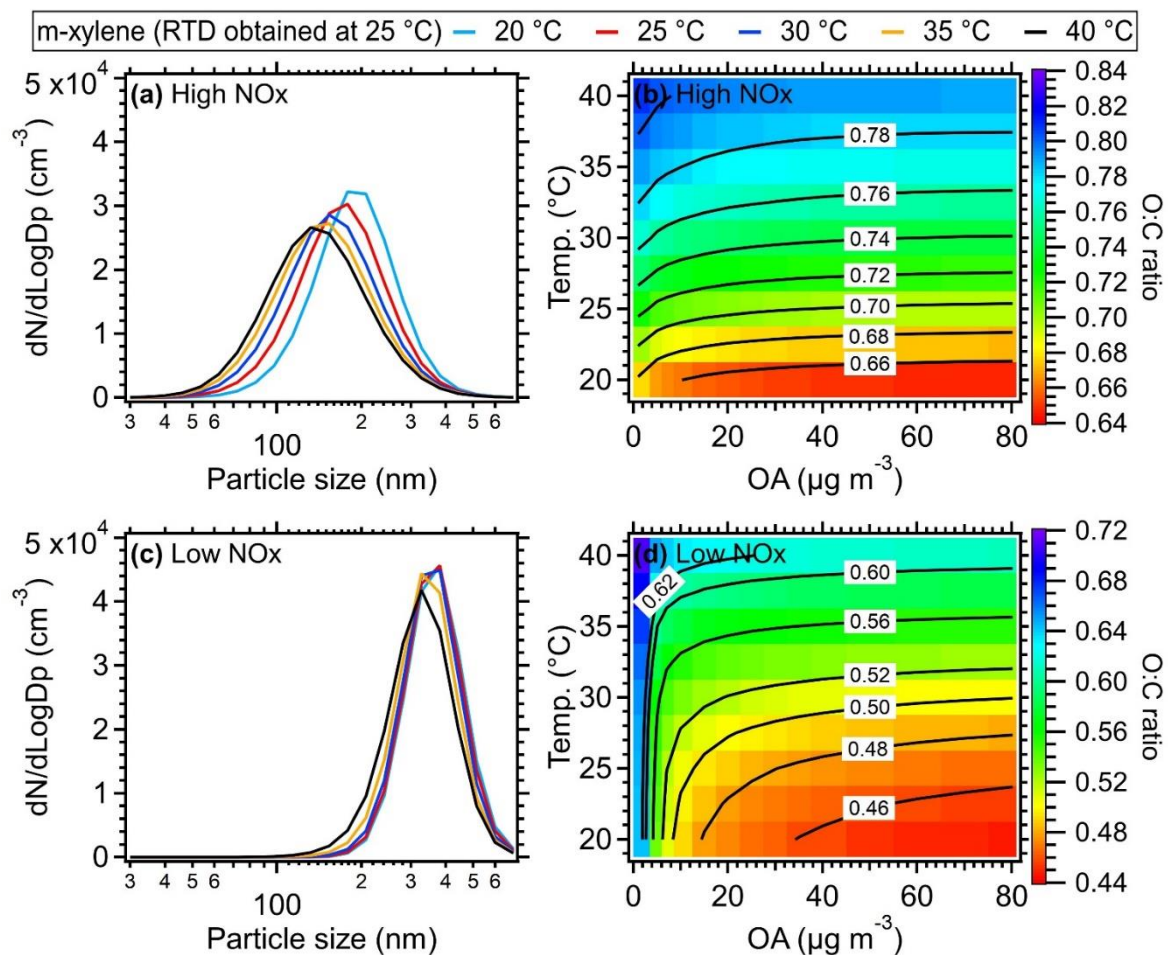
Figure S15. Simulated size distribution of α-pinene as a function of temperature by assuming the mass concentration of OA ~~is~~was 30 μg m⁻³ for (a) high NOx and (c) low NOx conditions, respectively. Simulated O: C ratio of α-pinene under different temperatures and organic aerosol concentrations under (b) high NOx and (d) low NOx conditions. The equivalent aging time ~~is~~was 0.5 days by assuming the OH concentration ~~is~~was equivalent to 1.5×10⁶ molec cm⁻³ (Mao et al., 2009).

185

Figure S16: Simulated size distribution of toluene as a function of temperature by assuming the mass concentration of
190   **OA ~~is~~was 30 μg m⁻³ for (a) high NOx and (c) low NOx conditions, respectively. Simulated O:C ratio of toluene under different temperature and organic aerosol concentration under (b) high NOx and (d) low NOx conditions. The equivalent aging time ~~is~~was 1 day by assuming the OH concentration ~~is~~was equivalent to 1.5×10⁶ molecule cm⁻³ (Mao et al., 2009).**

Figure S17: Simulated size distribution of m-xylene as a function of temperature by assuming the mass concentration of OA ~~is~~was 30 μg m^{-3} for (a) high NOx and (c) low NOx conditions, respectively. Simulated O:C ratio of m-xylene under different temperatures and organic aerosol concentration under (b) high NOx and (d) low NOx conditions. The equivalent aging time ~~is~~was 1 day by assuming the OH concentration ~~is~~was equivalent to 1.5×10^6 molecule cm^{-3} (Mao et al., 2009).
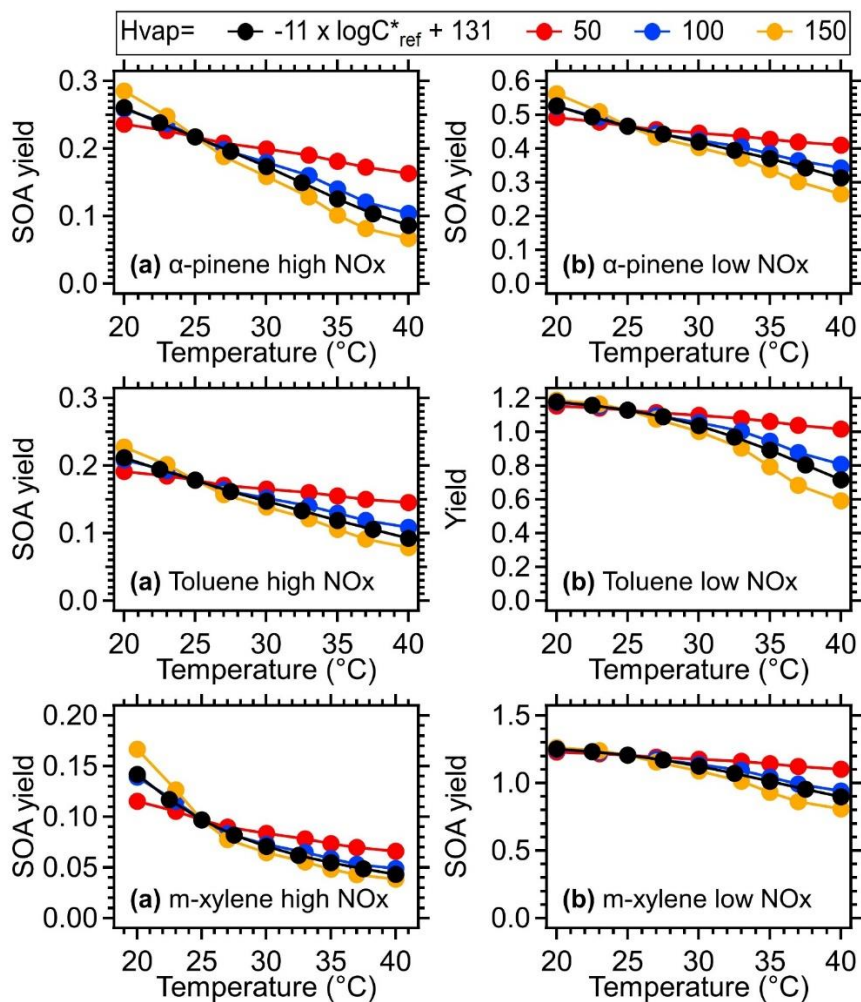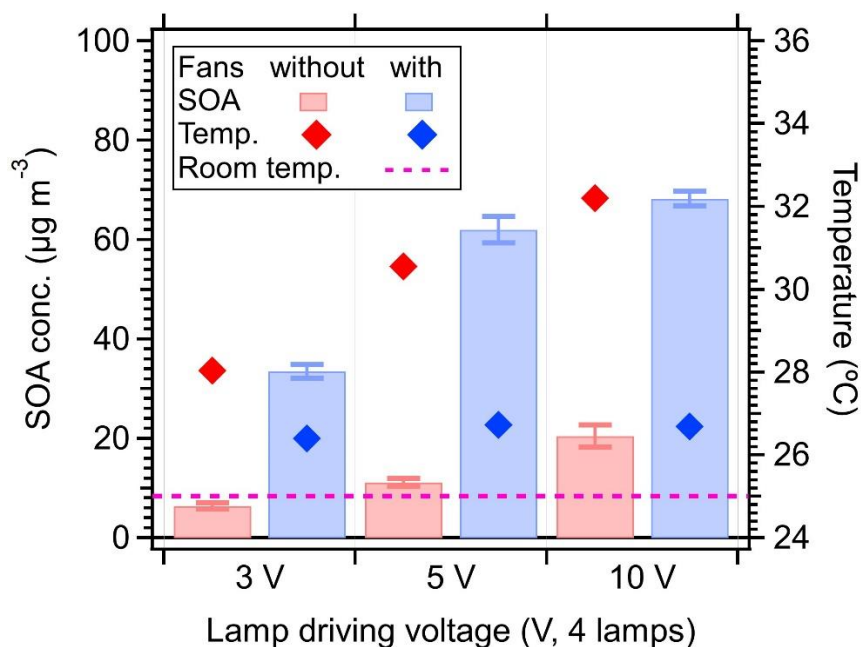
Figure S18: Simulated SOA yield of (a-b) α-pinene, (c-d) Toluene, (e-f) m-xylene as a function of temperature under different H_i^{vap} values. The mass concentration of organic aerosol ~~is~~was assumed to be 15 µg m⁻³. The equivalent aging time ~~is~~was 1 day assuming the OH concentration ~~is~~was equivalent to 1.5×10⁶ molecule cm⁻³ (Mao et al., 2009).

205

Figure S19. The SOA formation from benzene and OH radicals in the PAM-OFR as a function of light intensity. Two cases including PAM-OFR was blown with fans and without fans were both shown. The room temperature and temperature measured with the primary Temp&RH sensor set in the back panel were shown in the right axis. Note the OFR temperature reported here is the lower limit as discussed in section 3.1.5. The gas-phase benzene (99.80%, Sigma-Aldrich) was generated with syringe pumps. Benzene was used as gas-phase precursor in this experiment due to its lower kOH, since benzene will not be totally consumed under the high OH exposure at high voltage settings in OFR. The flow rate in this experiment was 4.5 L min^{-1}, and the RH was ~30%.
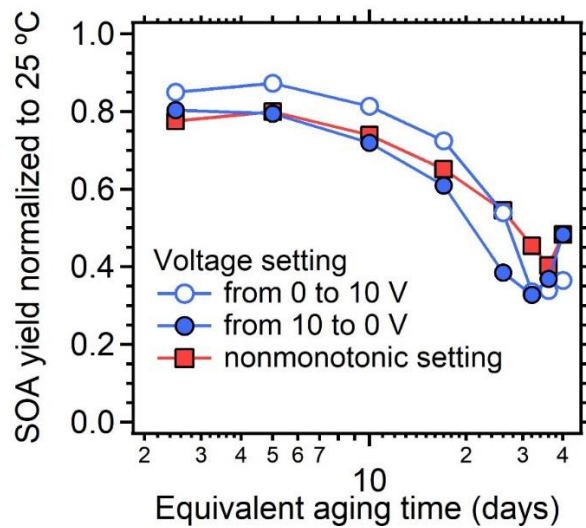
215

Figure S20. Simulated ratio of SOA yield with measured temperature vs. that under 25 °C under varied lamp settings. A 10-ppb toluene with OA mass concentration of 30 µg m^{-3} was assumed. The equivalent aging time is̶was calculated by assuming the OH concentration is̶was equivalent to 1.5×10^6 molecule cm^{-3} (Mao et al., 2009).

References

Bianchi, F., Kurten, T., Riva, M., Mohr, C., Rissanen, M. P., Roldin, P., Berndt, T., Crounse, J. D., Wennberg, P. O., Mentel, T. F., Wildt, J., Junninen, H., Jokinen, T., Kulmala, M., Worsnop, D. R., Thornton, J. A., Donahue, N., Kjaergaard, H. G., and Ehn, M.: Highly Oxygenated Organic Molecules (HOM) from Gas-Phase Autoxidation Involving Peroxy Radicals: A Key Contributor to Atmospheric Aerosol, Chem Rev, 119, 3472-3509, https://doi.org/10.1021/acs.chemrev.8b00395, 2019.

Cappa, C. D., Zhang, X., Loza, C. L., Craven, J. S., Yee, L. D., and Seinfeld, J. H.: Application of the Statistical Oxidation Model (SOM) to Secondary Organic Aerosol formation from photooxidation of of C12 alkanes, Atmospheric Chemistry and Physics, 13, 1591-1606, https://doi.org/10.5194/acp-13-1591-2013, 2013.

Chhabra, P. S., Ng, N. L., Canagaratna, M. R., Corrigan, A. L., Russell, L. M., Worsnop, D. R., Flagan, R. C., and Seinfeld, J. H.: Elemental composition and oxidation of chamber organic aerosol, Atmospheric Chemistry and Physics, 11, 8827-8845, https://doi.org/10.5194/acp-11-8827-2011, 2011.

Epstein, S. A., Riipinen, I., and Donahue, N. M.: A semiempirical correlation between enthalpy of vaporization and saturation concentration for organic aerosol, Environ Sci Technol, 44, 743-748, https://doi.org/10.1021/es902497z, 2010.

Holman, J. P.: Heat Transfer, 10 edn, McGraw-Hill, New York, USA, 2010.

Hu, W., Zhou, H., Chen, W., Ye, Y., Pan, T., Wang, Y., Song, W., Zhang, H., Deng, W., Zhu, M., Wang, C., Wu, C., Ye, C., Wang, Z., Yuan, B., Huang, S., Shao, M., Peng, Z., Day, D. A., Campuzano-Jost, P., Lambe, A. T., Worsnop, D. R., Jimenez, J. L., and Wang, X.: Oxidation Flow Reactor Results in a Chinese Megacity Emphasize the Important Contribution of S/IVOCs to Ambient SOA Formation, Environ Sci Technol, 56, 6880-6893, https://doi.org/10.1021/acs.est.1c03155, 2022.

Huang, Y., Coggon, M. M., Zhao, R., Lignell, H., Bauer, M. U., Flagan, R. C., and Seinfeld, J. H.: The Caltech Photooxidation Flow Tube reactor: design, fluid dynamics and characterization, Atmospheric Measurement Techniques, 10, 839-867, https://doi.org/10.5194/amt-10-839-2017, 2017.

Loza, C. L., Craven, J. S., Yee, L. D., Coggon, M. M., Schwantes, R. H., Shiraiwa, M., Zhang, X., Schilling, K. A., Ng, N. L., Canagaratna, M. R., Ziemann, P. J., Flagan, R. C., and Seinfeld, J. H.: Secondary organic aerosol yields of 12-carbon alkanes, Atmospheric Chemistry and Physics, 14, 1423-1439, https://doi.org/10.5194/acp-14-1423-2014, 2014.

Mao, J., Ren, X., Brune, W. H., Olson, J. R., Crawford, J. H., Fried, A., Huey, L. G., Cohen, R. C., Heikes, B., Singh, H. B., Blake, D. R., Sachse, G. W., Diskin, G. S., Hall, S. R., and Shetter, R. E.: Airborne measurement of OH reactivity during INTEX-B, Atmospheric Chemistry and Physics, 9, 163-173, https://doi.org/10.5194/acp-9-163-2009, 2009.

Ng, N. L., Kroll, J. H., Chan, A. W. H., Chhabra, P. S., Flagan, R. C., and Seinfeld, J. H.: Secondary organic aerosol formation from m-xylene, toluene, and benzene, Atmospheric Chemistry and Physics, 7, 3909-3922, https://doi.org/10.5194/acp-7-3909-2007, 2007.

Peng, Z., Palm, B. B., Day, D. A., Talukdar, R. K., Hu, W., Lambe, A. T., Brune, W. H., and Jimenez, J. L.: Model Evaluation of New Techniques for Maintaining High-NO Conditions in Oxidation Flow Reactors for the Study of OH-Initiated Atmospheric Chemistry, ACS Earth and Space Chemistry, 2, 72-86, https://doi.org/10.1021/acsearthspacechem.7b00070, 2018.

Zhang, X., Cappa, C. D., Jathar, S. H., McVay, R. C., Ensberg, J. J., Kleeman, M. J., and Seinfeld, J. H.: Influence of vapor wall loss in laboratory chambers on yields of secondary organic aerosol, Proc Natl Acad Sci U S A, 111, 5802-5807, https://doi.org/10.1073/pnas.1404727111, 2014.